ONE DIMENSIONAL AND MULTISCALE MODELS FOR BLOOD FLOW CIRCULATION

THÈSE N^{O} 3006 (2004)

PRÉSENTÉE À LA FACULTÉ SCIENCES DE BASE

Institut d'analyse et de calcul scientifique

SECTION DE MATHÉMATIQUE

ÉCOLE POLYTECHNIQUE FÉDÉRALE DE LAUSANNE

POUR L'OBTENTION DU GRADE DE DOCTEUR ÈS SCIENCES

PAR

Daniele LAMPONI

laurea in fisica, Università degli Studi di Bologna, Italie
et de nationalité italienne

acceptée sur proposition du jury:

Prof. A. Quarteroni, directeur de thèse
Dr J. Peiro, rapporteur
Prof. N. Stergiopulos, rapporteur
Prof. A. Veneziani, rapporteur

Lausanne, EPFL
2004

A mio nonno

Abstract

The aim of this work is to provide mathematically sound and computationally effective tools for the numerical simulation of the interaction between fluid and structures as occurring, for instance, in the simulation of the human cardiovascular system. This problem is global, in the sense that local changes can modify the solution far away. From the point of view of computing and modelling this calls for the use of *multiscale methods*, where simplified models are used to treat the global problem leaving to more accurate models the local description. Moreover it is characterised by the appearance of pressure waves inside the vessels.

In large arteries the vessel wall dynamics can be described by a thin elastic membrane model (Navier equation) while the fluid motion can be represented by the Navier-Stokes equations for incompressible Newtonian fluids.

Unfortunately, given the high levels of details furnished by this model, its computational complexity is dramatically high. Therefore reduced models have been developed. In particular, *one-dimensional models*, originally introduced by Euler, seem to be appropriate for the study in the time-space domain of pressure wave propagation induced by the interaction between the fluid and the vessel wall in the arterial tree. These reduced models are obtained after integrating the Navier-Stokes equations over a vessel section, supposed to be circular, and assuming an *algebraic wall law* to describe the relationship between pressure and wall deformation. They can be used in place of the more complex three dimensional fluid-structure models or in cooperation with them (*multiscale approach*).

The first part of this work deals with *one dimensional models*. A reduced 1D model taken from literature is presented and analysed. Some extensions of the basic model, in particular with respect to vessel wall law (*generalised string model*) and more complex geometries (*bifurcated and curved arteries*), are also considered. Numerical schemes are proposed and some numerical results are presented.

In the second part of this thesis we focus on a *multiscale model*. We consider a 55 arterial tree, described by the 1D model, coupled with *lumped parameter models* for heart and capillaries. In particular, specific attention has been devoted to the coupling between the left ventricle and the arterial system, whose physiopathological relevance is well known. This mathematical model gives good results in numerical tests and is able to describe the relevant features of the pressure wave propagation and reflections whithin the arterial system.

Riassunto

L'obiettivo di questo lavoro è lo sviluppo di modelli e codici per la simulazione dell'interazione tra fluido e struttura, nell'ambito dello studio del sistema cardiovascolare umano. Questo problema è globale, nel senso che cambiamenti locali possono avere conseguenze in un qualsiasi punto del sistema cardiovascolare. Da un punto di vista modellistico si dovrà pertanto ricorrere all'uso di particolari tecniche conosciute con il nome di metodi multiscala: il problema globale è risolto utilizzando modelli elementari, mentre localmente sono usati modelli più accurati. Un'altra peculiarità di questo problema sono le onde di pressione che si propagano lungo le arterie.

Nelle larghe arterie la dinamica della parete può essere descritta da una membrana (equazione di Navier) mentre il fluido può essere rappresentato con le equazioni di Navier-Stokes per i fluidi Newtoniani incomprimibili.

Sfortunatamente, a fronte di un'alta capacità descrittiva, la complessità computazionale di questo modello è drammaticamente elevata. Per questo motivo sono stati sviluppati modelli ridotti. In particolare, i modelli monodimensionali, originariamente introdotti da Eulero nel 1844, appaiono indicati per la descrizione della propagazione delle onde di pressione indotte dall'interazione tra il fluido e la parete delle arterie. Questi modelli ridotti sono ottenuti integrando le equazioni di Navier-Stokes su una sezione supposta circolare e facendo l'ipotesi di una legge di parete algebrica. Essi possono essere usati sia al posto dei più complessi modelli tridimensionali di interazione fluido-struttura sia in cooperazione con loro (metodo multiscala).

Nella prima parte di questo lavoro vengono trattati i modelli monodimensionali. Un modello ridotto 1D già presente in letteratura è illustrato ed analizzato. Alcune estensioni di questo modello basilare, in particolare rispetto alla legge di parete delle arterie (modello di stringa generalizzato) e a più complesse geometrie (biforcazioni e arterie curve), sono oltretutto considerate. Infine vengono presentati gli schemi numerici utilizzati per la risoluzione e alcuni risultati.

La seconda parte della tesi è incentrata su un modello multiscala. Viene considerato un sistema di 55 arterie, descritte col modello monodimensionale, accoppiato con modelli a parametri ristretti per il cuore e i capillari. Vista la sua importanza fisiopatologica, un'attenzione particolare è stata rivolta all'interazione tra il ventricolo sinistro e il sistema arterioso. Il modello matematico presentato dà buoni risultati nei tests numerici ed è capace di riprodurre le caratteristiche principali della propagazione delle onde di pressione.

Acknowledgements

I thank Prof. A. Quarteroni, who has given me the opportunity to work on a very interesting subject and in an exciting environnement. He has continuously stimulated me to investigate further aspects of the problem, pushing me to finish my PhD.

I am very grateful also to Prof. L. Formaggia with whom I had the chance, the possibility and the pleasure to work during the first part of my PhD. He has always been ready to give me suggestions and indications on mathematical topics and to help me in overcoming the numerous difficulties encountered.

I would like to thank all the people with whom I have had the chance to collaborate and discuss, and particularly among them, Prof. S. Čanić, Prof. S. Sherwin, Dr. F. Nobile, Dr. M. Tuveri and Prof. A. Veneziani. I mention also Prof. A. Mikelić who has show me how a true mathematician works.
Special thanks to Dr. M. Discacciati and Dr. S. Deparis with whom I shared the office.

I also thank Dr. J. Peiró, Prof. N. Stergiopulos and Prof. A. Veneziani who accepted to be members of the jury, as well as Prof. B. Dacorogna who presided the jury.

I acknowledge the *Fonds National Suisse* that has supported this work.

Dedico questa tesi a mio nonno, alla sua bontà, alla sua calma, alla sua energia, alla sua costanza, al suo coraggio, al suo entusiasmo, alla sua fede.

Contents

Introduction

The numerical simulation of blood flow in human arteries attracts nowadays the interest of many researchers. Even if cardiac arrest remains the top lethal disease in industrialised nations (see e.g. [5] and [3]), the medical, social and economical impact of the evolution of treatment methods will continue to be large. In fact, the increase in expectation life combined with the changes in living and eating habits causes the alteration of blood vessel properties and, hence, the occurrence of heart and vascular diseases.

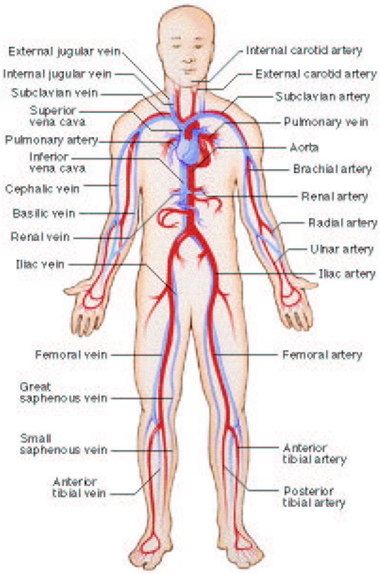

Figure 1: Human circulatory system, taken from [4]. Roughly speaking the human circulatory system is composed by the heart (Figure 2), the arteries and the veins, the arteries bringing oxygenated blood from heart left ventricle to the various organs, the veins bringing it back to the right atrium, and the heart acting as a pump.

The objective of this work is to provide mathematically sound and computationally effective tools for the numerical simulation of the interaction between fluid and structures as occurring, for instance, in the simulation of the human cardiovascular system (Figure 1).

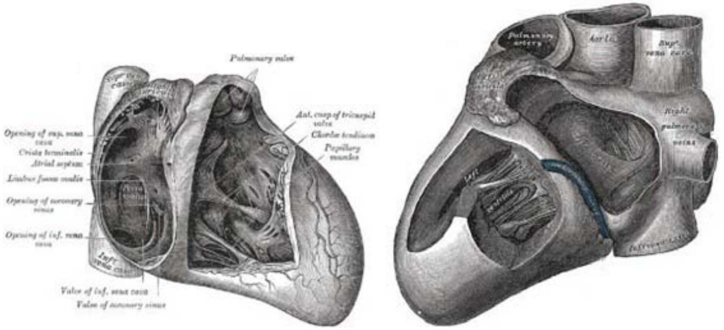

Figure 2: The human heart, interior of the right side and of the left side of the heart, taken from [6]. Its functioning is very complex and involves among other things the electro-chemical activation of the muscle cells (see e.g. [8]).

Today, numerical simulations of the human circulatory system still feature a limited role in the ongoing field of creating new and perfecting existing methods for treating heart and related diseases. Even the modelling of the human blood is a difficult task, being composed of many particles (i.e. red and white blood cells and platelets), the significance of each varying with the size of the blood vessel of interest (e.g blood can be considered as a continuum in large arteries, while in capillaries its discontinuous nature cannot be neglected). Moreover it interacts with the vessel wall (Figure 3) whose structure is also very complex.

At the moment, most results from numerical simulations are used to gain a better understanding of flow patterns and vessel wall stresses when an anomaly occurs, for example in an aortic stenosis or in an aortic abdominal aneurism (AAA). A stenosis is a constriction or narrowing of an artery (for instance cholesterol and other substances over time may clog the artery), while an aneurysm is usually defined as a focal dilation of the aorta at least 150 % of the normal aortic diameter. AAA can continue to expand and rupture spontaneously, exsanguinate, and cause death. The rupture is an important cause of unheralded deaths in people over 55 years of age, claiming more than 15,000 lifes annually in the United States alone. One possible technique to treat a stenosis is to put a stent: this is a wire metallic mesh (see Figure 4), which stays permanently in the artery, holding it open and improving blood flow to the heart muscle. The aneurism is treated in a similar way by replacing the damaged tissue by a prosthesis or endograft (Figure 5).
In particular numerical simulations become very advantageous, being relatively cheap and safe, in the preliminary testing of new product designs [54, 40, 55, 2, 1].

In this work we will focus on the human arterial system (Figure 6). This last can be mathematically described by different models with a different level of detail, from 3D Navier-

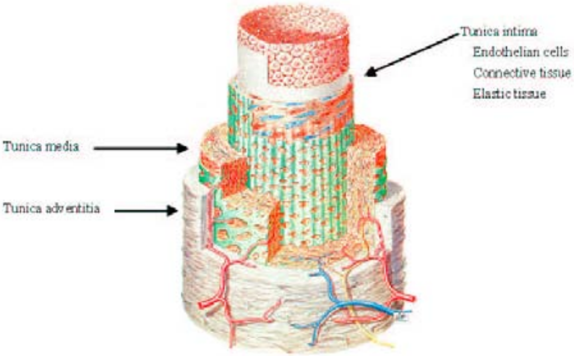

Figure 3: Vessel wall (courtesy of K. Kangasniemi and H. Opas). The structure and the mechanical properties of artery wall are rather complex (see e.g. [50, 79]). Large and medium sized arteries consist of 3 distinct layers: tunica intima, tunica media and tunica adventitia. The tunica intima consists of three layers: endothelian cells, connective tissue and an elastic tissue. The tunica media is the thickest layer and is composed mainly of connective tissue, smooth muscle cells and elastic tissue. The structure of the tunica media also depends on the type of artery. In larger arteries it consists of connective tissues, elastic tissue and elastic fibers. In smaller arteries, like the arteries in the arm, smooth muscle cells replace the elastic fiber layer. The tunica media predominantly determines the mechanical properties of the arterial wall. The tunica adventitia consists of collagen fibers and elastic tissue [19].

Stokes based ones [103] down to lumped parameter systemic representations based on the analogy between hydraulic and electric networks (see e.g. [105],[61],[106], [34], [83]), passing throughout 3D axial-symmetric model [22] and 1D reduced models [77, 16].
In particular, one dimensional models, originally introduced by Euler [26], seem to be appropriate for the study in the time-space domain of pressure wave propagation induced by the interaction between the fluid and the vessel wall in the arterial tree (see [69, 70, 96, 92, 99, 68, 66, 77]). In this specific framework these reduced models can be used in place of the more complex three dimensional fluid-structure models or in cooperation with them. Their computational complexity is dramatically lower than that of multidimensional models based on the coupling of Navier-Stokes equations for the flow field and a mechanical model for the vessel wall displacement. For example a one dimensional simulation of 3 s, i.e. approximately 4 cardiac cycles, of an arterial tree consisting of the main 55 arteries in the human body (Figure 7) takes less than 10 minutes on a standard PC, while a fluid-structure interaction Navier-Stokes simulation of an artery of length 6 cm takes 1 hour just for a period of 0.3 s.

Their principal property is to allow a good description of pressure waves propagation in arteries [99, 69]. For this reason they can be successfully used to investigate the effects of the geometrical and mechanical arterial modification, due e.g. to the presence of stenoses, or to the placement of stents or prostheses [32, 14, 90, 17], as occurs for instance in abdominal aortic

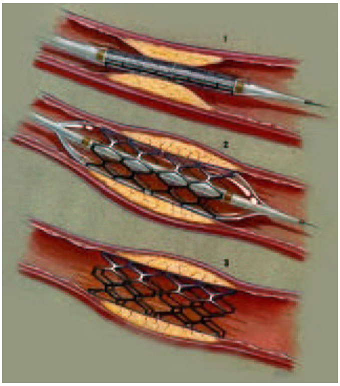

Figure 4: Balloon expandable stent. (1) Stenosis in a artery; the internal balloon is inflated and it plastically deforms the stent. (2) The stent constitutes a real scaffolding for the artery that recovers again the original lumen. (3) The balloon is deflated and then pulled out, while the stent is left inside the artery.

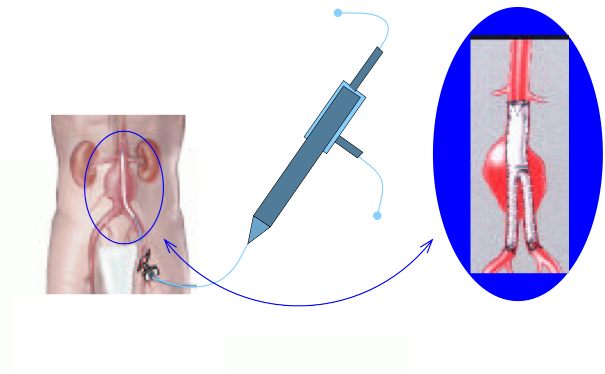

Figure 5: Non invasive vascular treatment of abdominal aortic aneurysm. An endograft is placed in the AAA site to substitute the damaged tissue.

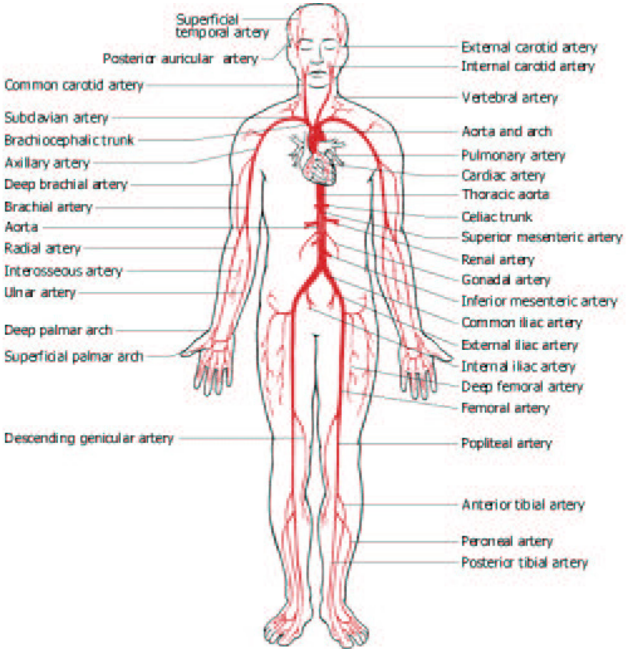

Figure 6: Human arterial system, taken from [4]. Arteries can be regarded as hollow tubes; we can subdivide them in large arteries, medium arteries and capillaries. In this Figure the large arteries are depicted . Their main role is to bring blood from the heart to the periphery acting as a “compliant system”; in fact they deform under blood pressure storing, hence, elastic energy during the systolic phase. This is given back during the dyastolic phase.

aneurism. Their computational cost makes it possible not only to study the local pressure wave propagation [70, 96, 72, 73, 63, 64] but even the global one [30, 91, 62, 63]. Moreover the computational performance could be improved using parallel computing [47].
On the other hand, they are also used in the framework of a multiscale approach [33, 71, 48, 30, 78, 82], where they are coupled with lumped parameter models (also called 0D models) [84, 105, 83] and three dimensional fluid-structure models [60]. As discussed in [28] and in [31] such reduced models can be used to provide correct boundary conditions to 3D calculations and, thence, to perform global simulations of human cardiovascular system (Figure 8).

This work is divided in two parts: *One dimensional models for blood flow simulations* and *A multiscale simulation of the human arterial system.*

The first part deals with a one dimensional model for the fluid-structure interaction problem in arteries, its numerical solution and the extensions of the basic 1D model realised during

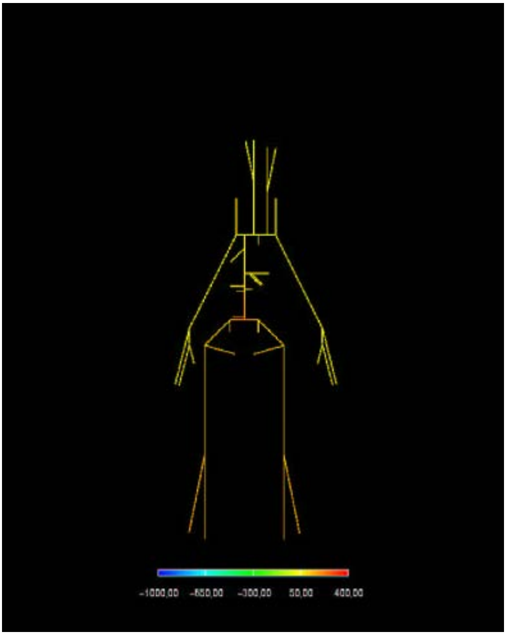

Figure 7: A system of 55 arteries representing the human arterial tree. This simulation was realised using a network of one dimensional models.

the present work.

In *Chapter 1* the state of the art of one dimensional modelling is presented: a derivation of a 1D model is briefly carried out and some theoretical results taken from the literature [77, 28, 15] are reported. The resulting model consists of a 2×2 hyperbolic system of partial differential equations whose unknowns are the area A, related to the pressure P by a constitutive vessel law, and the flow rate Q. In this first approach the vessel wall is modelled in order to produce an elastic and static reaction to a fluid action (*algebraic vessel law*) [77].

Chapter 2 is devoted to the numerical treatment of the 2×2 hyperbolic system. Among the possibilities offered by the literature [52, 76, 80] we have chosen a second order Taylor-Galerkin numerical scheme in a finite-element formulation, because of its satisfactory dispersion and dissipation properties. This scheme is stable under a CFL (Courant-Friedrichs-Lewy) condition that for realistic applications can be too restrictive (CFL number $< \frac{1}{\sqrt{3}}$). For this reason we derived a new scheme with a less restrictive CFL condition. Numerical test on the new scheme proposed are therein reported. Moreover the problem of the numerical treatment of boundary conditions is addressed.

As previously mentioned, in the basic model presented in *Chapter 1* the vessel wall is described by a simple algebraic law (the pressure is proportional to the wall displacement). In *Chapter 3* we extend this model to more complex and realistic vessel wall laws (where the pressure is linked to the wall displacement by a partial differential equation), taking into account other phenomena, such as wall inertia, viscoelasticity and longitudinal elasticity [79, 16]. In this case, it is still possible, at the cost of some simplifications in the model, to recover a system of two partial differential equations for A and Q. In this way it may be easily recognised that the wall inertia introduces a dispersive term in the equation, while viscoelasticity contributes with a diffusive operator. We present a numerical framework where these additional terms are handled by an operator splitting technique; in this way the solver based on a second order Taylor-Galerkin scheme and presented in *Chapter 2* is still used [29, 67]. Numerical tests are reported to exemplify the effect of the various terms on both pressure and flow pattern.

In *Chapter 4* we address a more complex geometry, taking into account abrupt variations of vessel wall properties (as occurs for instance in the case of a stent or an endograft) [32, 29, 14, 90, 67] as well as bifurcated channels [29, 92, 91, 62, 63, 67]. This last extension is, in particular, of crucial importance for the simulation of an arterial network. The two problems are very similar from a mathematical point of view and are handled by a domain decomposition technique [81] for which proper interface conditions have to be found. We present interface conditions that guarantee a global energy inequality. Details on the numerical scheme used to solve the interface problem are also furnished.
Finally the case of an endograft posed in the iliac bifurcation is presented. This test case is presented here with the aim of understanding how it can be treated by one dimensional models.

In *Chapter 5* a preliminary extension to the case of curved geometries is reported. The one dimensional model presented in *Chapter 1* is based on the assumption of a specific profile for the longitudinal component of the velocity, while the axial components are neglected. In the reduced models here presented we enrich the velocity field: the two components of the axial velocity are not neglected anymore and the component of velocity along the longitudinal axis is described, on each vessel section, by a higher order polynomial [38, 39, 85]. This allows the development of un-symmetric velocity profiles. We report here about some models developed for a straight geometry and the extension of them for a curved geometry (with constant curvature). These models are characterized by a weak imposition of the divergence constraint.
Some preliminary numerical results for curved geometries are also reported.

In the second part we consider an arterial tree featuring 55 arteries [105, 97, 104], described by the 1D model, coupled with lumped parameter models for heart and capillaries. As the one dimensional model has already been presented, here we address the methodology and the numerical methods behind the coupling (multiscale) problem (*Chapter 6*) and we present some numerical results for cases of clinical interest (*Chapter 7*).

Normally, the action of the heart is represented by a boundary conditon to be prescribed at the inlet of the first artery (the ascending aorta) of the network [91]. In *Chapter 6* we

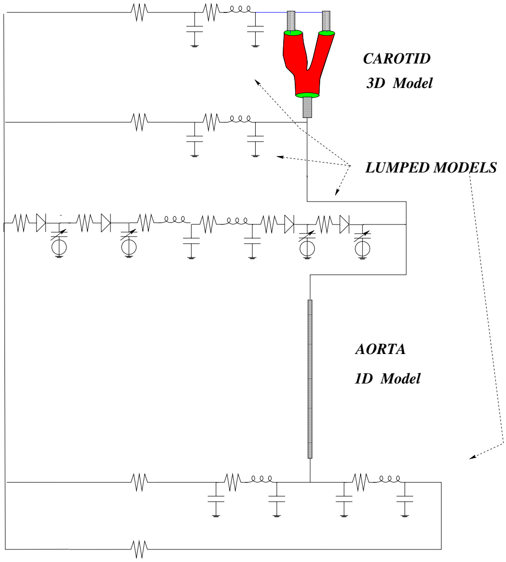

Figure 8: Multiscale approach for the human cardiovascular system. The one dimensional model is coupled with a lumped parameter model and a three dimensional Navier-Stokes fluid-structure interaction problem. This approach is completely modular in the sense that we can improve the local description using a more accurate model (figure taken from [33]).

show that the reduction of the heart action to a boundary condition for this system is unsatisfactory, in particular when studying the effect on the pressure and flow patterns caused by changes in the geometrical or mechanical characteristics of the arterial network (e.g. due to the presence of a prosthesis in the iliac bifurcation). No feedback from the arterial tree to the heart is indeed being modelled in this way. Therefore, we propose to overcome this drawback by a coupled description based on the matching of the 1D network model with a lumped parameter model for the left ventricle [30]. In particular, we use a varying elastance model presented in the literature [59, 45] together with a technique that accounts for the closure of the aortic valve.
At the outlet we use a Windkessel model to simulate the presence of small arteries and capillaries.

In *Chapter 7* the model presented in *Chapter 6* is tested and applied to some cases of physiological or pathological relevance.
It is well know that arterial stiffness increases with age [59]; this is reflected in suitable modifications of the parameter values of the numerical model. Hence, we first analyse the physiological case and the ageing effects, showing that our model is able to recover empirical results presented in literature [59]. In particular, we investigate the overload on the heart

induced by the backward waves, whose relevance is increased by the stiffening of the vessel walls.

Next, a pathological situation (an amputation, occurring for instance as a consequence of diabetes) is considered where anomalous pressure wave reflections could have some consequences on the heart. This pathological case can be described by a suitable modification of the computational domain.

Preliminary numerical results referring to such pathological case are presented.

Part I

One dimensional models for blood flow simulations

Chapter 1

Classical 1D models for straight vessels

Introduction

The aim of the Chapter is to give a presentation of the state of art of one dimensional modelling of blood flow in arteries.

A simple reduced (1D) model will be introduced to describe the flow motion in arteries and its interaction with the wall displacement. In the absence of branching, a short section of an artery may be considered as a cylindrical compliant tube. There are (at least) two possibilities of deriving reduced models: asymptotic analysis and averaging the Navier-Stokes equations on vessel sections.

In the first case, the Navier-Stokes equations are considered in non-dimensional form, a small parameter ϵ (e.g. the ratio of the radius of the vessel to the length) is introduced, and all terms of second order in ϵ are neglected; the reduced model follows by averaging the reduced equations and recasting them in dimensional form [15, 16].

In the second case, the reduced model is obtained by introducing some physical semplifications (the axial velocities are neglected and a profile is chosen for the longitudinal velocity) and averaging the Navier-Stokes equations [77] on each vessel section.

We will describe here in more details this second method, which is the one adopted in this work.

The resulting model consists of two partial differential equations whose unknowns are the area A, the pressure P, and the flow rate Q. This model is, then, coupled to the structure throught the pressure: here we assume a static linear dependence of the pressure on the vessel wall displacement.

Moreover we will report the most relevant theoretical results present in the literature about one dimensional models. At the end of the Chapter we will address the problem of boundary conditions.

The model derivation in Section 1.1 is taken from [29], while the theoretical results of Section 1.2 are mainly inspired by [77, 28, 15].

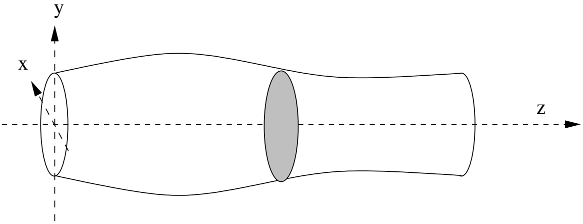

Figure 1.1: The cylindrical domain Ω_t. The cylinder axis is aligned with the coordinate z. The axial sections z =const. remain circular at all times.

1.1 One dimensional models

One dimensional models provide a simplified description of the flow motion in arteries and its interaction with the vessel wall displacement. Although unable to provide details on the flow field (such as recirculation or oscillating shear stresses), they can effectively describe the propagative phenomena due to the wall compliance. They are derived from the Navier Stokes equations

$$\begin{cases} \dfrac{\partial \mathbf{u}}{\partial t} + (\mathbf{u} \cdot \nabla)\,\mathbf{u} + \dfrac{1}{\rho}\nabla P - \operatorname{div}\left[\nu(\nabla \mathbf{u} + (\nabla \mathbf{u})^T)\right] = 0 \\ \operatorname{div}\,\mathbf{u} = 0 \end{cases} \quad \text{in } \Omega_t, t > 0, \tag{1.1.1}$$

posed on a cylindrical domain Ω_t which changes in time because of the flow induced wall movement. Here $\mathbf{u} = (u_x, u_y, u_z)$ is the fluid velocity, P denotes the pressure, ν is the kinematic viscosity and ρ the blood density; (x, y, z) is a system of Cartesian coordinates.

The complete derivation of one dimensional models can be found in [77] and is not repeated here. We just recall the main assumptions behind this derivation.

The domain, Ω_t, is a straight cylinder (with axis oriented along the coordinate z), as depicted in Fig. 1.1. It is comprised between $z = 0$ and $z = L$, L being the vessel length, taken to be constant in time. In the following, we will often employ cylindrical coordinates, denoted by (r, θ, z). We make the assumption of axial symmetry for all quantities involved. Furthermore, a wall displacement along the radial direction is considered. This implies that each axial section S remains circular at all times, i.e., for $z \in [0, L]$ and $t > 0$ we have

$$S = S(z,t) = \{(r, \theta, z) : 0 \leq r \leq R(z,t),\ 0 \leq \theta < 2\pi\},$$

where $R = R(z,t)$ is the vessel radius. The pressure is taken to be constant on each axial section and we assume that viscous effects are relevant only near the wall boundary. The component u_z is dominant with respect to u_x and u_y and furthermore we assume that it may be described in cylindrical coordinates as

$$u_z(r, z, t) = \overline{u}(z,t) s(\frac{r}{R(z,t)}),$$

where $\overline{u}$ is the average velocity on each axial section and $s : [0, R(z,t)] \to \mathbb{R}$ is a velocity profile (also called profile law).

The vessel wall is supposed to be impermeable, although seepage of fluid through the wall may be accounted for at the expense of a slight modification of the equations (see section 1.1.2).

By integrating (1.1.1) over a generic axial section $S(z,t)$ and taking advantage of the above assumptions, one finally obtains the following system

$$\frac{\partial A}{\partial t} + \frac{\partial Q}{\partial z} = 0 \tag{1.1.2}$$

$$\frac{\partial Q}{\partial t} + \frac{\partial}{\partial z}\left(\alpha \frac{Q^2}{A}\right) + \frac{A}{\rho}\frac{\partial P}{\partial z} + K_R \frac{Q}{A} = 0 \tag{1.1.3}$$

for all $z \in (0,L)$ where the unknowns A, Q and P (in the following we will also use the notation $p = \frac{P}{\rho}$) denote the section area, the averaged volumic flux and the mean pressure, respectively. They are defined as

$$\begin{aligned} A(z,t) &= \int_{S(z,t)} dx\,dy, \quad Q(z,t) = \int_{S(z,t)} u_z(x,y,z,t)dx\,dy, \\ P(z,t) &= (A(z,t))^{-1} \int_{S(z,t)} P(x,y,z,t)dx\,dy. \end{aligned} \tag{1.1.4}$$

Clearly we have $Q = A\overline{u}$. The coefficient α is the momentum correction coefficient (also called Coriolis coefficient), defined as

$$\alpha = \frac{\int_S u_z^2 dxdy}{A\overline{u}^2} = \frac{\int_S s^2\,dxdy}{A},$$

while K_R is a resistance parameter related to the viscosity of blood.

For a profile law of the form

$$s(r) = \zeta^{-1}(\zeta+2)(1-r^\zeta), \quad r = \sqrt{x^2+y^2}$$

with $\zeta > 0$, we have $\alpha = (\zeta+2)(\zeta+1)^{-1}$. In particular for a parabolic profile (Poiseuille flow) $\alpha = \frac{4}{3}$. In blood flow problems a flatter profile ($\zeta = 9$) is often preferred [95]. In this case $\alpha = 1.1$. Furthermore, $\alpha = 1$ is also often used, since it leads to simplifications in the mathematical formulation that will be detailed later on. As for the resistance parameter, a parabolic profile would provide $K_R = 8\pi\nu$, which is the value normally used, while for $\zeta = 9$ one would get $K_R = 22\pi\nu$.

Recently [16] self-consistent effective equations modelling blood flow in arteries have been derived. These new reduced models are obtained without any hypothesis on the velocity profile. In particular, in the resulting system, the velocity profile is obtained solving a partial differential equation.

1.1.1 Vessel wall law

To close our problem, (1.1.2) and (1.1.3), which is undetermined as it features three unknowns and only two equations, it is necessary to provide an additional relation. This is derived from the mechanical model for the vessel displacement. The vessel wall is a rather complex physical system: a biological description can be found in [42], [43], [44]. Therein some mathematical models are detailed.

Our starting point is the so-called generalised string model ([79], [77]), that can be easily obtained starting from the membrane equation (linearly elastic membranes are modeled by the Navier equations, see [49] or [53]), under the hypothesis that the longitudinal (along z) displacement of the wall is negligible.
It writes

$$\rho_w h_0 \frac{\partial^2 \eta}{\partial t^2} - \tilde{a}\frac{\partial^2 \eta}{\partial z^2} + \tilde{b}\eta - \tilde{c}\frac{\partial^3 \eta}{\partial t \partial z^2} = (P - P_{ext}). \tag{1.1.5}$$

Here, $\eta = R - R_0$ is the displacement of the vessel wall with respect to a reference configuration at the initial time t=0:

$$\Omega_0 = \{(r,\theta,z) : 0 \le r \le R_0(z),\, 0 \le \theta < 2\pi,\, 0 \le z \le L\}$$

which corresponds to that taken by the vessel when filled by a still fluid at pressure equal to the external pressure P_{ext} (here taken constant). Clearly

$$\eta = \frac{\sqrt{A} - \sqrt{A_0}}{\sqrt{\pi}}, \quad \text{with } A_0 = \pi R_0^2. \tag{1.1.6}$$

ρ_w is the vessel density, h_0 the wall thickness at the reference configuration, $\tilde{a}$, $\tilde{b}$ and $\tilde{c}$ three positive coefficients. In particular,

$$\tilde{b} = \frac{Eh_0}{\kappa R_0^2} = \frac{\pi E h_0}{\kappa A_0}, \tag{1.1.7}$$

where E is the Young modulus of elasticity and κ may take the value 1 or 3/4 depending on whether the assumption of uni-axial plane stresses is made in the derivation of the generalised string model. More details are found in [79] and [77]. Here we take $\kappa = 1$.
The partial differential equation (1.1.5) may be used to link the pressure with the vessel area and its time and spatial derivatives. However, its direct use in the context of our one dimensional model is problematic. The system formed by (1.1.3) and (1.1.5) (after having expressed the latter in terms of A by using (1.1.6)) would contain two evolution equations for the same unknown, the area A. Moreover, it is known that for the problem at hand, the elastic response is the dominating effect, while the other terms are less important. Consequently, a first model is obtained by neglecting all derivatives in (1.1.5) (see e.g. [66] or [77]). Pressure and area will then be related by an algebraic law of the type

$$P - P_{ext} = \tilde{b}\eta = \beta \frac{\sqrt{A} - \sqrt{A_0}}{A_0} \tag{1.1.8}$$

where

$$\beta = E h_0 \sqrt{\pi} \tag{1.1.9}$$

is in general a function of z because of possible spatial variations of the Young modulus E and the wall thickness h_0.
In general, an algebraic relationship between pressure and area may be written as

$$P = P_{ext} + \psi(A; A_0, \boldsymbol{\beta}) \tag{1.1.10}$$

where we have outlined that the pressure will also depend parametrically on A_0 and on a set of coefficients $\boldsymbol{\beta}$ which account for physical and mechanical characteristics. A_0 and $\boldsymbol{\beta}$ are given functions of z. It is required that ψ be (at least) a C^1 function of its arguments and be defined for all $A > 0$ and $A_0 > 0$. The range of variation of $\boldsymbol{\beta}$ will depend on the particular mechanical model chosen. Furthermore, for all allowable values of A, A_0 and $\boldsymbol{\beta}$ we must have

$$\frac{\partial \psi}{\partial A} > 0, \qquad \text{and } \psi(A_0; A_0, \boldsymbol{\beta}) = 0.$$

Various algebraic relations of the form (1.1.10) have been used for the development of one dimensional models of blood flow, the interested reader may refer to the cited reference. In this work we will restrict our selves to (1.1.8), i.e. $\psi = \beta \frac{\sqrt{A}-\sqrt{A_0}}{A_0}$, and $\boldsymbol{\beta}$ reduces to the single parameter β. Furthermore, for the sake of simplicity, and without loss of generality, we will assume $P_{ext} = 0$.

We will now focus on the differential problem obtained by substituting (1.1.8) into (1.1.3), and on its numerical solution, leaving to Chapter 4 the discussion on how to implement the other terms in (1.1.5) into the model.

1.1.2 One dimensional model with algebraic pressure law

By replacing (1.1.8) into (1.1.3), after some manipulation we obtain a system of differential equations which may be written in conservation form as

$$\frac{\partial \mathbf{U}}{\partial t} + \frac{\partial \mathbf{F}}{\partial z}(\mathbf{U}) = \mathbf{B}(\mathbf{U}) \tag{1.1.11}$$

where $\mathbf{U} = [A, Q]^T$ are the conservative variables, $\mathbf{F} = [F_1, F_2]^T$ are the corresponding fluxes and $\mathbf{B} = [B_1, B_2]^T$ are the source terms. Details may be found in [77]. More precisely, if we choose (1.1.8) as the pressure area relation, we have

$$\mathbf{F}(\mathbf{U}) = \begin{bmatrix} Q \\ \alpha \dfrac{Q^2}{A} + \dfrac{\beta}{3\rho A_0} A^{\frac{3}{2}} \end{bmatrix} \quad \text{and} \quad \mathbf{B}(\mathbf{U}) = \begin{bmatrix} 0 \\ -K_R \frac{Q}{A} \end{bmatrix}. \tag{1.1.12}$$

(1.1.11) can be rewritten as:

$$\frac{\partial \mathbf{U}}{\partial t} + \mathbf{H} \frac{\partial \mathbf{U}}{\partial z} = \tilde{\mathbf{B}}(\mathbf{U}) = \mathbf{B}(\mathbf{U}) - \frac{\partial \mathbf{F}}{\partial A_0} \frac{\partial A_0}{\partial z} - \frac{\partial \mathbf{F}}{\partial \beta} \frac{\partial \beta}{\partial z} \tag{1.1.13}$$

where

$$\mathbf{H}(\mathbf{U}) \; = \; \frac{\partial \mathbf{F}}{\partial \mathbf{U}} = \begin{bmatrix} \dfrac{\partial F_1}{\partial A} & \dfrac{\partial F_1}{\partial Q} \\ \dfrac{\partial F_2}{\partial A} & \dfrac{\partial F_2}{\partial Q} \end{bmatrix} = \begin{bmatrix} 0 & 1 \\ -\alpha \dfrac{Q^2}{A^2} + \dfrac{\beta}{2\rho A_0} A^{\frac{1}{2}} & 2\alpha \dfrac{Q}{A} \end{bmatrix}, \tag{1.1.14}$$

$$\tilde{\mathbf{B}}(\mathbf{U}) \; = \; \begin{bmatrix} 0 \\ -K_R \frac{Q}{A} + \frac{A}{A_0} \frac{h_0 \sqrt{\pi}}{\rho} \left(\frac{2}{3} A^{\frac{1}{2}} - A_0^{\frac{1}{2}} \right) \frac{\partial E}{\partial z} \\ \qquad - \frac{E h_0 \sqrt{\pi}}{\rho} \frac{A}{A_0^2} \left(\frac{2}{3} A^{\frac{1}{2}} - \frac{1}{2} A_0^{\frac{1}{2}} \right) \frac{\partial A_0}{\partial z} \end{bmatrix}. \tag{1.1.15}$$

The term $\frac{\partial A_0}{\partial z}$ in equation (1.1.13) accounts for a variation of the Area at rest, as occuring for instance in case of tapering or stenosis, while the term $\frac{\partial \beta}{\partial z}$ accounts for a variation of the

mechanical properties of the vessel.
Moreover we can add a seepage effect (mass losing effect) modifing the source term of the mass conservation equation. Equation (1.1.2) states the mass conservation and is modified by adding a source term

$$\frac{\partial A}{\partial t} + \frac{\partial Q}{\partial z} = -Y \tag{1.1.16}$$

with

$$Y = y_0 + k(\sqrt{A} - \sqrt{A_0}) \tag{1.1.17}$$

where y_0 and k are suitable constants to be empirically fitted. This seepage effect may be used either to simulate, in a rather crude way, the blood leaving the main vessel wall through lateral branches, or the arterial flow through the vessel wall in some smaller arteries such as those in the brain.

1.2 Some theoretical results

1.2.1 Analysis of characteristics

Consider system (1.1.13). By straightforward calculations we have the following expressions for the eigenvalues of $\mathbf{H}$

$$\lambda_{1,2} \;=\; \alpha\frac{Q}{A} \pm \sqrt{c_1^2 + \alpha(\alpha-1)\frac{Q^2}{A^2}} \quad , \qquad c_1 = \sqrt{\frac{\beta}{2\rho A_0}}A^{\frac{1}{4}} \tag{1.2.1}$$

Using the Cauchy-Schwarz inequality

$$A\bar{u} = \int_S u \leq \sqrt{A}\sqrt{\int_S u^2} \tag{1.2.2}$$

and therefore

$$A\bar{u}^2 \leq \int_S u^2, \tag{1.2.3}$$

leading to $\alpha \geq 1$. Consequently the two eigenvalues λ_1 and λ_2 are distinct and real: the system (1.1.13) is thence fully hyperbolic.
It is useful to rewrite it in a different manner, by diagonalising the matrix $\mathbf{H}$.
We indicate by $\mathbf{l}_1$ and $\mathbf{l}_2$ the two left eigenvectors of $\mathbf{H}$ and by $\mathbf{r}_1$ and $\mathbf{r}_2$ the rigth ones; moreover let $\mathbf{L}$ and $\mathbf{R}$ be the matrices formed by the left and right eigenvectors, respectively, and $\mathbf{\Lambda}$ the diagonal matrix formed by the eigenvalues.
If we normalise the eigenvectors ($\mathbf{LR} = \mathbf{I}$), we have

$$\mathbf{H} = \mathbf{R\Lambda L}.$$

Using these notations, system (1.1.13) is rewritten as

$$\frac{\partial \mathbf{U}}{\partial t} + \mathbf{R\Lambda L}\frac{\partial \mathbf{U}}{\partial z} = \mathbf{B}(\mathbf{U}) \tag{1.2.4}$$

Now, multiplying equation (1.2.4) by $\mathbf{L}$

$$\mathbf{L}\frac{\partial \mathbf{U}}{\partial t} + \mathbf{\Lambda L}\frac{\partial \mathbf{U}}{\partial z} = \mathbf{LB}(\mathbf{U}) \tag{1.2.5}$$

If there exists a quantity $\mathbf{W} = \mathbf{W}(\mathbf{U})$ such that

$$\frac{\partial \mathbf{W}}{\partial \mathbf{U}} = \mathbf{L} \tag{1.2.6}$$

equation (1.2.5) can be rewritten as

$$\frac{\partial \mathbf{W}}{\partial t} + \mathbf{\Lambda} \frac{\partial \mathbf{W}}{\partial z} = \mathbf{L}\mathbf{B}(\mathbf{U}) \tag{1.2.7}$$

In this way, the original system has been diagonalized. $\mathbf{W} = [W_1, W_2]^T$ are called characteristic variables.
In the case where $\mathbf{B} = 0$, this relation says that they are invariant along the two curves (in the (z,t) plane) described by the non-linear ordinary differential equations (see e.g. [36])

$$\frac{dY_1}{dt} = \lambda_1(Y_1, t) \qquad \text{and} \qquad \frac{dY_2}{dt} = \lambda_2(Y_2, t). \tag{1.2.8}$$

From equation (1.2.6) it follows (see [77]) that if the characteristic variables exist they must satisfy

$$\begin{array}{ll} \dfrac{\partial W_1}{\partial A} = \zeta[\sqrt{c_1^2 + \alpha(\alpha-1)\bar{u}^2} - (\alpha-1)\bar{u}] \quad , & \dfrac{\partial W_1}{\partial A} = \zeta A \\ \dfrac{\partial W_2}{\partial A} = \zeta[-\sqrt{c_1^2 + \alpha(\alpha-1)\bar{u}^2} - (\alpha-1)\bar{u}] \quad , & \dfrac{\partial W_2}{\partial A} = \zeta A \end{array}$$

where $\zeta = \zeta(A, \bar{u})$ is an integrating factor to be determined.
In the general case, the solution of this problem is not a simple task, but considering the special case $\alpha = 1$ leads to some simplifications. In this specific case, by straightforward calculations ([77]) one finally obtains the expressions for the two characteristic variables

$$W_{1,2} = \frac{Q}{A} \pm 4\sqrt{\frac{\beta}{2\rho A_0}} A^{\frac{1}{4}}. \tag{1.2.9}$$

These relations can be inverted to express the primitive variables in terms of the characteristic ones,

$$A = \left(\frac{2\rho A_0}{\beta}\right)^2 \frac{(W_1 - W_2)^4}{8^4}, \qquad Q = A\frac{(W_1 + W_2)}{2}. \tag{1.2.10}$$

1.2.2 Energy estimate

Defining a local energy e as

$$e = \frac{1}{2} A\bar{u}^2 + \frac{1}{\rho}\int_{A_0}^{A} \psi(\xi, A_0, \beta) d\xi$$

a global energy for the 1D model is given by

$$\epsilon(t) = \int_0^L e(t, z) dz, \qquad t \in I$$

Note that e is the sum of the kinetic energy and the elastic energy stored in the vessel wall. It has been proven in [28] that under some hypotheses (subcritical flow regimes, that is $\lambda_1 > 0$

and $\lambda_2 < 0$, and area A always positive) and in the special case of $\alpha = 1$, the following equality holds

$$\epsilon(t) + K_R \int_{t_0}^{t} \int_0^L \bar{u}^2 dz d\tau + \frac{1}{\rho} \int_{t_0}^{t} Q(P_t - P_{ext})|_0^L d\tau = \epsilon(t_0) \tag{1.2.11}$$

where $\epsilon(t_0)$ depends only on the initial data A^0 and Q^0, while $P_t = P + \frac{1}{2}\rho\bar{u}^2$ is the fluid total pressure. In equation (1.2.11) the first term at the left side represents the global energy of the 1D model, the second the energy dissipated and the third the energy ingoing and outgoing. In order to draw an energy inequality we need to investigate the sign of this last term, which will depend on the boundary conditions.
Further discussion can be found in [28].

1.2.3 Entropy

Let us consider the hyperbolic system written in quasi-linear form (1.1.13). We may have situations in which the weak solution is not unique: in this case an additional relation is required in order to select the physical solution. Typically in gas dynamics the physical quantity used is the entropy. For system (1.1.13) it is possible to define an entropy function for which an additional conservation law holds ([52, 36]).
Following [77] a pair of functions $e : \mathbb{R}^2 \to \mathbb{R}$ and $F_e : \mathbb{R}^2 \to \mathbb{R}$ is called an entropy pair for the system if e is a convex function of U (called entropy) and if the following condition is satisfied

$$(\frac{de}{dU})^T \mathbf{H}(\mathbf{U}) = \frac{\partial F_e}{\partial U} \tag{1.2.12}$$

for all the admissible values of U.
In the special case $\alpha = 1$

$$e = \frac{1}{2} A\bar{u}^2 + \frac{1}{\rho} \int_{A_0}^{A} \psi(\xi, A_0, \beta) d\xi \tag{1.2.13}$$

is indeed an entropy with associated flux

$$F_e = \frac{1}{\rho} Q(P_t - P_{ext}) \tag{1.2.14}$$

Further details can be found in [77].

1.2.4 Note on the regularity of the solution

As system (1.1.13) is hyperbolic and non-linear, one should expect to have shock development, as known from literature (i.e. see [52]).
In [15] a mathematical analysis is presented for the quasi-linear effects arising in a hyperbolic system of PDE modelling blood flow in arteries. That system differs from system (1.1.13) because the pressure-area relationship is taken to be linear. In particular it is shown that, in a healthy individual, shocks never occur for physiological vessel lengths and physiological pulse (the time and location of the first shock is there estimated at 2.8 m downstream from the inlet boundary).

1.3 Boundary conditions

As already seen in Section 1.2.1, the mathematical analysis of system (1.1.13) outlines its hyperbolic nature. The solution is, then, the non-linear superposition of two simple waves. The two eigenvalues λ_1 and λ_2, representing their velocity, are always of opposite sign for the flow regimes we are interested in. Hence, the differential problem needs exactly one boundary condition at $z = 0$ and at $z = L$ ([76]).

An important class of boundary conditions, is the one called non-reflecting, where only the information associated to the entering wave is prescribed (if $\lambda_1 > 0$ and $\lambda_2 < 0$, at $z = 0$ the incoming characteristic variable is W_1, while at $z = L$ is W_2).

This means that non-reflecting boundary conditions are of the form

$$W_1(t) = g_1(t), \quad \text{at } z = 0, \quad t > 0 \tag{1.3.1}$$

$$W_2(t) = g_2(t), \quad \text{at } z = L, \quad t > 0. \tag{1.3.2}$$

These conditions are admissible for the problem at hand.

The admissibility of a boundary condition for a non-linear hyperbolic system has been addressed in [25]; other references may be found in [36].

Equations (1.3.1) and (1.3.2) allow the wave associated to the outgoing characteristic to leave the domain. In particular, a boundary condition of this type is convenient at the distal section, when no specific information is given on pressure or flux variation. In this case $g_2(t)$ can be taken to be constant.

At inlet one normally aims at imposing values of pressure or mass flux, because empirical data are usually given in term of physical variables. In this case, in order to use equation (1.3.1) a way to construct $g_1(t)$ from physical data is needed (for a numerical approach see Section 2.2).

Chapter 2

Numerical approximations of 1D models

Introduction

In the previous Chapter, the classical one-dimensional model has been presented and analysed. The final model reduces to a 2×2 hyperbolic system.

In this Chapter the problem of the numerical solution of such a system will be addressed.

Among the possibilities proposed in the literature [52, 76, 80], we have chosen to use a Lax-Wendroff scheme, because it produces a moderate amount of numerical dispersion and dissipation. Moreover, we have chosen the finite element version (LW-FEM) of this numerical scheme instead of the finite difference version (LW-FDM), because of its lower numerical diffusion and dispersion (for more details see Chapter 8 of [76]).

In the first part of this Chapter a second-order Taylor-Galerkin (or LW-FEM) scheme is presented ([23, 9, 24, 20]); this scheme is stable under a CFL (Courant-Friedrichs-Lewy) condition which relates the time step to the space grid size. While the LW-FDM is stable if the CFL number is lower than 1, the CFL condition for the LW-FEM is more restrictive (CFL number $< \frac{1}{\sqrt{3}}$).

Therefore a possibility to improve this scheme, increasing the CFL number, is also discussed. This modified scheme, presented in Section 2.1.1 and analysed in Section 2.3.1, has been developed in collaboration with L. Formaggia.

The problem of how to treat boundary conditions numerically will be addressed in the second part.

2.1 Numerical Discretisation

System (1.1.11) is discretised using a second order Taylor-Galerkin scheme [23]. Its derivation is more complex here because of the presence of the source term.
To simplify notation, we will denote $\mathbf{F}_\mathbf{U} = \dfrac{\partial \mathbf{F}}{\partial \mathbf{U}}$ and $\mathbf{B}_\mathbf{U} = \dfrac{\partial \mathbf{B}}{\partial \mathbf{U}}$.

By recalling (1.1.11) we may write

$$\begin{aligned}
\frac{\partial \mathbf{U}}{\partial t} &= \mathbf{B} - \frac{\partial \mathbf{F}}{\partial z} && (2.1.1)\\
\frac{\partial^2 \mathbf{U}}{\partial t^2} &= \mathbf{B}_\mathbf{U}\frac{\partial \mathbf{U}}{\partial t} - \frac{\partial}{\partial z}\left(\mathbf{F}_\mathbf{U}\frac{\partial \mathbf{U}}{\partial t}\right) \\
&= \mathbf{B}_\mathbf{U}\left(\mathbf{B} - \frac{\partial \mathbf{F}}{\partial z}\right) - \frac{\partial(\mathbf{F}_\mathbf{U}\mathbf{B})}{\partial z} + \frac{\partial\left(\mathbf{F}_\mathbf{U}\frac{\partial \mathbf{F}}{\partial z}\right)}{\partial z} && (2.1.2)
\end{aligned}$$

We subdivide the time domain in time intervals (t^n, t^{n+1}), $n = 0, 1, ...$, with $t^n = \Delta t n$, Δt being the time step.
By performing a Taylor expansion around the solution $\mathbf{U}(t^n)$, we obtain

$$\begin{aligned}
\mathbf{U}(t^{n+1}) &= \mathbf{U}(t^n) + \left.\frac{\partial \mathbf{U}}{\partial t}\right|_{t^n}\Delta t + \left.\frac{\partial^2 \mathbf{U}}{\partial t^2}\right|_{t^n}\frac{\Delta t^2}{2} + O(\Delta t^3) && (2.1.3)\\
&= \mathbf{U}(t^n) + \Delta t\left(\mathbf{B}(t^n) - \frac{\partial \mathbf{F}(t^n)}{\partial z}\right) + \frac{\Delta t^2}{2}\left[\mathbf{B}_\mathbf{U}(t^n)\mathbf{B}(t^n) - \mathbf{B}_\mathbf{U}(t^n)\frac{\partial \mathbf{F}(t^n)}{\partial z}\right.\\
&\quad \left. -\frac{\partial}{\partial z}\left(\mathbf{F}_\mathbf{U}(t^n)\mathbf{B}(t^n)\right) + \frac{\partial}{\partial z}\left(\mathbf{F}_\mathbf{U}(t^n)\frac{\partial \mathbf{F}(t^n)}{\partial z}\right)\right] + O(\Delta t^3) && (2.1.4)
\end{aligned}$$

This suggests the use of the following approximation $\mathbf{U}^{n+1}$ of $\mathbf{U}(t^{n+1})$, from the known value of $\mathbf{U}^n$:

$$\begin{aligned}
\mathbf{U}^{n+1} &= \mathbf{U}^n - \Delta t\frac{\partial}{\partial z}\left[\mathbf{F}^n + \frac{\Delta t}{2}\mathbf{F}^n_\mathbf{U}\mathbf{B}^n\right] - \frac{\Delta t^2}{2}\left[\mathbf{B}^n_\mathbf{U}\frac{\partial \mathbf{F}^n}{\partial z} - \frac{\partial}{\partial z}\left(\mathbf{F}^n_\mathbf{U}\frac{\partial \mathbf{F}^n}{\partial z}\right)\right]\\
&\quad + \Delta t\left(\mathbf{B}^n + \frac{\Delta t}{2}\mathbf{B}^n_\mathbf{U}\mathbf{B}^n\right), && (2.1.5)
\end{aligned}$$

where $\mathbf{U}^0$ is provided by the initial conditions and $\mathbf{F}^n$ stands for $\mathbf{F}(\mathbf{U}^n)$ (similar notations hold for $\mathbf{F}^n_\mathbf{U}$ and $\mathbf{B}^n$, $\mathbf{B}^n_\mathbf{U}$).
The space discretisation is carried out using the finite element method. The interval $[0, L]$ is divided into N elements $[z_i, z_{i+1}]$ with $i = 0, ..., N$ and we will indicate by h_i the local element size. We indicate by V_h the space of piecewise linear finite element functions, by $\mathbf{V}_h = [V_h]^2$ and by $\mathbf{V}^0_h$ the set formed by functions of $\mathbf{V}_h$ which are zero at $z = 0$ and $z = L$. Further, we indicate by

$$(\mathbf{u}, \mathbf{v}) = \int_0^L \mathbf{u} \cdot \mathbf{v} dz$$

the L^2 scalar product for vector functions.

Using the abridged notations $\mathbf{F}_{LW} = \mathbf{F}(\mathbf{U}_h) + \frac{\Delta t}{2}\mathbf{F}_{\mathbf{U}}(\mathbf{U}_h)\mathbf{B}(\mathbf{U}_h)$ and $\mathbf{B}_{LW} = \mathbf{B}(\mathbf{U}_h) + \frac{\Delta t}{2}\mathbf{B}_{\mathbf{U}}(\mathbf{U}_h)\mathbf{B}(\mathbf{U}_h)$, the finite element fomulation of (2.1.5) is :
for $n \geq 0$, find $\mathbf{U}_h^{n+1} \in \mathbf{V}_h$ which satisfies

$$\begin{aligned}(\mathbf{U}_h^{n+1}, \psi_h) &= (\mathbf{U}_h^n, \psi_h) + \Delta t\left(\mathbf{F}_{LW}, \frac{\partial \psi_h}{\partial z}\right) - \frac{\Delta t^2}{2}\left(\mathbf{B}_{\mathbf{U}}^n \frac{\partial \mathbf{F}^n}{\partial z}, \psi_h\right) \\ &\quad -\frac{\Delta t^2}{2}\left(\mathbf{F}_{\mathbf{U}}^n \frac{\partial \mathbf{F}^n}{\partial z}, \frac{\partial \psi_h}{\partial z}\right) + \Delta t\,(\mathbf{B}_{LW}^n, \psi_h)\,, \ \forall \psi_h \in \mathbf{V}_h^0 \qquad (2.1.6)\end{aligned}$$

plus the boundary and compatibility conditions which will be discussed in the next section.

This second order Taylor-Galerkin scheme (2.1.6) entails a time step limitation. A linear stability analysis [74] indicates that the following condition should be satisfied

$$\Delta t \leq \frac{\sqrt{3}}{3} \min_{0 \leq i \leq N}\left[\frac{h_i}{\max(\lambda_{1,i}, \lambda_{1,i+1})}\right], \qquad (2.1.7)$$

where $\lambda_{1,i}$ here indicates the value of λ_1 at mesh node z_i. This condition corresponds to a CFL number of $\frac{\sqrt{3}}{3}$, typical of a second order Taylor-Galerkin scheme in one dimension [74].

Moreover it should be noticed that this numerical scheme can be easily implemented in parallel, as done in [47].

2.1.1 Improving the numerical scheme

A third order (in time) scheme may be derived as well following the indications in [9].
Instead of the second order expansion(2.1.3) we can consider a third order one:

$$\mathbf{U}(t^{n+1}) = \mathbf{U}(t^n) + \left.\frac{\partial \mathbf{U}}{\partial t}\right|_{t^n} \Delta t + \left.\frac{\partial^2 \mathbf{U}}{\partial t^2}\right|_{t^n} \frac{\Delta t^2}{2} + \left.\frac{\partial^3 \mathbf{U}}{\partial t^3}\right|_{t^n} \frac{\Delta t^3}{6} + O(\Delta t^4) \qquad (2.1.8)$$

We rewrite the third order derivative as:

$$\left.\frac{\partial^3 \mathbf{U}}{\partial t^3}\right|_{t^n} \approx \frac{\theta}{\Delta t}\left(\left.\frac{\partial^2 \mathbf{U}}{\partial t^2}\right|_{t^{n+1}} - \left.\frac{\partial^2 \mathbf{U}}{\partial t^2}\right|_{t^n}\right) \qquad (2.1.9)$$

where θ is a parameter. Evidently, only for $\theta = 1$ we can have a third order scheme for $\mathbf{U}(t^{n+1})$.

This family of schemes implies the implicit treatment of the term $\frac{\partial^2 \mathbf{U}}{\partial t^2}$, which is approximated as follows:

$$\begin{aligned}\left.\frac{\partial^2 \mathbf{U}}{\partial t^2}\right|_{t^{n+1}} &\approx \mathbf{B}_{\mathbf{U}}^n\left(\mathbf{B}^{n+1} - \frac{\partial \mathbf{F}^{n+1}}{\partial z}\right) - \frac{\partial \mathbf{F}_{\mathbf{U}}^n \mathbf{B}^n}{\partial z} + \frac{\partial}{\partial z}\left(\mathbf{F}_{\mathbf{U}}^n \frac{\partial \mathbf{F}^{n+1}}{\partial z}\right) \\ &\approx \mathbf{B}_{\mathbf{U}}^n\left(\mathbf{B}^{n+1} - \mathbf{F}_{\mathbf{U}}^n \frac{\partial \mathbf{U}^{n+1}}{\partial z}\right) - \frac{\partial \mathbf{F}_{\mathbf{U}}^n \mathbf{B}^n}{\partial z} + \frac{\partial}{\partial z}\left((\mathbf{F}_{\mathbf{U}}^n)^2 \frac{\partial \mathbf{U}^{n+1}}{\partial z}\right) \qquad (2.1.10)\end{aligned}$$

With these approximations we lose the third order.
The main idea, reported in [9], is to use relation (2.1.8) in order to get an unconditionally

stable scheme for a set of θ values.
Following the same idea, we modify our scheme (2.1.6) as follows:

$$\begin{aligned}(\mathbf{U}_h^{n+1},\psi_h)+\frac{\Delta t^2}{6}\theta\left((\tilde{\mathbf{F}}_{\mathbf{U}})^2\frac{\partial\mathbf{U}_h^{n+1}}{\partial z},\frac{d\psi_h}{dz}\right)&=(\mathbf{U}_h^n,\psi_h)+\Delta t\left(\mathbf{F}_{LW}(\mathbf{U}_h^n),\frac{d\psi_h}{dz}\right)-\\ &\frac{\Delta t^2}{2}\left(\mathbf{B}(\mathbf{U}_h^n)\frac{\partial\mathbf{F}(\mathbf{U}_h^n)}{\partial z},\psi_h\right)-\frac{\Delta t^2}{2}\left(\mathbf{F}_{\mathbf{U}}(\mathbf{U}_h^n)\frac{\partial\mathbf{F}(\mathbf{U}_h^n)}{\partial z},\frac{d\psi_h}{dz}\right)+\\ &\Delta t\,(\mathbf{B}_{LW}\mathbf{U}_h^n,\psi_h)+\frac{\Delta t^2}{6}\theta\left((\tilde{\mathbf{F}}_{\mathbf{U}})^2\frac{\partial\mathbf{U}_h^{n+1}}{\partial z},\frac{d\psi_h}{dz}\right)\end{aligned}\qquad(2.1.11)$$

where $\tilde{\mathbf{F}}_{\mathbf{U}}$ is a piecewise constant approximation of $\mathbf{F}_{\mathbf{U}}(\mathbf{U}_h^n)$ to be suitably defined. Remark that for $\theta=0$ we re-obtain the previous second-order scheme.
Instead of using the θ optimal for accuracy we would like to find out for which values of θ we have a better stability condition. For that purpose, we perform a Von Neumann analysis on the linear equation:

$$\frac{\partial u}{\partial t}+a\frac{\partial u}{\partial z}=0\qquad(2.1.12)$$

discretised in time as follows:

$$u^{n+1}-\frac{\Delta t^2}{6}\theta\tilde{a}^2\frac{\partial^2u^{n+1}}{\partial z^2}=u^n-\Delta ta\frac{\partial u^n}{\partial z}+\frac{\Delta t^2}{2}a^2\frac{\partial^2u^n}{\partial z^2}-\frac{\Delta t^2}{6}\theta\tilde{a}^2\frac{\partial^2u^n}{\partial z^2}\qquad(2.1.13)$$

The analysis yields that for $\tilde{a}=a$ and $\theta\geq\frac{3}{2}$ we have an unconditionally stable scheme. For $\tilde{a}\neq a$ we still have a CFL condition, better than the old one and always bigger. Moreover for $\theta=\frac{3}{2}$ the scheme is still zero dissipative.
Next, we need to specify the choice of $\tilde{\mathbf{F}}_{\mathbf{U}}$ for the equation at hand. We recall that $\tilde{\mathbf{F}}_{\mathbf{U}}$ is an approximation of $\mathbf{F}_{\mathbf{U}}(\mathbf{U})$. Considering that

$$\mathbf{F}_{\mathbf{U}}(\mathbf{U})^2\;=\;\begin{bmatrix}-\alpha\dfrac{Q^2}{A^2}+\dfrac{\beta}{2\rho A_0}A^{\frac{1}{2}} & 2\alpha\dfrac{Q}{A}\\ (2\alpha\dfrac{Q}{A})(-\alpha\dfrac{Q^2}{A^2}+\dfrac{\beta}{2\rho A_0}A^{\frac{1}{2}}) & (4\alpha^2-1)\dfrac{Q^2}{A^2}+\dfrac{\beta}{2\rho A_0}A^{\frac{1}{2}}\end{bmatrix},\qquad(2.1.14)$$

reasonable approximation reads

$$(\tilde{\mathbf{F}}_{\mathbf{U}})^2\;=\;\begin{bmatrix}\dfrac{\beta}{2\rho A_0^{\frac{1}{2}}} & 0\\ 0 & \dfrac{\beta}{2\rho A_0^{\frac{1}{2}}}\end{bmatrix}.\qquad(2.1.15)$$

The computational advantage of this choice is evident: the two equations are still completely decoupled and $\tilde{\mathbf{F}}_{\mathbf{U}}$ does not depend on $\mathbf{U}$ anymore.

2.2 Boundary and compatibility conditions

Although the differential problem requires only one boundary condition at each end of the tube, the solution of the numerical problem requires to prescribe a full set of values for A

and Q at the first and last node. We need two extra relations, which are provided by the differential equations 'projected' along the direction of the outgoing characteristics, i.e.

$$\begin{aligned} \mathbf{l}_1^T\left(\frac{\partial \mathbf{U}}{\partial t}+\frac{\partial \mathbf{F}}{\partial z}(\mathbf{U})-\mathbf{B}(\mathbf{U})\right)&=0, \qquad z=0,\, t>0 \\ \mathbf{l}_2^T\left(\frac{\partial \mathbf{U}}{\partial t}+\frac{\partial \mathbf{F}}{\partial z}(\mathbf{U})-\mathbf{B}(\mathbf{U})\right)&=0, \qquad z=L,\, t>0. \end{aligned} \tag{2.2.1}$$

These compatibility relations could be discretised by adopting the same basic scheme as the differential problem. However, this would result in relations that couple the values of A_h^{n+1} and Q_h^{n+1} at the vessel ends. Since it is desirable for computational reasons to maintain two decoupled discrete systems for the evolution of area and mass flow, we have here resorted to a strategy to handle the compatibility relations called "characteristic extrapolation". It is based on the well known fact that the characteristic variables satisfy a system of ordinary differential equations along the characteristic path (1.2.8).

Indeed, when $\mathbf{B}(\mathbf{U})=0$ the characteristic variables are constant along the characteristics, so a first order approximation of the outgoing characteristic variables at time t^{n+1} and $z=0$ and $z=L$, respectively, is provided by

$$W_2^{n+1}(0)=W_2^n(-\lambda_2^n(0)\Delta t), \quad W_1^{n+1}(L)=W_1^n(L-\lambda_1^n(L)\Delta t).$$

A second order approximation might be obtained by following the technique described in [13]. When $\mathbf{B}(\mathbf{U})\neq 0$ the values of $W_2^{n+1}(0)$ and $W_1^{n+1}(L)$ will have to be computed by numerically solving the associated ODE system; for instance we solve it using an explicit Euler scheme. The values of $W_2^{n+1}(0)$ and $W_1^{n+1}(L)$ together with the boundary conditions effectively complement the discrete system provided by (2.1.6).

Again, if the characteristic variables are not available, the pseudo-characteristics may be used instead [76]. Considering equation (1.1.13) we evaluate $\mathbf{H}$ at the time step t^n; thence it is possible to numerically compute the eigenvectors and to construct the matrix $\mathbf{L}$, by which we can easily obtain the pseudo-characteristic variables ($\mathbf{W}=\mathbf{L}^n\mathbf{U}^n$).

From now on we assume $\alpha=1$, so the characteristic variables are given by (1.2.9).

When solving a real problem typically one has the pressure as input data. This is convenient for our problem, because this data is an admissible condition. Yet, sometimes it is not correct to impose the pressure directly, because this is a reflecting boundary condition and any imprecision in the pressure data will produce spurious wave reflections. In these cases we can resort to absorbing boundary conditions by prescribing the entering characteristic variable (see Section 1.3). Consider the case of a tube of length 10 cm where we impose total reflecting boundary condition at the outlet, as it would occurr, for instance, in a totally occluded artery. Suppose that we have the measured pressure at inlet for the same healthy artery. If we impose at inlet the measured pressure, we will find as a result a wave moving forward and, once the end is reached, reflected and going backward. When arriving again at inlet, the wave will not leave the tube but will be partially reflected. This is due to the fact that imposing a physical variable results in coupling the two characteristics variables. One may argue that if we have the exact pressure values at inlet the possible reflections are physical. Yet, the boundary data available in practice is often imprecise. Thus, the reflections will mainly be not physical and are better avoided. We will see, later on, situations where instead it is important to correctly reproduce the reflected wave (Chapter 6).

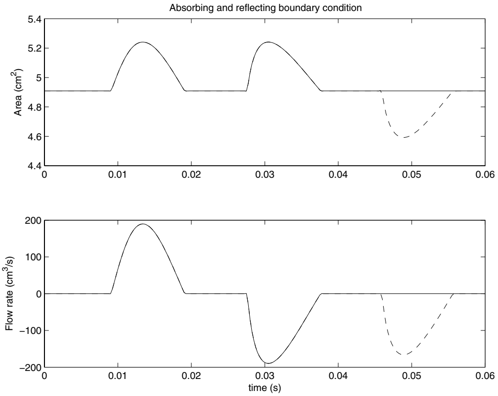

Figure 2.1: Time history for the physical variables in the middle point of a tube of length 10 *cm*; the solid line represents the solution obtained by using absorbing boundary condition while the discontinuous one is obtained by the reflecting boundary condition. They are superimposed and coincide almost everywhere, apart for the appearance of the reflected wave in the latter case.

An alternative way would be to give at inlet the characteristic variable. The problem is then how to construct a characteristic variable capable to impose, even if approximately, the pressure data.

Using the relations seen in Section 1.2.1 we may write W_1 as a function of W_2 and $P(t)$

$$W_1(t) = W_1(W_2(t), P(t)), \text{ at } z = 0, \qquad t > \bar{t}.$$

Here $P(t)$ represents the pressure profile prescribed at inlet.
As we want to decouple W_1 from W_2 we make the following approximation $W_2(t) = W_2(\bar{t})$, $\forall t$, where $\bar{t}$ is a fixed time, i.e. the starting time.
Then at each time step we compute

$$W_1(t^n) = W_1(W_2(\bar{t}), P(t^n)).$$

Figure 2.1 represents the time solution in the middle of the tube for the experiment described above, while in Figure 2.2 the characteristic variables are reported. We consider the result reported in Figure 2.1 for the reflecting boundary condition; it shows 3 waves: the first one traveling forward, the second one backward and a third one forward again. This last wave is due to the reflecting boundary condition imposed at inlet. In fact imposing physical condition results in a coupling of the two characteristic variables, giving as a result an entering W_1 when W_2 is outgoing (see Figure 2.2).

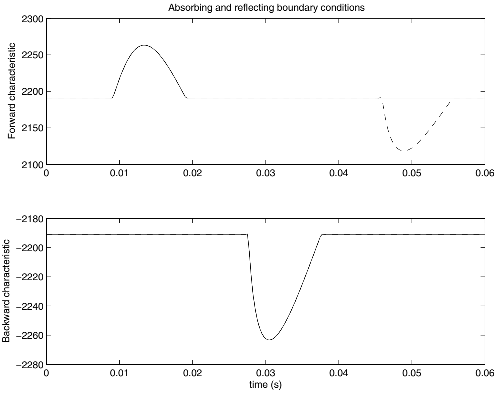

Figure 2.2: Time history for the characteristics variables in the middle point of a tube of lenght 10 cm; the solid line represents the solution obtained by using absorbing boundary condition while the discontinuous one is obtained by the reflecting boundary condition. They are superimposed and coincide almost everywhere, apart for the appearance of the reflected wave in the latter case.

2.3 Code validation

In order to asses the numerical scheme presented in Section 2.1.6, it has been verified in some selected cases that the numerical solution satisfies the energy equality (1.2.11).

In Figure 2.3 we report the energy (left term of energy equality) for a tube of 60 cm of length. At inlet, a single pulse (half sine) representing the incoming characteristic variable is imposed, while at outlet a non-reflecting boundary condition is imposed. In this test the fluid viscosity is set to zero, so the second term of equation (1.2.11) disappears. In the solution represented in Figure 2.3 we can distinguish 3 regions: in the first one the energy decreases because of the boundary term in equation (1.2.11); in the second one the energy is negative and costant, being the boundary term zero and being the energy dissipation caused by the fluid viscosity neglected; finally in the third region the energy decreases again because the traveling wave is outgoing.

In Figure 2.4 we report again the energy for a tube of 60 cm, but with different boundary conditions. At inlet we imposed $P + \frac{\rho}{2}u^2 = 0$, while at outlet $Q = 0$. These conditions guarantee that the boundary term in the energy inequality (equation 1.2.11) is always null, thus the system energy is positive and decreasing.

These results show that our numerical solution is in accordance with the predicted theoretical estimates (see Section 1.2.2).

Moreover our numerical scheme was compared with a discontinuous Galerkin method ([92, 89]). The comparison is described in detail in [67] and shows very good agreement between the two numerical schemes.

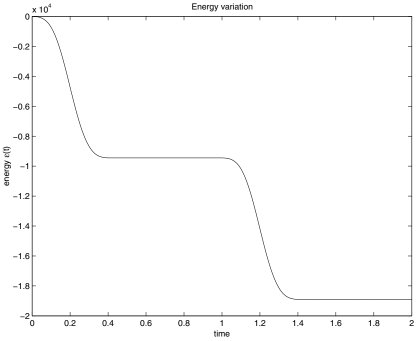

Figure 2.3: Computed energy for the 1D model. At inlet, a single pulse (half sine) representing the incoming characteristic variable is imposed, while at outlet a non-reflecting boundary condition is imposed.

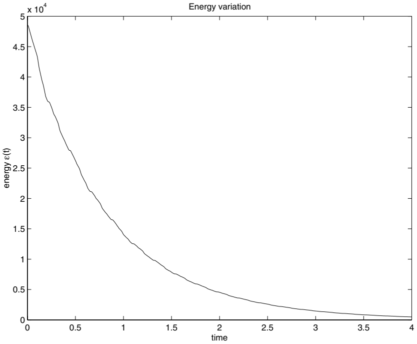

Figure 2.4: Computed energy for the 1D model. At inlet we imposed $P + \frac{\varrho}{2}u^2 = 0$, while at outlet $Q = 0$.

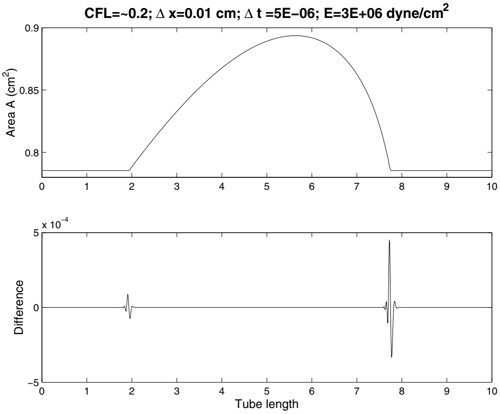

Figure 2.5: Difference between classical and modified Lax-Wendroff schemes, for a fixed CFL condition (CFL number ≈ 0.2). In the upper part the solution at a fixed time is represented. For this simulation a time step Δt of 0.000005 s and a space discretization Δx of 0.01 cm.

2.3.1 Numerical experiments on the modified scheme

Numerical tests have been performed in order to study the stability, the dispersion and the dissipation properties of the modified scheme (Section 2.1.1).
In particular we have considered 2 arteries of length 10 and 30 cm, where an ingoing wave (a half sine pulsed wave) is imposed on the characteristic variables. Figure 2.5 shows a comparison between the Lax-Wendroff scheme and the modified one presented here: at the same CFL value the two solutions are very close. It is interesting to note that we can improve the CFL number with the modified scheme, thus increasing the time step Δt (see equation (2.1.7)). In Figure 2.6 a comparison between two different CFL numbers is reported for the modified scheme. As we expect there are some dispersion effects when we increase the CFL number. This is highlighted in Figure 2.7 where the results for 3 different CFL numbers are reported (selected zones are enlarged in Figures 2.8 and 2.9); yet we increased the CFL number acting on the time step.
The numerical experiments suggest that with the modified scheme and a physiological value for the Young's modulus ($E \backsim 3\ 10^6\ dyne/cm^2$) we can increase the CFL number to around 1.

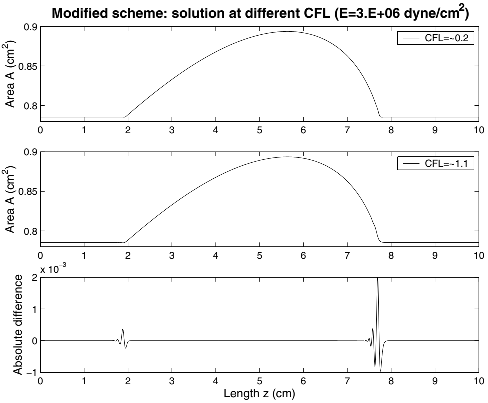

Figure 2.6: Modified scheme: degradation of the solution for different CFL values. Same test case as in Figure 2.5. The case with increased CFL number is obtained taking a $\Delta t = 0.000025$ s.

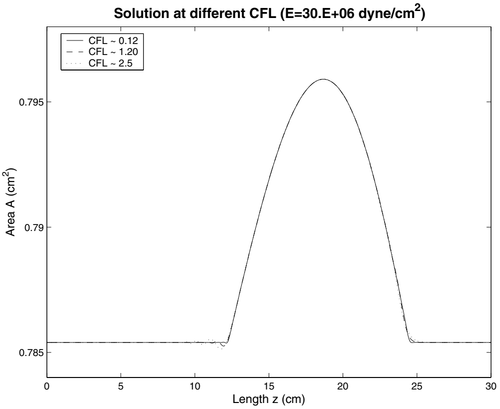

Figure 2.7: Modified scheme: degradation of the solution for different CFL values. The picture shows three solution at a fixed time for three different CFL numbers. At bigger CFL numbers dispersion phenomena are present (see also Figure 2.8).

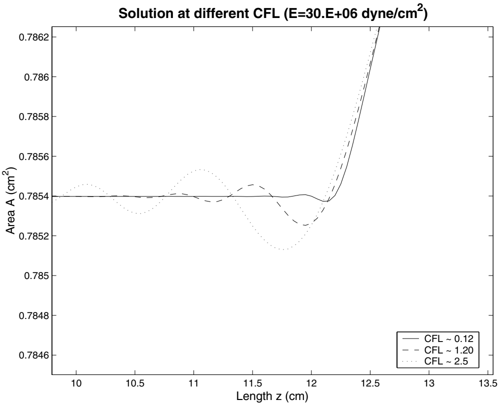

Figure 2.8: Modified scheme: zoom of a significative zone of figure 2.7.

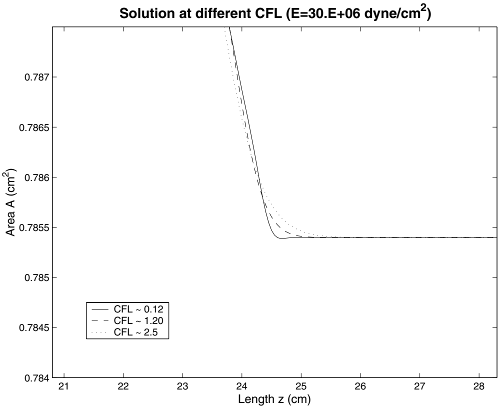

Figure 2.9: Modified scheme: zoom of a significative zone of figure 2.7.

Chapter 3

More realistic wall laws

Introduction

In Section 1.1 we have recalled the basic 1D model for a single arterial element, where the artery is approximated by a straight cylinder filled with blood. The main unknowns of the resulting system of two partial differential equations are the mean pressure P and the mass flux Q across the vessel axial sections as well as the area A of the section. An additional relation between P and A provides the way of closing the problem. The algebraic law (1.1.8) corresponds to the hypothesis of instantaneous static equilibrium for the vessel wall and leads to system (1.1.11).

In reality the wall of an artery is a very complex physical system as shown for example in [42, 43, 79]. Here we consider a more complex vessel dynamics, described by the differential equation (1.1.5), the so-called generalised string model [79]. This model can be derived starting from the Navier equations for a membrane (see e.g. [53, 49] for the model and [79, 16] for the derivation).

In this case, it is still possible, at the price of some simplifications in the model, to recover a system of two partial differential equations for A and Q, as already illustrated in [33]. In this way it may be easily recognised that the wall inertia introduces a dispersive term in the equation, while viscoelasticity contributes with a diffusive operator. Here, we present a numerical framework where these additional terms are handled by an operator splitting technique. Numerical tests will exemplify the effect of the various terms on the pressure and flow pattern.

The results reported in this Chapter have been published in the papers [29] and [67].

3.1 More complex wall models

The mechanical model used in Chapter 1 to describe the vessel wall dynamics was based on the assumption of an instantaneously elastic equilibrium, according to which the vessel wall responds to a change in the fluid pressure by adapting its section area, following a perfectly elastic law.

In reality, the mechanical behaviour of an arterial wall is much more complex. Although it is arguable whether there is a need for a sophisticated mechanical modelling when so many simplifications have already been made both at the geometrical and at fluid-dynamics level, improving the structural description may serve several purposes:

- to study the overall effects on the flow field of the different physical terms that might be included, such as wall inertia, viscoelasticity and pre-stress state;
- to verify the relevance of these terms for the problem at hand on the basis of realistic physiological or pathological values of the various coefficients.

The structural model will be obtained from the general equilibrium laws by imposing geometrical simplifications consistent with those used to derive the flow equations. In particular, we consider displacements η in the radial direction only. This is a reasonable assumption since some recent results [72] using membrane models for the wall structure which account for the effects of transversal displacements show that these are negligible.

The differential equation we will consider is in fact the generalised string model (1.1.5), where we substitute the second viscoelastic term by a simpler one, based on the De Voigt viscoelastic model (see [35]). It reads

$$\rho_w h_0 \frac{\partial^2 \eta}{\partial t^2} - \tilde{a}\frac{\partial^2 \eta}{\partial z^2} + \tilde{\gamma}\frac{\partial \eta}{\partial t} + \tilde{b}\eta = (P - P_{ext}). \tag{3.1.1}$$

To obtain an equation in terms of A we recall that $A = A_0 + \pi\eta^2$ and we linearise the time derivatives, following [33], as follows

$$\frac{\partial \eta}{\partial t} \simeq \frac{1}{2\sqrt{A_0}\sqrt{\pi}}\frac{\partial A}{\partial t} \tag{3.1.2}$$

$$\frac{\partial^2 \eta}{\partial t^2} = \frac{1}{\sqrt{\pi}}\frac{\partial^2}{\partial t^2}\left(\sqrt{A} - \sqrt{A_0}\right) \simeq \frac{1}{2\sqrt{\pi A_0}}\frac{\partial^2 A}{\partial t^2}. \tag{3.1.3}$$

Therefore, the adopted model may be written as

$$m\frac{\partial^2 A}{\partial t^2} - \gamma\frac{\partial A}{\partial t} - a\frac{\partial^2}{\partial z^2}(\sqrt{A} - \sqrt{A_0}) + \beta\frac{\sqrt{A} - \sqrt{A_0}}{A_0} = P, \tag{3.1.4}$$

where we have taken, as before, $P_{ext} = 0$ and

$$m = \frac{\rho_w h_0}{2\sqrt{\pi}\sqrt{A_0}}, \quad \gamma = \frac{\tilde{\gamma}}{2\sqrt{\pi}\sqrt{A_0}}, \quad a = \frac{\tilde{a}}{\sqrt{\pi}},$$

while β is still given by (1.1.9).

This model should be integrated with the fluid equations (1.1.2) and (1.1.3). The objective is to retain the basic two-equations structure of the model. Furthermore, we will assume that the additional terms are of less importance than the basic elastic response function $\beta\frac{\sqrt{A}-\sqrt{A_0}}{A_0}$ considered in the derivation of the previous model. This assumption permits the use of an operator splitting procedure for the numerical approximation.

The coupling between (1.1.2, 1.1.3) and (3.1.4) is given through the pressure term $\frac{A}{\rho}\frac{\partial}{\partial z}(P - P_{ext})$ in the momentum equation. Therefore, the continuity equation (1.1.2) will remain unaltered and, following [33], we will use it to replace the time derivatives of A with the space derivative of Q.

We are mainly interested in identifying the effects of the additional extra terms on the vessel mechanics. In the next sections we will systematically analyse the effect of each of the added terms.

3.1.1 Wall inertia term

The inertia term accounts for the wall mass and its acceleration: using physical arguments we can argue that it will be important only in case of large vessel masses and/or high frequency waves (big acceleration). In these cases we expect oscillations to occur at a frequency dependent on the wave length.

The contribution of this term in the momentum equation can be written, using the continuity equation, as

$$\frac{A}{\rho}\frac{\partial}{\partial z}\left(m\frac{\partial^2 A}{\partial t^2}\right) = -\frac{Am}{\rho}\frac{\partial^3 Q}{\partial t \partial z^2}. \tag{3.1.5}$$

System (1.1.11), augmented by the inertia term would then read

$$\begin{cases} \dfrac{\partial A}{\partial t} + \dfrac{\partial Q}{\partial z} = 0 \\ \dfrac{\partial Q}{\partial t} + \dfrac{\partial}{\partial z}F_2(A,Q) - \dfrac{Am}{\rho}\dfrac{\partial^3 Q}{\partial t \partial z^2} = B_2(A,Q), \end{cases} \tag{3.1.6}$$

where $F_2(A,Q)$ and $B_2(A,Q)$ denote the second component of the flux $\mathbf{F}$ and of the source term $\mathbf{B}$, respectively.

The differential system (3.1.6) may be written by splitting the flow rate $Q = \widehat{Q} + \widetilde{Q}$, where $\widehat{Q}$ and $\widetilde{Q}$ are implicitly defined through the set of equations

$$\begin{cases} \dfrac{\partial A}{\partial t} + \dfrac{\partial Q}{\partial z} = 0 \\ \dfrac{\partial \widehat{Q}}{\partial t} + \dfrac{\partial}{\partial z}F_2(A,Q) = B_2(A,Q) \\ \dfrac{\partial \widetilde{Q}}{\partial t} - \dfrac{Am}{\rho}\dfrac{\partial^3 Q}{\partial t \partial z^2} = 0. \end{cases} \tag{3.1.7}$$

This allows us to devise the following operator splitting strategy. On each time interval $[t^n, t^{n+1}]$, $n \geq 0$, system $(3.1.7)_{1,2}$ is solved by the Taylor-Galerkin scheme described in Section 2.1.6 and we correct the mass flux by employing equation $(3.1.7)_3$. More precisely, the adopted finite element formulation for the latter equation reads: given A_h^{n+1} and $\widehat{Q}_h^{n+1}$,

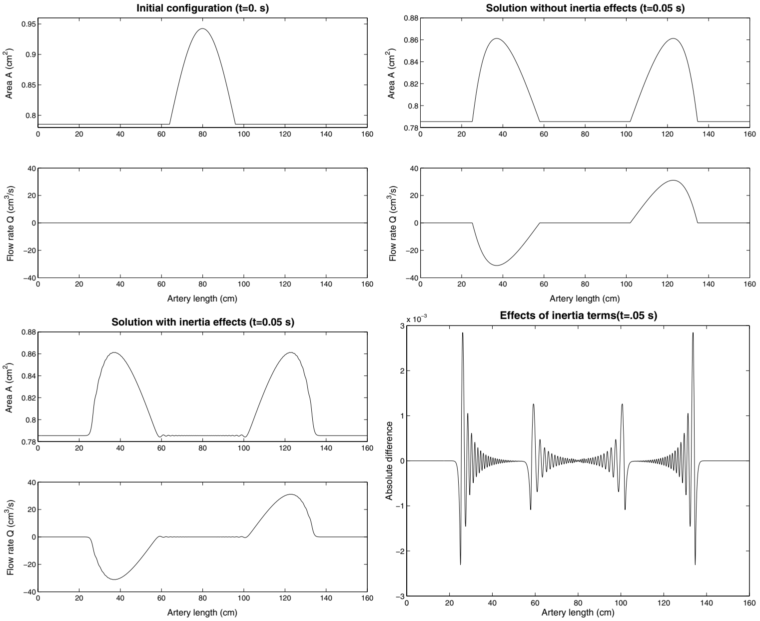

Figure 3.1: Inertia effects on the solution; on the top-left the initial configuration, a half sine wave of length 35 *cm*, is reported. The solutions without inertia term (top-right), with inertia term (bottom-left) and the difference between the two (bottom-right) for a fixed time (0.05 *s*) are reported too.

find $\widetilde{Q}_h \in V_h^0$ such that

$$\left(\frac{1}{A_h^{n+1}}\widetilde{Q}_h^{n+1}, \psi_h\right) + \frac{m}{\rho}\left(\frac{\partial \widetilde{Q}_h^{n+1}}{\partial z}, \frac{\partial \psi_h}{\partial z}\right) = \frac{m}{\rho}\left(\frac{\partial \widehat{Q}_h^{n+1}}{\partial z}, \frac{\partial \psi_h}{\partial z}\right), \quad \forall \psi_h \in V_h^0. \qquad (3.1.8)$$

This corresponds to having imposed a homogeneous Dirichlet boundary condition for the correction term $\widetilde{Q}$.
An alternative approach could be to linearize the coefficient in equation $(3.1.7)_3$ and to modify the mass matrix in the Lax-Wendroff finite element solver adding a stiffness matrix multiplied by $\frac{mA_0}{\rho}$ (see [9]).
In the following numerical experiments we have set $\rho = 1\ gr/cm^3$, ν =0.035 m^2/s, R_0 has been taken to be constant and equal to 0.5 cm, h_0 =0.05 cm and $E = 3\ 10^6\ dyne/cm^2$. The simulations have been carried out using a time step $\Delta t = 10^{-5}\ s$.
Figure 3.1 shows the results for a realistic test problem where the vessel wall density is set to $\rho_w = 1gr/cm^3$ and we take a wave of length 32 cm (top-left of Figure 3.1). It should be noted that the inertia term yields a relative variation in the vessel area of the order of 10^{-3}.

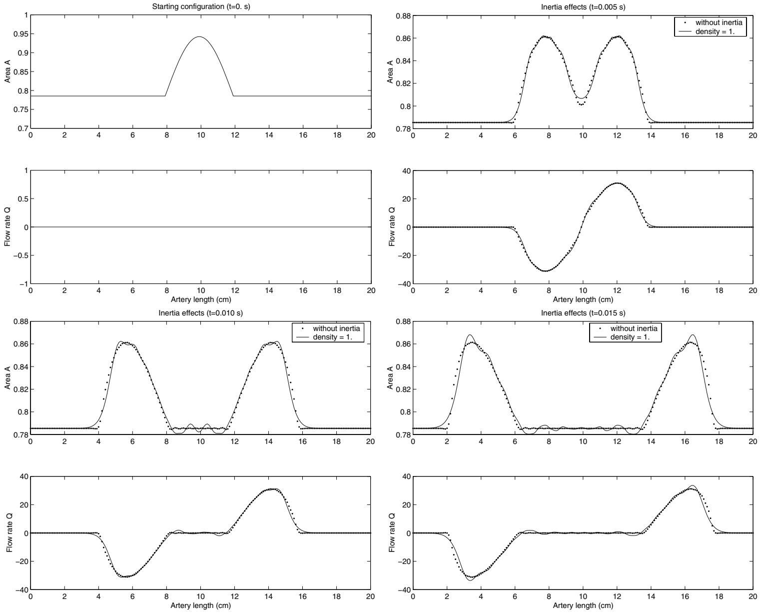

Figure 3.2: Inertia effects on the solution; on the top-left the initial configuration, a half sine wave of length 4 cm, is reported. The solutions without inertia term (dotted line) and with inertia term, wall density set to 1 gr/cm^3, (solid line) for different time steps are also reported.

We may also note the high frequency oscillations induced by the inertia term. Clearly, in real conditions these oscillations are damped out by the viscoelastic term. If we use higher frequency (yet less realistic) waves, the variation in the flow rate is more important. We also report numerical experiments carried out in the same geometrical configuration using a pressure wave pulse of length 4 cm (top-left of Figures 3.2 and 3.3) and a wall density of 1 and 100 gr/cm^3, respectively. These tests have been carried out to enhance the inertia effects. Note, in particular, that the value 100 gr/cm^3 is unrealistic under physiological conditions. These tests show that the inertia term plays a major role when the mass or the vessel acceleration are important.

A qualitative comparison with the results obtained by a three dimensional axi-symmetric fluid-structure interaction code (see for instance [22] for a complete description of models and numerical methods) has been carried out only for the test case of Figure 3.2; a good agreement has been found. The difference between the average pressures computed by the two methods is always below 10%.

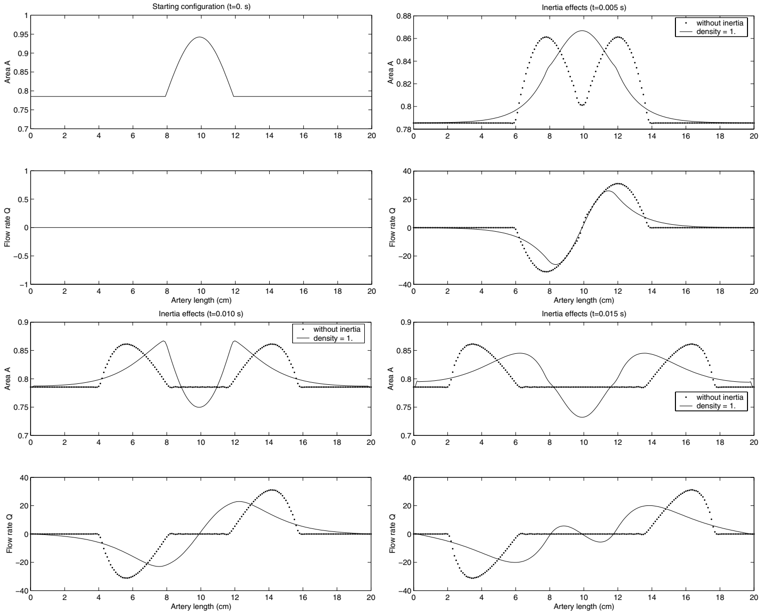

Figure 3.3: Inertia effects on the solution; on the top-left the initial configuration is reported: a half sine wave of length 4 cm. The solutions without inertia term (dotted line) and with inertia term, wall density set to 100 gr/cm^3, (solid line) for different time steps are also reported.

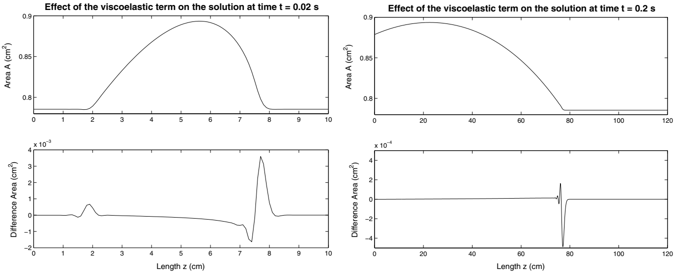

Figure 3.4: Viscoelasticity effects on the solution at two given time steps: solution of the problem without viscoelasticity term (top) and difference between the solutions with and without viscoelastic term (bottom).

3.1.2 Viscoelastic term

In the generalised string model we might account for two possible viscous effects. Here, we have considered only the term in the form $\tilde{\gamma}\frac{\partial \eta}{\partial t}$ (resulting from a simple De Voigt viscoelasticity model, see [35]), since the term $\tilde{c}\frac{\partial^3 \eta}{\partial t \partial z^2}$ will produce a fourth order spatial derivative in the momentum equation that makes its numerical treatment more difficult.

After introducing the term in the momentum equation and using the continuity equation, the modified system reads

$$\begin{cases} \dfrac{\partial A}{\partial t} + \dfrac{\partial Q}{\partial z} = 0 \\ \dfrac{\partial Q}{\partial t} + \dfrac{\partial F_2(A,Q)}{\partial z} - \dfrac{A\gamma}{\rho}\dfrac{\partial^2 Q}{\partial z^2} = B_2(A,Q). \end{cases} \tag{3.1.9}$$

This system has been solved by an operator splitting procedure similar to that introduced before and an implicit Euler discretisation for the correction term $\widetilde{Q}$.

Tests have been carried out to investigate the effects of the viscoelastic term. We set $\rho = 1$ gr/cm^3, ν =0.035 m^2/s, $R_0 = 0.5$ cm, h_0 =0.05 cm and $E = 3$ 10^6 $dyne/cm^2$. The simulations have been carried out with a time step $\Delta t = 10^{-4}$ s and a space discretization $\Delta x = 0.1$ cm. In Figure 3.4 we report the results of a short half sine pressure wave (period 0.015 s, amplitude 20000 $dyne/cm^2$) and a longer one (period 0.3 s, amplitude 20000 $dyne/cm^2$) imposed at inlet. For the viscoelastic computation we have taken $\gamma = 3$ $gr/cm^3 s$. It should be noted that the solutions with and without the viscoelastic term have a relative difference in the area of less than 1 %.

3.1.3 Longitudinal elasticity term

Experimental findings show that vessel walls are longitudinally pre-stressed [35, Chapter 8]. This originates the second z derivative term in the generalised string model [77]. Accounting for this term by using the techniques previously illustrated would produce a modified system of the type

$$\begin{cases} \dfrac{\partial A}{\partial t} + \dfrac{\partial Q}{\partial z} = 0 \\ \dfrac{\partial Q}{\partial t} + \dfrac{\partial F_2(A,Q)}{\partial z} - \dfrac{Aa}{\rho}\dfrac{\partial^3}{\partial z^3}\left(\sqrt{A} - \sqrt{A_0}\right) = B_2(A,Q). \end{cases} \tag{3.1.10}$$

Solving this system by an operator splitting technique like the one presented in Section 3.1.1 would require the solution of a differential equation for the correction term $\widetilde{Q}$ which satisfies

$$\frac{\partial \widetilde{Q}}{\partial t} - \frac{Aa}{\rho}\frac{\partial^3}{\partial z^3}\left(\sqrt{A} - \sqrt{A_0}\right) = 0. \tag{3.1.11}$$

The correction $\widetilde{Q}_h^{n+1} \in V_h^0$ has been computed by a collocation procedure and using a finite difference approximation for the third derivative term of A_h^{n+1} (which is computed in the first step of the operator splitting procedure).

The effect of the longitudinal pre-stress is more important when strong area gradients are present, such as the ones that might be caused by the presence of a stent. To analyse this situation, we consider a stented artery of total length $L = 15\ cm$ with a stent of length 5 cm placed in the middle. The vessel has a radius $R_0 = 0.5\ cm$ and $h_0 = 0.05\ cm$. The Young modulus is $E = 3\ 10^6\ dyne/cm^2$ for the healthy portion of the artery and $E_s = 30\ 10^6\ dyne/cm^2$ for the stented part. At $z = 5\ cm$ and $z = 10\ cm$ (the interfaces between the stent and the healthy artery) the Young modulus has been regularised by a fifth-order function (as done in [32]); the length of the variation zone is 0.1 cm. The coefficient $\tilde{a}$ is set to $10^4\ gr/s^2$. Finally, we take $\rho = 1\ gr/cm^3$, $\nu = 0.035\ cm^2/s$ and $\alpha = 1$.

At inlet we impose a half sine pressure wave of period $T = 0.4\ s$ and amplitude of 20000 $dyne/cm^2$.

Figure 3.5 shows that, without the longitudinal elasticity term (solution represented by a solid line), there is an abrupt variation in the area. Clearly this solution is not physiological as we cannot have, in the limit, a discontinuous area. Taking into account the effect of the longitudinal elasticity term, the variation is smoothed out, although the jump between the values of the area on the left and the right is still of the same magnitude.

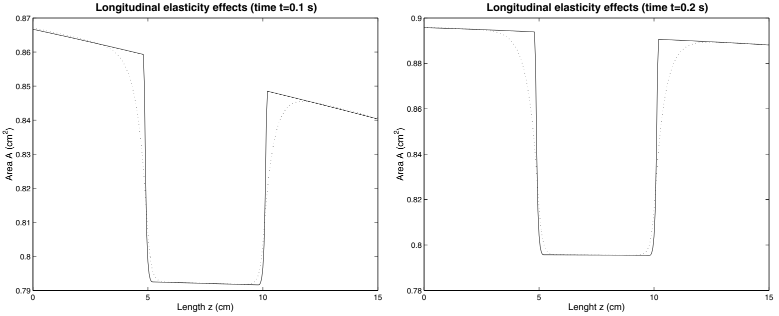

Figure 3.5: Longitudinal elasticity effects on the solution at two different time steps (the solid and the dotted lines represent the solution without and with the longitudinal pre-stress term, respectively). The solid line shows an abrupt variation in the area, which is smoothed out by the longitudinal pre-stress term.

Chapter 4

More complex geometries

Introduction

In this Chapter we will present two generalisations of the model described in Chapter 1: abrupt changes in vessel properties and bifurcating channels.

In some pathological situations, a segment of an artery has either to be replaced by a prosthesis or reinforced by the application of a stent (a metallic wire mesh). In both cases we face a situation where the elastic properties of the vessel change abruptly. The 'stent' problem has attracted the interest of many researchers because of its practical interest and the consequent impact on the marketplace (e.g. [55, 2, 1]). The problem of an abrupt variation on the vessel properties presents some mathematical challenges for 1D models. Clearly it may be treated by regularising the transition region between the healthy artery and the prosthesis, as done in [32].

Here we investigate an alternative approach based on the domain decomposition (DD) method [81]. The set of interface conditions which might be imposed at the interface is not unique [29, 14]. We will present several alternatives, justified by physical arguments, and we will show how, for a particular choice, it is possible to obtain an energy inequality for the coupled system.

From the other side the human arterial system is formed by a network of vessels: even if we approximate each arterial segment by using a one-dimensional description, we need to find a proper way to account for branching. Yet, when accounting for bifurcated channels, we deal with the problem of discontinuous vessel properties: in fact a bifurcation can be viewed as three arteries plus interface conditions and at interfaces the area A is discontinuous.

Again, a DD technique has been developed to treat this situation.

The problem of endovascular treatment of abdominal aortic aneurysm will be addressed as well.

The results reported in this Chapter have been published in the papers [29] and [67].

Figure 4.1: Endograft

4.1 Domain decomposition approach for prostheses and bifurcations

When a stent or a prosthesis such as the one depicted in Figure 4.1 is implanted to alleviate severe vascular pathologies, it causes an abrupt variation of the elastic properties along the artery. In principle this could be taken into account by allowing β to have a discontinuity at the interfaces between the "healthy" and the prosthetic artery, while being a smooth function otherwise. Here we will first consider the case of a single discontinuity at $z = \Gamma \in (0, L)$. By following the arguments in [14] we may derive that in this situation A (and consequently p) is (in general) discontinuous at $z = \Gamma$ and, consequently, the product $A\frac{\partial p}{\partial z}$ in equation (1.1.3) is not well defined at this location.

A possibility to overcome this problem is to use a regularisation for β, as done in [32]. However, this requires the use of a fine mesh around Γ to properly represent the transition, with a consequent loss of efficiency of the numerical scheme because of the stability condition (2.1.7). Furthermore, if the solution is very steep, the Taylor-Galerkin scheme should be stabilised to avoid spurious oscillations, with the inevitable addition of extra numerical dissipation [37].

We will here investigate instead an alternative solution provided by the domain decomposition approach (see [81]). In Figure 4.2 we show the vessel Ω partitioned into two subdomains $\Omega_1 = (0, \Gamma)$ and $\Omega_2 = (\Gamma, L)$. For a standard system in conservation form, the interface condition would entail the continuity of the fluxes, which corresponds to the Rankine-Hugoniot condition for a discontinuity that does not propagate (see e.g.[36]). Unfortunately, in view of the previous considerations, it is arguable whether the interface conditions can be derived from the equations in form (1.1.11) since they have been obtained under the requirement that the solution be smooth. Clearly, the problem concerns only the momentum equation as the continuity equation is originally in conservation form and, by standard arguments, this yields mass flux continuity across the interface (a fact that agrees with the physical intuition):

$$[Q] = Q|_{\Gamma^+} - Q|_{\Gamma^-} = 0. \tag{4.1.1}$$

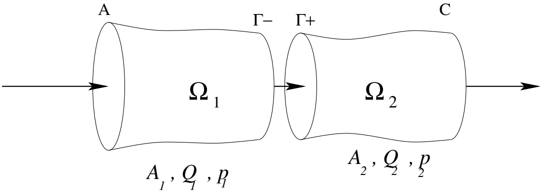

Figure 4.2: Domain decomposition of an artery featuring a discontinuous Young's modulus

The jump condition for the momentum equation has to be driven instead by other considerations. A possibility, investigated in [14], is to consider the limit of a regularised problem. Yet, this procedure is not completely satisfactory, since the limit will in general depend on the way the regularisation procedure is carried out. Another possibility often encountered in the literature for similar situations [63] is to impose the continuity of pressure. Yet, this condition would imply a possible increase of the energy of the system through the discontinuity, a condition hardly justifiable by physical means. Here we have followed the route of searching for a condition which would guarantee an energy inequality for the coupled problem.
In Lemma 2.1 of [28] it has been shown that our problem, in the case of $\alpha = 1$, satisfies the following energy inequality

$$\varepsilon(t) + K_R \int_0^t \int_0^L \bar{u}^2 dz dt + \int_0^t [Q p_t]_0^L \, dt \le \varepsilon(0) \tag{4.1.2}$$

where

$$\varepsilon(t) = \int_0^L \left(\frac{1}{2} A(z,t) \bar{u}^2(z,t) + \frac{1}{\rho} \int_{A_0}^{A(z,t)} \psi(\zeta) d\zeta \right) dz,$$

while $p_t = p + \frac{1}{2}\bar{u}^2$ is the total pressure and $[f]_0^L = f(L) - f(0)$.
In the domain decomposition case of Figure 4.2, indicating quantities in Ω_i with the subscript $i = 1, 2$, we obtain, by summing inequality (4.1.2) applied to the problem in each subdomain,

$$\varepsilon_1(t) + K_R \int_0^t \int_0^\Gamma \bar{u}_1^2 dz dt + \varepsilon_2(t) + K_R \int_0^t \int_\Gamma^L \bar{u}_2^2 dz dt + \int_0^t (Q_2 p_{t,2}|_L - Q_1 p_{t,1}|_0) dt + \int_0^t (Q_1 p_{t,1} - Q_2 p_{t,2})|_\Gamma dt \le \varepsilon_1(0) + \varepsilon_2(0), \quad t > 0. \tag{4.1.3}$$

Should we require that

$$Q_1 p_{t,1} \ge Q_2 p_{t,2} \tag{4.1.4}$$

at the interface point Γ we would obtain an energy inequality equivalent to that of the single domain case. Then, by imposing suitable restrictions on the boundary data following the same arguments given in [28], we obtain a global energy estimate in the form

$$\varepsilon_1(t) + \varepsilon_2(t) + K_R \left[\int_0^t \left(\int_0^\Gamma \bar{u}_1^2 dz + \int_\Gamma^L \bar{u}_2^2 dz \right) dt \right] \le \varepsilon_1(0) + \varepsilon_2(0) + \xi(t) \tag{4.1.5}$$

where ξ is a quantity which depends only on the boundary data and on t. Thanks to (4.1.1) condition (4.1.4) is in particular satisfied by the choice $p_{t,1} = p_{t,2}$; in view of this results we have chosen the following interface conditions

$$\begin{matrix} Q_1 = Q_2 \\ p_{t,1} = p_{t,2} \end{matrix} \quad \text{on } z = \Gamma, \quad t > 0. \tag{4.1.6}$$

Therefore the coupled problem reads, in each domain Ω_i, $i = 1, 2$ and for $t > 0$,

$$\begin{cases} \dfrac{\partial A_i}{\partial t} + \dfrac{\partial Q_i}{\partial z} = 0, \\ \dfrac{\partial Q_i}{\partial t} + \dfrac{\partial}{\partial z}\left(\dfrac{Q_i^2}{A_i}\right) + A_i \dfrac{\partial p_i}{\partial z} + K_R \dfrac{Q_i}{A_i} = 0, \end{cases} \tag{4.1.7}$$

together with the interface condition (4.1.6) and appropriate boundary conditions at $z = 0$ and $z = L$.

To solve the problems in Ω_1 and Ω_2 separately, we have devised a decoupling technique which, at each time step from t^n to t^{n+1}, provides the Taylor-Galerkin algorithm with the values Q_i^{n+1} and A_i^{n+1} of the unknowns at the interface Γ, for $i = 1, 2$. We need to use (4.1.6) together with the compatibility conditions, for instance in the form of the extrapolation of the characteristic variables exiting Ω_1 and Ω_2 at Γ (here, for the sake of simplicity, we will neglect the source term: see Section 2.2 for more details). We indicate with $W_{1,1}^{n+1}$ and $W_{2,2}^{n+1}$ the values at $z = \Gamma$ and $t = t^{n+1}$ of the (outgoing) characteristic variables W_1 and W_2, relative to domain Ω_1 and Ω_2, respectively, obtained by extrapolation from the data at $t = t^n$. Using relation (1.2.9) we finally obtain at $z = \Gamma$ a non linear system for the interface variable, namely

$$\begin{cases} Q_1^{n+1} - Q_2^{n+1} = 0 \\ \psi(A_1^{n+1}; A_{0,1}, \beta_1) + \dfrac{\rho}{2}\left(\dfrac{Q_1^{n+1}}{A_1^{n+1}}\right)^2 - \psi(A_2^{n+1}; A_{0,2}, \beta_2) - \dfrac{\rho}{2}\left(\dfrac{Q_2^{n+1}}{A_2^{n+1}}\right)^2 = 0 \\ \dfrac{Q_1^{n+1}}{A_1^{n+1}} + 4\sqrt{\dfrac{\beta_1}{2\rho A_{0,1}}}\left(A_1^{n+1}\right)^{\frac{1}{4}} - W_{1,1}^{n+1} = 0 \\ \dfrac{Q_2^{n+1}}{A_2^{n+1}} - 4\sqrt{\dfrac{\beta_2}{2\rho A_{0,2}}}\left(A_2^{n+1}\right)^{\frac{1}{4}} - W_{2,2}^{n+1} = 0 \end{cases} \tag{4.1.8}$$

which is solved by a Newton iteration. Here, β_i and $A_{0,i}$ indicate the values of β and A_0 in Ω_i and, for the sake of generality, we have assumed that the reference section area A_0 might be discontinuous at $z = \Gamma$.

It has been verified that the determinant of the Jacobian of system (4.1.8) is different from zero for all allowable values of the parameters, thus guaranteeing that the Newton iteration is well-posed. It has also been found that, by using as starting values the unknowns at time t^n, the method converges in few iterations with a tolerance of 10^{-8} on the relative increment. For values of pressure and velocities typical of blood flow the value of pressure is much greater than the kinetic energy $\frac{1}{2}\bar{u}^2$. This explains why many practitioners in the field use continuity of pressure (instead of total pressure) at the interface without encountering stability problems. This is also true for the interface condition proposed in [14], which does not satisfy the energy inequality (4.1.5) a-priori. Indeed, we have performed some numerical studies and found that,

for conditions akin to the physiological ones, the results obtained by imposing continuity of pressure, continuity of total pressure or the condition reported in [14] differ less than one percent and do not affect stability. In Figure 4.3 we report a numerical comparison between the three conditions: in this case a relative difference of 10^{-5} was found.
A physical argument suggests that the total pressure decreases along the flow direction at Γ, as a function of the flow rate. To account for this, one could impose a relation of the type

$$p_{t,2} = p_{t,1} - \text{sign}(Q) f(Q), \quad \text{at } z = \Gamma,\ t > 0$$

being f a positive monotone function satisfying $f(0) = 0$. Clearly this condition, coupled with the continuity of Q, satisfies (4.1.6). However, the difficulties of finding an appropriate "dissipation function" f for the problem at hand has brought us to consider only the continuity of total pressure, which corresponds to $f \equiv 0$.

4.1.1 Branching

The arterial and venous systems are characterised by the presence of branching. Branching flow is an interesting subject on its own and has recently being studied both theoretically and numerically. We here mention the work in [93] and in [94].
The flow in a bifurcation is intrinsically three dimensional; yet it may still be represented by means of a 1D model, following a domain decomposition approach, if one is not interested in the flow details at the bifurcation. Figure 4.4 shows a model for a bifurcation. In a first stage we simplify the real geometric structure by imposing that the bifurcation is located exactly on one point and neglecting the effect of the bifurcation angles. This approach has been followed also by other authors, like [62]. An alternative technique is reported in [98], where a separate tract containing the branch is introduced.
In order to solve the three problems in Ω_1 (main branch), Ω_2 and Ω_3 we need to find appropriate interface conditions. The hyperbolic nature of the problem tells us that we need three conditions. The first one states the conservation of mass across the bifurcation, i.e.

$$Q_1 = Q_2 + Q_3, \quad \text{at } z = \Gamma, t > 0. \tag{4.1.9}$$

We note that the orientation of the axis in the three branches is such that a positive value of Q_i indicates that blood is flowing from the main branch Ω_1 into the other two. By performing an energy analysis similar to that of the previous section on the three branches separately we reach the conclusion that we can obtain a global energy inequality for the coupled problem whenever $p_{t,1}Q_1 - p_{t,2}Q_2 - p_{t,3}Q_3 \geq 0$. If we impose the continuity of total pressure across the bifurcation together with (4.1.9) we have $p_{t,1}Q_1 - p_{t,2}Q_2 - p_{t,3}Q_3 = 0$. In this situation it is also expected that the complex flow in the bifurcation will cause a decrease in total pressure in the direction of the flow field across the bifurcation, and this loss should be related to the fluid velocity (or flow rate) and to the bifurcation angles.
A possibility to account for this, derived from the analysis of [41], is to impose, at $z = \Gamma$, that

$$\begin{aligned} p_{t,1} - \text{sign}(\bar{u}_1) f_1(\bar{u}_1) &= p_{t,2} + \text{sign}(\bar{u}_2) f_2(\bar{u}_2, \alpha_2), \\ p_{t,1} - \text{sign}(\bar{u}_1) f_1(\bar{u}_1) &= p_{t,3} + \text{sign}(\bar{u}_3) f_3(\bar{u}_3, \alpha_3), \end{aligned} \tag{4.1.10}$$

where α_2 and α_3 are the angles of the branches Ω_2 and Ω_3 with respect to the main one (see Figure 4.5); f_1, f_2 and f_3 are positive functions and equal to zero when the first argument is

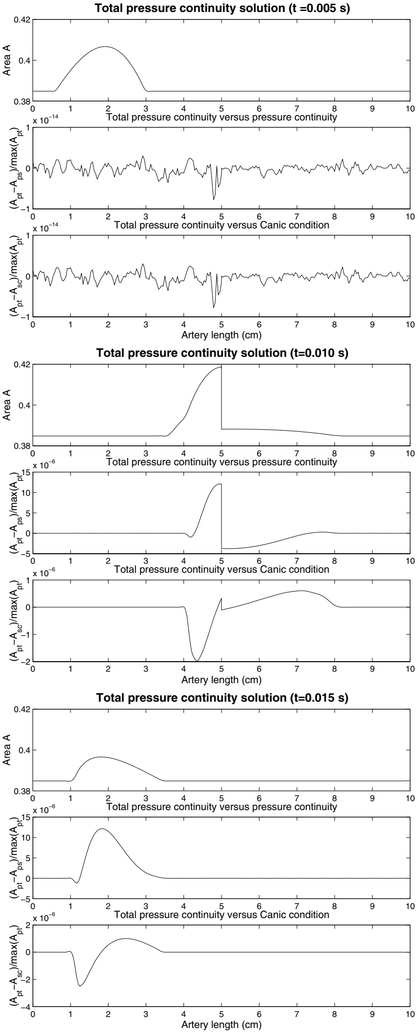

Figure 4.3: Comparison between three different interface conditions for DD. The solution for the condition based on the continuity of the total pressure and the relative differences of the condition based on the continuity of pressure and of the condition reported in [14] are reported for three chosen times.

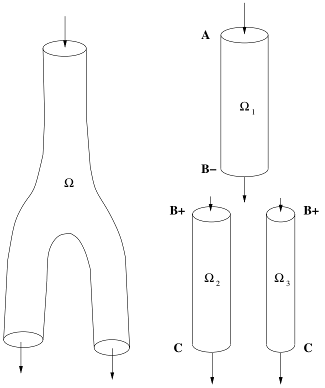

Figure 4.4: One dimensional model of bifurcation by domain decomposition technique

zero. These can be chosen to be:

$$f_1(u) = \gamma_1 u_1^2, \quad f_i(u_i, \alpha_i) = \gamma_i u_i^2 \sqrt{2(1-\cos\alpha_i)},\ i = 2, 3, \tag{4.1.11}$$

where the γ_i are positive coefficients.
In the numerical scheme, (4.1.9) and (4.1.10) will be complemented by three compatibility relations, which can be expressed again by the extrapolation of the outgoing characteristic variables. We have thus a non linear system for the six unknowns A_i^{n+1}, Q_i^{n+1}, $i = 1, 2, 3$, at the interface location Γ, which is solved by a Newton iteration.
Some numerical tests have been made to investigate the effect of the bifurcation angles using relations (4.1.10) and (4.1.11) ($\gamma_1 = 0$, γ_2 and $\gamma_3 = 2$). The length of the three domains has been taken equal to 10 cm. The following parameters have been chosen: E =3 10^6 $dyne/cm^2$, h_0 =0.05 cm, $R_0 = 0.5$ cm, ρ =1 gr/cm^3, $\alpha = 1$, ν =0.035 cm^2/s, equal in all three vessels. At the inlet of Ω_1 we have imposed a half sine input pressure wave of period 0.1 s and amplitude 20000 $dyne/cm^2$, while a non-reflecting condition has been imposed at the outlet sections of Ω_2 and Ω_3. In Figures 4.6, 4.7 and 4.8 we show the time variation of the area A and the two characteristic variables W_1 and W_2 at a location placed at the midpoint of Ω_1, Ω_2 and Ω_3, respectively, for different values of α_1 and α_2. In particular, $\alpha_1 = \alpha_2 = 0$ corresponds to the case where we impose just the continuity of the total pressure, ignoring the dissipative effects caused by the kinks. We may note that using the formula (4.1.10) that accounts for the angles increases the wave reflection upstream of the bifurcation (there is an increase in the amplitude of W_2 in Figure 4.6), with a subsequent increase in the pressure level in Ω_1. On the other hand, the strength of the wave transmitted into Ω_2 and Ω_3 is reduced (as expected). The result of this simple experiment shows that indeed the dissipation caused by the flow deviation at bifurcations could be relevant.
Also in this case, due to the difficulty of finding suitable values of the “dissipation functions” f_i for the problem at hand, we have preferred to put them to zero and impose the continuity

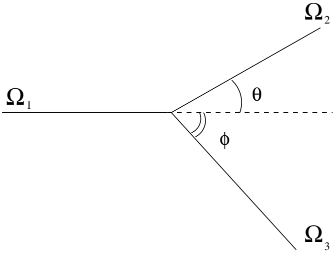

Figure 4.5: A sketch of branching.

of the total pressure across the bifurcation, i.e.,

$$p_{t,1} = p_{t,2} = p_{t,3}, \quad \text{at } z = \Gamma. \tag{4.1.12}$$

Thence, in the remaining part of this work we will neglect this effect.

4.1.2 Bifurcated channel with endograft

Here we show an application of the one dimensional model to a real-life problem. Abdominal aortic aneurysms (AAA) represent a significant and relatively common vascular problem. They are characterised by an abnormal dilatation of a portion of the aorta. This swollen region would enlarge with time and, without a surgical treatment, it will eventually break with fatal consequences. Even if open surgical repair is still the standard treatment for AAA, endografts and endovascular stent grafts begin to play a major role as they allow a less invasive treatment (Figure 4.9).

The presence of an endograft may be treated by our one-dimensional model as a bifurcated channel with varying mechanical properties, as shown in Figure 4.10. The domain is decomposed into 6 regions, Ω_i, $i = 1, \dots, 6$ and the interface conditions of type (4.1.6) or (4.1.9)-(4.1.12) are used where appropriate.

A preliminary numerical test has been carried out by selecting all Ω_i to be of equal length L=5 *cm*. We considered everywhere $\rho = 1\ gr/cm^3$, $\nu = 0.035\ cm^2/s$, $\alpha = 1$, $h_0 = 0.05\ cm$; while the Young's moduli have been taken to be equal to $E_{endograft} = 60\ 10^6\ dyne/cm^2$ for the endografted part (Ω_i, $i = 2, 3, 5$) and $E_{vessel} = 10\ 10^6\ dyne/cm^2$ for the remaining subdomains. The vessel reference radii have been taken to be $R_{0,1} = R_{0,2} = 0.6\ cm$, $R_{0,3} = R_{0,4} = 0.4\ cm$ and $R_{0,5} = R_{0,6} = 0.5\ cm$.

At inlet we have imposed a half sine pressure wave of period 0.1 *s* and amplitude 20000 $dyne/cm^2$.

The spatial grid was uniform with a total of 546 nodes. The computations were carried out with a time step $\Delta t = 0.00001\ s$.

Figures 4.11, 4.12, 4.13 report the time evolution for the area A and the two characteristic variables W_1 and W_2 at three given points, respectively at the middle of Ω_1, and of Ω_2 and of Ω_6. By inspecting Figure 4.11 we remark that in W_1 we find the input wave imposed at inlet, while in W_2 we find the composition of two effects, the wave reflected from the beginning of the endograft and the wave reflected from the branching point. These modify the sinusoidal

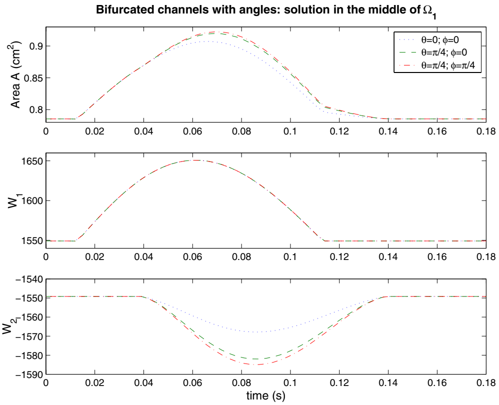

Figure 4.6: Solution dependence on bifurcation angles: area and characteristic variables at the middle point of domain Ω_1 are reported.

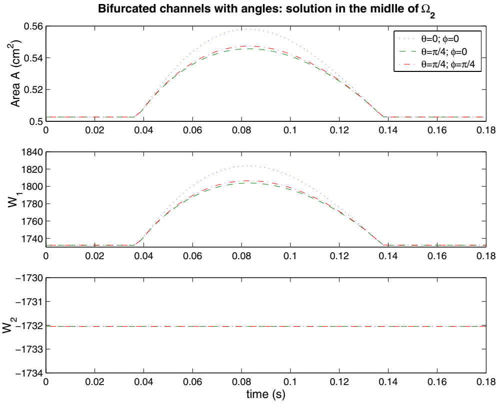

Figure 4.7: Solution dependence on bifurcation angles: area and characteristic variables at the middle point of domain Ω_2 are reported.

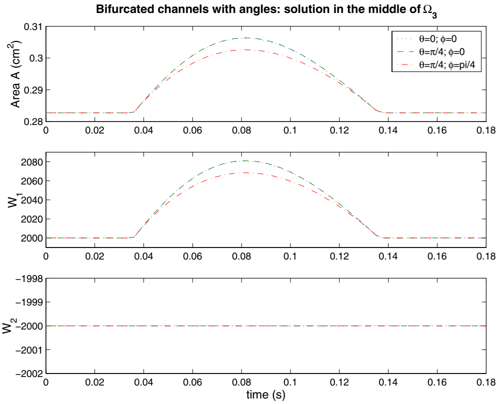

Figure 4.8: Solution dependence on bifurcation angles: area and characteristic variables at the middle point of domain Ω_3 are reported.

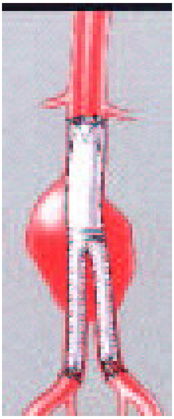

Figure 4.9: Endograft placement in the surgical treatment of abdominal aortic aneurysms.

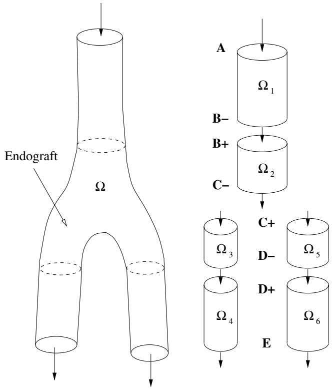

Figure 4.10: Modelling (left) and domain decomposition (right) of a bifurcation with an endograft.

shape of the area A. In Figure 4.12 we find in W_2 only the wave reflected from the branching point. Finally, in Figure 4.13 we do not find reflected waves (being the outlet boundary condition an absorbing one); moreover, in W_1 we can observe the part of the wave passing through the branches.

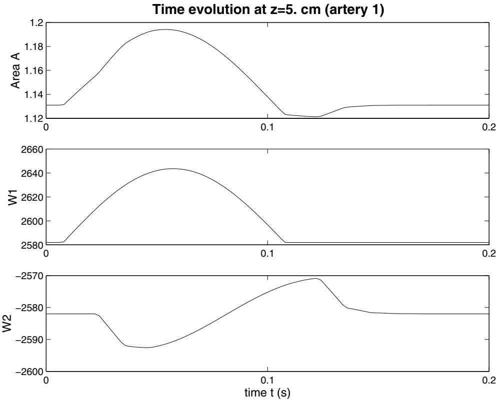

Figure 4.11: Bifurcation with endograft: time evolution for the area and the characteristic variables in the middle of domain Ω_1.

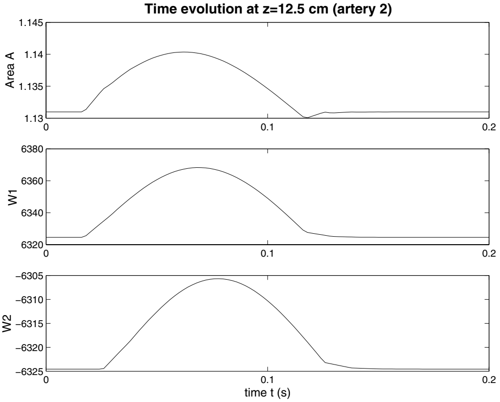

Figure 4.12: Bifurcation with endograft: time evolution for the area and the characteristic variables in the middle of domain Ω_2.

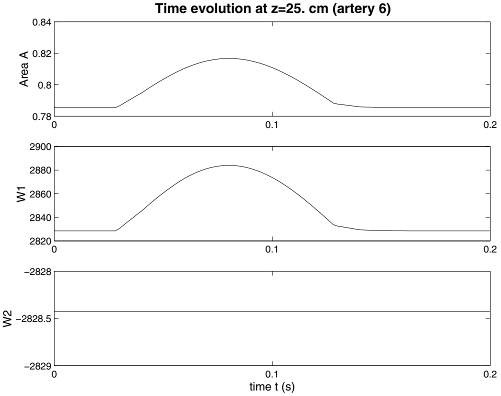

Figure 4.13: Bifurcation with endograft: time evolution for the area and the characteristic variables in the middle of domain Ω_6.

Chapter 5

Curved vessels

In this Chapter we address the problem of flow simulation on curved pipes: how does curvature modify the wave propagation on a simple tube? How can we derive reduced models for curved arteries?

Starting from the theory of *Cosserat* curves [58], Green and Naghdi [38] developed a general framework to study the problem of flow simulation on straight and curved cylindrical pipes. Moreover in [39] they have analyzed the case of a fluid in a curved pipe of constant curvature. The main idea, reported in [39], is, given a generic domain with a (x, y, χ) coordinate system, the development of the fluid velocity on a basis of "shape functions": $\vec{u}(x, y, \chi, t) = \sum_{n=0}^{N} \lambda_n(x, y)\omega_n(\chi, t)$, where $\lambda_n(x, y)$ are the "shape functions" and $\omega_n(\chi, t)$ the coefficients of the velocity profile.

Here we apply this theory to the specific case of haemodynamics modelling.

After choosing a set of shape functions, some models are derived for either straight or curved (with constant curvature) cylindrical pipes, the unknowns of the problem being the coefficients of the velocity profile. The models obtained are a generalization of the classical 1D model and, in the simplest cases, they are hyperbolic.

In principle we can improve the "quality" of these models as much as we want, simply increasing the dimensions of the chosen basis of shape functions; however, as it will be pointed out at the end of this Chapter, numerical difficulties and computational constraints arise in practice since the number of unknows increases and the system becomes of a mixed hyperbolic-parabolic type.

An approach similar to this one has been recently used in [85], in the framework of rigid and straight cylinder configurations, to obtain an alternative formulation to the classical 1D models.

In contrast with what done therein and in [38], but in analogy with the classical 1D models presented in Chapter 1, we don't impose exactly the divergence constraint.

Some preliminary numerical results for curved geometries and a comparison with the straight case are also reported.

The models presented in this Chapter have been developed in collaboration with L. Formaggia.

5.1 Some preliminary considerations

In Chapter 1 we have seen that, by considering a straight cylindrical domain Ω_t, reduced models are obtained starting from the Navier-Stokes equations by integration over transversal sections. The reduced model was derived neglecting the components of the velocity field in the (x, y) plane and after prescribing a given profile for the z component of the velocity (i.e. $u_z = s(x, y)\bar{u}(z, t)$, $s(x, y)$, being $\bar{u}(z, t)$ the mean velocity). This leads to the 2 by 2 system of partial differential equations (1.1.13). In the reduced models here presented we enrich the velocity field: the components of velocity on the plane (x, y) is no longer neglected and the component of velocity along the longitudinal axis is described, on each vessel section, by a higher order polynomial. This allows the development of non-symmetric velocity profiles.
Even if more complex models for the pressure-area relation have been proposed and analyzed [79, 29], in this context we will still consider a constant pressure over each axial section, related to the area by an algebraic wall law.
The main application of this study is modelling the flow field in curved pipes; nevertheless as first step we develop and test the new reduced models on a straight geometry. For instance this could be very useful in a domain decomposition approach where we approximate a part of the computational domain by a straight geometry and another by a curved one.
We report here only about some models developed for straight geometry and the extension of them for curved geometry (with constant curvature). These models are characterized by a weak imposition of the divergence constraint; in this respect they differ from the original model by Naghdi and Green [38, 39]. The physical hypothesis behind their derivation being that the longitudinal component of the velocity is the predominant one.
Other models have been considered as well: in particular the possibility to have a profile for the pressure not constant over the transversal section and the possibility to satisfy the divergence equation exactly [27].

In order to make more clear the derivation of the more complex models in next Sections, the general problem is recalled and the 1D model is again rederived.

5.1.1 Navier-Stokes equations and some definitions

In the following derivations of reduced models it will consider as starting point the Navier-Stokes equations

$$\begin{cases} \dfrac{\partial \mathbf{u}}{\partial t} + \text{div } (\mathbf{u} \otimes \mathbf{u}) + \dfrac{1}{\rho}\nabla P - \nu \Delta \mathbf{u} = 0 \\ \text{div } \mathbf{u} = 0 \end{cases} \quad \text{in } \Omega_t, t > 0 \tag{5.1.1}$$

set on a domain Ω_t which changes in time because of the flow induced wall movement. Here $\mathbf{u} = (u_\chi, u_y, u_z)$ is the fluid velocity, P denotes the pressure, ν is the kinematic viscosity and ρ the blood density; (χ, y, z) is a system of coordinates, either Cartesian or curved.

System (5.1.1) componentwise reads:

$$\frac{\partial u_\chi}{\partial t} + \text{div }(u_\chi \mathbf{u}) + \frac{1}{\rho}\frac{\partial P}{\partial \chi} - \nu \Delta u_\chi = 0 \tag{5.1.2}$$

$$\frac{\partial u_x}{\partial t} + \text{div }(u_x \mathbf{u}) + \frac{1}{\rho}\frac{\partial P}{\partial x} - \nu \Delta u_x = 0 \tag{5.1.3}$$

$$\frac{\partial u_y}{\partial t} + \text{div }(u_y \mathbf{u}) + \frac{1}{\rho}\frac{\partial P}{\partial y} - \nu \Delta u_y = 0 \tag{5.1.4}$$

$$\frac{\partial u_\chi}{\partial \chi} + \frac{\partial u_x}{\partial x} + \frac{\partial u_y}{\partial y} = 0 \tag{5.1.5}$$

We will consider cylindrical domains (χ, x, y), as the ones depicted in Figures 5.1 and 5.8, straight and curved, respectively. When dealing with a generic Riemannian geometry we need to account for the concept of metric tensor. This latter is a tensor of rank 2 (symmetric and positive definite) that is used to measure distances and angles. Once a local basis is chosen, the metric tensor appears as a matrix. The notation $\mathbf{G} = (g_{ij})$ is conventionally used for the metric tensor [7, 18]. In our case we have orthogonal coordinate systems, so $\mathbf{G}$ is diagonal and we use the scale factors $h_i = \sqrt{g_{ii}}$, $i = 1, 2, 3$.

For an Euclidean geometry (Figure 5.1) we have

$$\mathbf{G} = \left\{ \begin{array}{ccc} h_1^2 & 0 & 0 \\ 0 & h_2^2 & 0 \\ 0 & 0 & h_3^2 \end{array} \right\} = \left\{ \begin{array}{ccc} 1 & 0 & 0 \\ 0 & 1 & 0 \\ 0 & 0 & 1 \end{array} \right\} \tag{5.1.6}$$

while for the curved geometry of Figure 5.8 we have

$$\mathbf{G} = \left\{ \begin{array}{ccc} h_1^2 & 0 & 0 \\ 0 & h_2^2 & 0 \\ 0 & 0 & h_3^2 \end{array} \right\} = \left\{ \begin{array}{ccc} 1 & 0 & 0 \\ 0 & 1 & 0 \\ 0 & 0 & \left(\frac{y+C}{C}\right)^2 \end{array} \right\}, \tag{5.1.7}$$

where C is the curvature radius.

In the following we will indicate by $g^{\frac{1}{2}} = h_1 h_2 h_3$ the metric of the space. The metric is the measure of the space in the chosen system of coordinates. For a Cartesian system $g^{\frac{1}{2}} = 1$, while for a curved geometry with constant curvature (as the one represented in Figure 5.8) $g^{\frac{1}{2}} = \frac{y+C}{C}$. Obviously the expressions of the operators present in system (5.1.1) in terms of physical variables will depend on the metric tensor (for general expressions see e.g. [10, 7]). In particular we remark that the following relation holds

$$\lim_{\epsilon \to 0} \frac{1}{\epsilon} \int_{V(\epsilon)} \bullet \quad d\Omega = \lim_{\epsilon \to 0} \frac{1}{\epsilon} \int_{\bar{\chi}-\epsilon}^{\bar{\chi}+\epsilon} \left[\iint_S g^{\frac{1}{2}} \bullet \quad dxdy \right] d\chi = \iint_S g^{\frac{1}{2}} \bullet \quad dxdy.$$

where S is the section of the vessel and V_ϵ is a volume ($V_\epsilon = S \times [\bar{\chi} - \epsilon, \bar{\chi} + \epsilon]$).

Thus we define the following operators:

$$\begin{array}{rcl} \mathbf{P_0}(\bullet) & = & \displaystyle\iint_S g^{\frac{1}{2}} \bullet \quad dxdy \\ \mathbf{P_1}(\bullet) & = & \displaystyle\iint_S g^{\frac{1}{2}} \bullet \quad xdxdy \\ \mathbf{P_2}(\bullet) & = & \displaystyle\iint_S g^{\frac{1}{2}} \bullet \quad ydxdy \end{array}$$

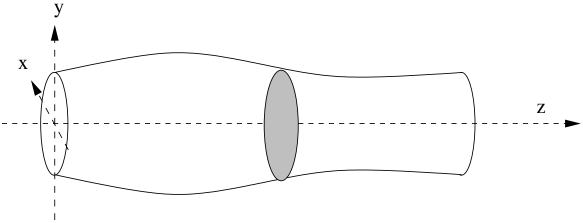

Figure 5.1: The cylindrical domain Ω_t. The cylinder axis is aligned with the coordinate z. The axial sections z =constant remain circular at all times.

The reduced models will be obtained applying these operators to equations (5.1.2-5.1.5).

5.1.2 An alternative derivation of the basic one dimensional model

The domain Ω_t is a straight cylinder (with axis oriented along the coordinate z) and we assume $0 < z < L$, L being the vessel length, taken to be constant with time. We make the assumption of axial symmetry for all the quantities involved. Furthermore a wall displacement along the radial direction is considered. This implies that each axial section S remains circular at all times. The pressure is taken to be constant on each axial section ($p(x, y, z) = p(z)$) and we assume that viscous effects are relevant only near the wall boundary; moreover we assume an algebraic law (1.1.8) for the vessel wall. The component u_z is assumed to be dominant with respect to u_x and u_y and furthermore that it may be described as

$$u_z(x, y, z, t) = \overline{u}(z, t) s\left(\frac{x}{R(z, t)}, \frac{y}{R(z, t)}\right),$$

where $\overline{u}(z, t)$ is the average velocity on each axial section, s is a velocity profile and $R(z, t)$ is the vessel radius (in the following we will write R instead of $R(z, t)$). The profile is chosen to be a parabolic one (Poiseuille solution). Thence:

$$u_z(x, y, z, t) = \left(1 - \frac{x^2 + y^2}{R^2}\right) a(z, t) = 2\left(1 - \frac{x^2 + y^2}{R^2}\right) \overline{u}(z, t)$$

By applying the operator $\mathbf{P_0}$ to equations (5.1.2) and (5.1.5), one finally obtains, by straightforward calculations, the following system

$$\frac{\partial A}{\partial t} + \frac{\partial Q}{\partial z} = 0 \qquad (5.1.8)$$

$$\frac{\partial Q}{\partial t} + \frac{4}{3}\frac{\partial}{\partial z}\left(\frac{Q^2}{A}\right) + \frac{\beta}{2\rho A_0} A^{\frac{1}{2}} \frac{\partial A}{\partial z} + 8\pi\nu\frac{Q}{A} = 0 \qquad (5.1.9)$$

for all $z \in (0, L)$ where the unknowns A and Q denote the section area and the flow rate, respectively.

Note that we have obtained the same system that was derived in Chapter 1 under the assumption of a parabolic profile for the longitudinal component of the velocity field.

5.2 Straight geometry: first simplified model

A better model is obtained by enriching the description of the velocity profile. For the main component of the velocity field, u_z, we consider the following expansion:

$$u_z = \left(1 - \frac{x^2+y^2}{R^2}\right)\left(a(z,t) + b(z,t)x + c(z,t)y\right). \tag{5.2.1}$$

$a(z,t), b(z,t), c(z,t)$ are the coefficients of the velocity profile and they are unknowns.
Note that we could consider this expansion as a perturbation of the Poiseuille parabolic profile.
For the other two components of the velocity field we consider an expansion over the same basis:

$$u_x = o_{x1}(z,t) + o_{x2}(z,t)x + o_{x3}(z,t)y \tag{5.2.2}$$

$$u_y = o_{y1}(z,t) + o_{y2}(z,t)x + o_{y3}(z,t)y \tag{5.2.3}$$

where o_{xi} and o_{yi} $(i = 1,2,3)$ are the coefficients of the velocity profiles to be computed.
A simpler model is obtained by completely neglecting the u_x and u_y velocity components in equation (5.1.2): this is reported later in Section 5.2.2.

Because of the cylindrical simmetry of the problem we know that the displacement is radial; therefore the section remains circular and, for each of its points, $(x = R\cos\theta, y = R\sin\theta)$, with $\theta \in [0, 2\pi]$, we can impose

$$u_x|_{(R\cos\theta,R\sin\theta)} = o_{x1}(z,t) + o_{x2}(z,t)R\cos\theta + o_{x3}(z,t)R\sin\theta = \dot\eta\cos\theta$$

$$u_y|_{(R\cos\theta,R\sin\theta)} = o_{y1}(z,t) + o_{y2}(z,t)R\cos\theta + o_{y3}(z,t)R\sin\theta = \dot\eta\sin\theta.$$

where $\dot\eta = \frac{\partial\eta}{\partial t}$ is the velocity of the vessel wall.
Finally, by straightforward calculation

$$o_{x1} = o_{y1} = o_{x3} = o_{y2} = 0 \ , \ o_{x2} = \frac{\dot\eta}{R} \text{ and } o_{y3} = \frac{\dot\eta}{R}$$

Substituting into equations (5.2.2) and (5.2.3) we obtain the expressions for u_x and u_y:

$$u_x = \frac{\dot\eta}{R}x \qquad u_y = \frac{\dot\eta}{R}y, \tag{5.2.4}$$

which state that the x and y components of the velocity field have a linear variation.

The unknowns of the problem considered are the area A and the three coefficients of the axial velocity expansion a, b, c. Clearly we need 4 equations to close the system; they are obtained by applying $\mathbf{P_0}$ to equation (5.1.5), and $\mathbf{P_0}$,$\mathbf{P_1}$,$\mathbf{P_2}$ to equation (5.1.2), because of the constant expansion for the pressure profile and the linear expansion for the u_z velocity components.
Remark that in this way the Navier-Stokes divergence equation is imposed only *weakly*, that is, in an integral form. Thus the velocity field we obtain does not fulfill the divergence equation pointwise.
In order to ameliorate the readeability of the final system and compare it to the one dimensional model of Section 5.1.2 we define the following variables: $Q = \frac{\pi}{2}a(z,t)R^2$, $H =$

$\frac{\pi}{12}b(z,t)R^4$, $G = \frac{\pi}{12}c(z,t)R^4$. Note that Q is, in fact, the flow rate.
We get

$$\left\{\begin{array}{l} \dfrac{\partial A}{\partial t} + \dfrac{\partial Q}{\partial z} = 0 \\ \dfrac{\partial Q}{\partial t} + \dfrac{4}{3}\dfrac{\partial}{\partial z}\dfrac{Q^2}{A} + 6\pi\dfrac{\partial}{\partial z}\dfrac{H^2}{A^2} + 6\pi\dfrac{\partial}{\partial z}\dfrac{G^2}{A^2} + \dfrac{\beta}{3\rho A_0}\dfrac{\partial}{\partial z}A^{\frac{3}{2}} = -8\pi\nu\dfrac{Q}{A} \\ \dfrac{\partial H}{\partial t} + \dfrac{1}{2}\dfrac{H}{A}\dfrac{\partial Q}{\partial z} + 2\dfrac{\partial}{\partial z}\dfrac{HQ}{A} = -24\pi\nu\dfrac{H}{A} \\ \dfrac{\partial G}{\partial t} + \dfrac{1}{2}\dfrac{G}{A}\dfrac{\partial Q}{\partial z} + 2\dfrac{\partial}{\partial z}\dfrac{GQ}{A} = -24\pi\nu\dfrac{G}{A} \end{array}\right. \tag{5.2.5}$$

The first equation of system (5.2.5), which states the mass conservation, is the same that in the basic model. The second equation differs for the presence of two terms which depend on the asimmetries of the u_z velocity profile, while the other two equations describe the evolution of the non-simmetric profiles. It appears also that, if in the initial configuration H and G are zero and the boundary conditions are compatible with $H = G = 0$, they will remain zero everywhere for all time $t > 0$. The system, in this case, reduces to the one dimensional model described by eqs. (5.1.8) and (5.1.9). This is what we expected because of the axial simmetry of the problem studied.
System (5.2.5) is rewritten in quasi-linear form as

$$\frac{\partial \mathbf{U}}{\partial t} + \mathbf{J}\frac{\partial \mathbf{U}}{\partial z} = \mathbf{B}(\mathbf{U}) \tag{5.2.6}$$

where $\mathbf{U} = [A, Q, H, G]^T$ and

$$\mathbf{J} = \begin{bmatrix} 0 & 1 & 0 & 0 \\ -\dfrac{4}{3}\dfrac{Q^2}{A^2} - 12\pi\dfrac{H^2}{A^3} - 12\pi\dfrac{G^2}{A^3} + \dfrac{\beta}{2\rho A_0}\sqrt{A} & \dfrac{8}{3}\dfrac{Q}{A} & 12\pi\dfrac{H}{A^2} & 12\pi\dfrac{G}{A^2} \\ -2\dfrac{HQ}{A^2} & \dfrac{5}{2}\dfrac{H}{A} & 2\dfrac{Q}{A} & 0 \\ -2\dfrac{GQ}{A^2} & \dfrac{5}{2}\dfrac{G}{A} & 0 & 2\dfrac{Q}{A} \end{bmatrix} \tag{5.2.7}$$

$$\mathbf{B} = \begin{bmatrix} 0 \\ -8\pi\nu\dfrac{Q}{A} \\ -24\pi\nu\dfrac{H}{A} \\ -24\pi\nu\dfrac{G}{A} \end{bmatrix}. \tag{5.2.8}$$

We have already remarked that system (5.2.5) reduces to system (1.1.13) when $H = G = 0$; therefore the characteristic analysis we did in Section 1.2.1 is still valid. Also, if we consider

the linearization of the matrix $\mathbf{J}$ around the state $H = G = 0$ we find the following eigenvalues: $\lambda_{1,2} = \frac{1}{A}\{\frac{4}{3}Q \pm \frac{1}{3}\sqrt{4Q^2 + 9\frac{\beta}{2\rho A_0}A^{\frac{5}{2}}}\}$, $\lambda_3 = \lambda_4 = 2\frac{Q}{A}$. As $4Q^2 + 9\frac{\beta}{2\rho A_0}A^{\frac{5}{2}}$ is always positive, λ_1 and λ_2 are real, $\lambda_1 \neq \lambda_2$ and for physiological flow conditions $\lambda_2 < 0 < \lambda_1$. Thence system (5.2.5) linearized around this state is still hyperbolic.
Moreover we can verify that the two linearizations of $\mathbf{J}$ around the points $(Q = 0, H = 0)$ and $(Q = 0, G = 0)$ yield a hyperbolic system. We consider just the linearization around the state $(Q = 0, H = 0)$, the system being symmetric in the variables H and G. In this case the 4 eigenvalues are $\lambda_{1,2} = \pm\frac{1}{A^2}\sqrt{A\left(18\pi H^2 + \frac{\beta}{2\rho A_0}A^{\frac{7}{2}}\right)}$, $\lambda_3 = \lambda_4 = 0$. Yet, as the value $A\left(18\pi H^2 + \frac{\beta}{2\rho A_0}A^{\frac{7}{2}}\right)$ is positive, the 4 eigenvalues are real and λ_1 and λ_2 have always different signs.

System (5.2.6) is solved by a finite difference upwind scheme

$$\mathbf{U}_j^{n+1} = \mathbf{U}_j^n - \frac{\Delta t}{\Delta z}\mathbf{A}^+\left(\mathbf{U}_j^n - \mathbf{U}_{j-1}^n\right) - \frac{\Delta t}{\Delta z}\mathbf{A}^-\left(\mathbf{U}_{j+1}^n - \mathbf{U}_j^n\right) + \Delta t\mathbf{B}_j^n \qquad j = 1, n_{nodes}\ ,\ t = t^n$$

where $\mathbf{A}^{\pm} = \mathbf{R}\mathbf{\Lambda}^{\pm}\mathbf{R}^{-1}$, $\mathbf{\Lambda}^+ = \mathrm{diag}(\lambda_i^+) = \mathrm{diag}(\max(\lambda_i, 0))$, $\mathbf{\Lambda}^- = \mathrm{diag}(\lambda_i^-) = \mathrm{diag}(\min(\lambda_i, 0))$, λ_i being the eingenvalues of the matrix $\mathbf{J}$ and $\mathbf{R}$ the matrix of right eigenvectors, to be numerically computed after a linearization of the matrix $\mathbf{J}$ ([80, 76]).
This method is stable under the CFL condition $\max_i |\frac{\lambda_i \Delta t}{\Delta x}| < 1$ [76].

Non reflecting boundary conditions are imposed, consistently with the hyperbolic nature of the system, by a pseudo-characteristics method [80]. Considering eq. (5.2.6) we evaluate $\mathbf{J}$ at the time step t^n; then it is possible to numerically compute the eigenvectors and to construct the matrix $\mathbf{L}$, by which we can easily obtain the pseudo-characteristic variables $(\mathbf{W} = \mathbf{L}^n\mathbf{U}^n)$. Thus we can impose at inlet wave traveling on the ingoing characteristic variables (corresponding to positive eigenvalues) and at outlet a constant on the entering characteristic variable (corresponding to a negative eigenvalue).

5.2.1 Numerical results

Figure 5.2 presents possible velocity profiles compatible with the chosen u_z expression. The profile can be non-symmetric and also recirculation along z axis is allowed. In Figure 5.3 the solution of a test case ($\rho = 1\ gr/cm^3$, $A_0 = 1\ cm^2$, $\beta = 10^6\ gr/s^2$, $\nu = 0.035\ cm^2/s$) is presented. For the solution a time step $\Delta t = 0.0001\ s$ and a space discretization $\Delta z = 0.2\ cm$ were used. In the initial configuration (solution at $t = 0\ s$) $A = A_0$ and $G = 0$, while Q and H have an assigned profile (half-sine functions with $Q_{max} = 100\ cm^3/s$ and $H_{max} = 10\ cm^4/s$). As the tube is straight, there is no propagation of the H profile which goes to zero slowly due to the presence of a source term in eq. (5.2.6). To confirm that we set the fluid viscosity to zero; hence, the source term is null. The results for the same test case are reported in Figure 5.4. The H profile doesn't propagate because of the problem symmetry: in fact we expect to have far from the perturbed region a symmetric velocity profile. From eqs. (5.2.5) it can be see that if $Q = 0$ then H doesn't propagate. Moreover we remark that the flow rate Q can be zero even if H or G are different from zero: in fact the "averages" of H and G are null. In Figure 5.5 we report the velocity profile for the same test case (at $t = 0.20\ s$, $z = 40\ cm$) and two projections of the velocity profile along y axes and along x axes, respectively. This Figure shows that the average of the velocity profile is zero.

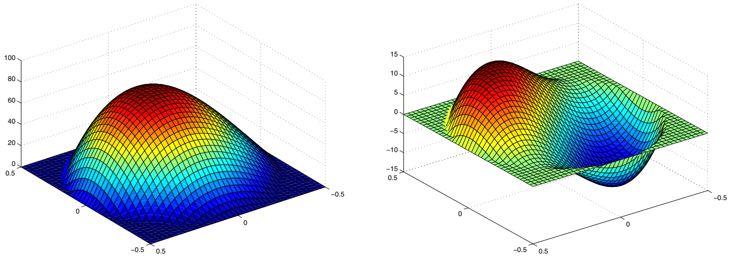

Figure 5.2: Possible velocity profiles for the choosen u_z development: at left for $A = 0.7854$, $Q = 30$, $H = 10$, $G = 10$, at right for $A = 0.7854$, $Q = 0$, $H = 10$,$G = 10$.

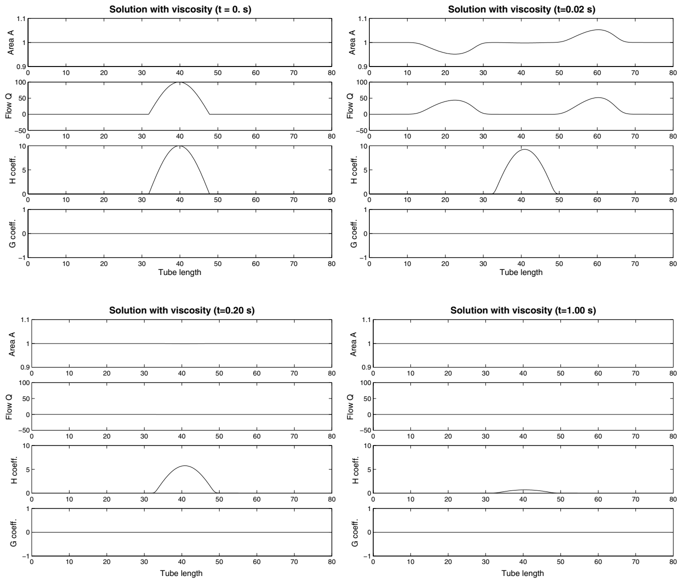

Figure 5.3: Solution at selected time steps for a straight artery of lenght 80 cm. H and G profiles don't propagate; the H profile initialised to a particular value in the starting configuration disappear because of viscosity effects.

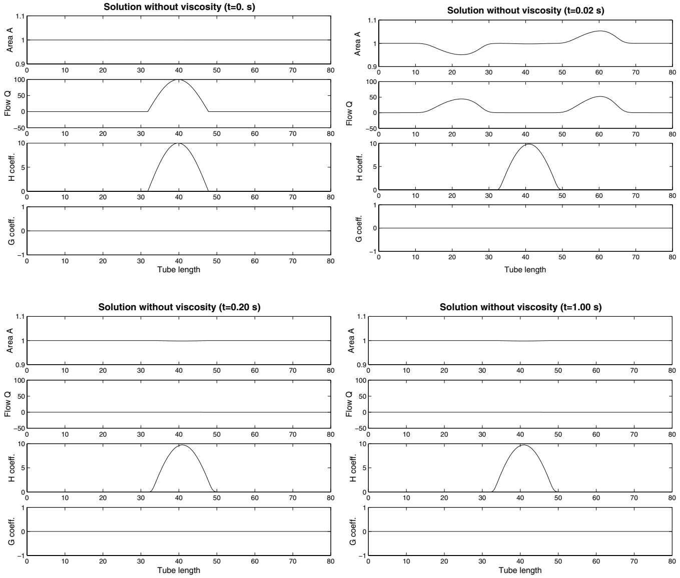

Figure 5.4: Solution at selected time steps for a straight artery of length 80 *cm*. H and G profiles don't propagate; the H profile initialised to a particular value in the starting configuration doesn't disappear because there is no viscosity.

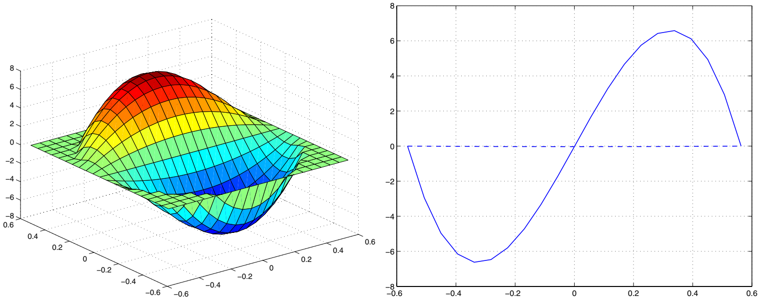

Figure 5.5: On the left velocity profile over a circular section for $z = 40$ *cm* and at the right two projections of the velocity profile along y axes (dotted line) and along x axes (solid line) for the solution reported in the bottom-left corner of Figure 5.4.

5.2.2 Remark

By neglecting completely the velocity components along x and y in equation (5.1.2) we obtain a system close to the previous one (5.2.6); in quasi-linear form it reads:

$$\frac{\partial \mathbf{U}}{\partial t} + \mathbf{J}\frac{\partial \mathbf{U}}{\partial z} = \mathbf{B}(\mathbf{U}) \tag{5.2.9}$$

where $\mathbf{U} = [A, Q, H, G]^T$ and

$$\mathbf{J} = \begin{bmatrix} 0 & 1 & 0 & 0 \\ -\frac{4}{3}\frac{Q^2}{A^2} - 12\pi\frac{H^2}{A^3} - 12\pi\frac{G^2}{A^3} + \frac{\beta}{2\rho A_0}\sqrt{A} & \frac{8}{3}\frac{Q}{A} & 12\pi\frac{H}{A^2} & 12\pi\frac{G}{A^2} \\ -2\frac{HQ}{A^2} & 2\frac{H}{A} & 2\frac{Q}{A} & 0 \\ -2\frac{GQ}{A^2} & 2\frac{G}{A} & 0 & 2\frac{Q}{A} \end{bmatrix} \tag{5.2.10}$$

$$\mathbf{B} = \begin{bmatrix} 0 \\ -8\pi\nu\frac{Q}{A} \\ -24\pi\nu\frac{H}{A} \\ -24\pi\nu\frac{G}{A} \end{bmatrix} \tag{5.2.11}$$

This system is very close to system (5.2.6): the source term is the same and the only difference in the matrix $\mathbf{J}$ are the entries $\mathbf{J}(3,2)$ and $\mathbf{J}(4,2)$ where the coefficient 2 substitute the coefficient $\frac{5}{2}$.
An analysis, analogous to the one of the previous Section, around the linearized states $H = G = 0$ and $Q = G = 0$, yields that system (5.2.9) is hyperbolic.

5.3 Straight geometry: second simplified model

We consider now a second extension of the model presented in Section 5.1.2: the geometry description is the same as above (Figure 5.1) as well as the physical hypotheses. In particular the pressure is still constant over the section S and we suppose an algebraic law for the vessel wall.
Again the complexity of this new model is increased with respect to the velocity profiles. For the most important component of the velocity field, u_z, we still consider the same expansion as in the previous Section, equation (5.2.1), while for the other two components of the velocity field we consider an expansion over a richer basis $\{1, x, y, x^2, xy, y^2\}$:

$$u_x = o_{x1}(z,t) + o_{x2}(z,t)x + o_{x3}(z,t)y + o_{x4}(z,t)x^2 + o_{x5}(z,t)y^2 + o_{x6}(z,t)xy \tag{5.3.1}$$

$$u_y = o_{y1}(z,t) + o_{y2}(z,t)x + o_{y3}(z,t)y + o_{y4}(z,t)x^2 + o_{y5}(z,t)y^2 + o_{y6}(z,t)xy \tag{5.3.2}$$

Yet as the problem is axi-symmetric we impose a radial displacement:

$$u_x|_{(R\cos\theta, R\sin\theta)} = \dot{\eta}\cos\theta$$

$$u_y|_{(R\cos\theta, R\sin\theta)} = \dot{\eta}\sin\theta$$

and we obtain simplified expressions for u_x and u_y:

$$u_x = o_{x1}(z,t) + \frac{\dot{\eta}}{R}x - \frac{o_{x1}(z,t)}{R^2}\left(x^2 + y^2\right) \tag{5.3.3}$$

$$u_y = o_{y1}(z,t) + \frac{\dot{\eta}}{R}y - \frac{o_{y1}(z,t)}{R^2}\left(x^2 + y^2\right) \tag{5.3.4}$$

Again, as unknowns, we have the area A, the three expansion coefficients for the longitudinal velocity field, a, b, c, but also two coefficients coming from the expansions of the axial velocity components, o_{x1} and o_{y1}.

With respect to the previous model (see Section 5.3) the number of unknowns increases: now we need six equations in order to solve the problem; they are obtained by applying $\mathbf{P_0}$ to equations (5.1.5), (5.1.3), (5.1.4), and $\mathbf{P_0}$,$\mathbf{P_1}$,$\mathbf{P_2}$ to equation (5.1.2). This choice is consistent with the chosen developments for the pressure and the velocity field components.

Again it should be remarked that the divergence equation is imposed only *weakly.*

Defining the following six new variables $A = \pi R^2$, $Q = \frac{\pi}{2}a(z,t)R^2$, $H = \frac{\pi}{12}b(z,t)R^4$, $G = \frac{\pi}{12}c(z,t)R^4$, $\Omega_x = \frac{\pi}{2}o_{x1}(z,t)R^2$, $\Omega_y = \frac{\pi}{2}o_{y1}(z,t)R^2$, we get the following system:

$$\begin{cases} \dfrac{\partial A}{\partial t} + \dfrac{\partial Q}{\partial z} = 0 \\ \dfrac{\partial Q}{\partial t} + \dfrac{4}{3}\dfrac{\partial}{\partial z}\dfrac{Q^2}{A} + 6\pi\dfrac{\partial}{\partial z}\dfrac{H^2}{A^2} + 6\pi\dfrac{\partial}{\partial z}\dfrac{G^2}{A^2} + \dfrac{\beta}{3\rho A_0}\dfrac{\partial}{\partial z}A^{\frac{3}{2}} = -8\pi\nu\dfrac{Q}{A} \\ \dfrac{\partial H}{\partial t} + \dfrac{1}{2}\dfrac{H}{A}\dfrac{\partial Q}{\partial z} + 2\dfrac{\partial}{\partial z}\dfrac{HQ}{A} = -24\pi\nu\dfrac{H}{A} + \dfrac{4}{3}\dfrac{\Omega_x Q}{A} \\ \dfrac{\partial G}{\partial t} + \dfrac{1}{2}\dfrac{G}{A}\dfrac{\partial Q}{\partial z} + 2\dfrac{\partial}{\partial z}\dfrac{GQ}{A} = -24\pi\nu\dfrac{G}{A} + \dfrac{4}{3}\dfrac{\Omega_y Q}{A} \\ \dfrac{\partial \Omega_x}{\partial t} + \dfrac{4}{3}\dfrac{\partial}{\partial z}\dfrac{Q\Omega_x}{A} - \dfrac{1}{2}\dfrac{\partial}{\partial z}\left(\dfrac{H}{A}\dfrac{\partial Q}{\partial z}\right) = -8\pi\nu\dfrac{\Omega_x}{A} \\ \dfrac{\partial \Omega_y}{\partial t} + \dfrac{4}{3}\dfrac{\partial}{\partial z}\dfrac{Q\Omega_y}{A} - \dfrac{1}{2}\dfrac{\partial}{\partial z}\left(\dfrac{G}{A}\dfrac{\partial Q}{\partial z}\right) = -8\pi\nu\dfrac{\Omega_y}{A} \end{cases} \tag{5.3.5}$$

System (5.3.5) is rewritten in quasi-linear form

$$\frac{\partial \mathbf{U}}{\partial t} + \mathbf{J}\frac{\partial \mathbf{U}}{\partial z} = \mathbf{B}(\mathbf{U}) \tag{5.3.6}$$

where $\mathbf{U} = [A, Q, H, G, \Omega_x, \Omega_y]^T$ and

$$\mathbf{J} = \begin{bmatrix} 0 & 1 & 0 & 0 & 0 & 0 \\ -\frac{4}{3}\frac{Q^2}{A^2} - 12\pi\frac{H^2}{A^3} - 12\pi\frac{G^2}{A^3} + \frac{\beta}{2\rho A_0}\sqrt{A} & \frac{8}{3}\frac{Q}{A} & 12\pi\frac{H}{A^2} & 12\pi\frac{G}{A^2} & 0 & 0 \\ -2\frac{HQ}{A^2} & \frac{5}{2}\frac{H}{A} & 2\frac{Q}{A} & 0 & 0 & 0 \\ -2\frac{GQ}{A^2} & \frac{5}{2}\frac{G}{A} & 0 & 2\frac{Q}{A} & 0 & 0 \\ -\frac{4}{3}\frac{Q\Omega_x}{A^2} & \frac{4}{3}\frac{\Omega_x}{A} & 0 & 0 & \frac{4}{3}\frac{Q}{A} & 0 \\ -\frac{4}{3}\frac{Q\Omega_y}{A^2} & \frac{4}{3}\frac{\Omega_y}{A} & 0 & 0 & 0 & \frac{4}{3}\frac{Q}{A} \end{bmatrix} \tag{5.3.7}$$

$$\mathbf{B} = \begin{bmatrix} 0 \\ -8\pi\nu\frac{Q}{A} \\ -24\pi\nu\frac{H}{A} + \frac{4}{3}\frac{\Omega_x Q}{A} \\ -24\pi\nu\frac{G}{A} + \frac{4}{3}\frac{\Omega_y Q}{A} \\ -8\pi\nu\frac{\Omega_x}{A} + \mathbf{\frac{1}{2}\frac{\partial}{\partial z}\left(\frac{H}{A}\frac{\partial Q}{\partial z}\right)} \\ -8\pi\nu\frac{\Omega_y}{A} + \mathbf{\frac{1}{2}\frac{\partial}{\partial z}\left(\frac{G}{A}\frac{\partial Q}{\partial z}\right)} \end{bmatrix} \tag{5.3.8}$$

Again system (5.3.6) is solved by a finite difference upwind scheme

$$\mathbf{U}_j^{n+1} = \mathbf{U}_j^n - \frac{\Delta t}{\Delta z}\mathbf{A}^+\left(\mathbf{U}_j^n - \mathbf{U}_{j-1}^n\right) - \frac{\Delta t}{\Delta z}\mathbf{A}^-\left(\mathbf{U}_{j+1}^n - \mathbf{U}_j^n\right) + \Delta t\mathbf{B}_j^n \qquad j = 1, n_{nodes}\ ,\ t = t^n$$

where $\mathbf{A}^{\pm} = \mathbf{R}\mathbf{\Lambda}^{\pm}\mathbf{R}^{-1}$, $\mathbf{\Lambda}^+ = \text{diag}(\lambda_i^+) = \text{diag}(\max(\lambda_i, 0))$, $\mathbf{\Lambda}^- = \text{diag}(\lambda_i^-) = \text{diag}(\min(\lambda_i, 0))$, λ_i are the eingenvalues of the matrix $\mathbf{J}$ and $\mathbf{R}$ is the matrix of right eigenvectors.

Again, non reflecting boundary conditions are imposed, consistently with the hyperbolic nature of the system, by a pseudo-characteristics method [80].

5.3.1 Numerical results

In Figures 5.6 and 5.7 the solutions of a test case ($\rho = 1\ gr/cm^3$, $A_0 = 1\ cm^2$, $\beta = 10^6\ gr/s^2$; $\nu = 0.035\ cm^2/s$ and $\nu = 0\ cm^2/s$ for the case with and without viscosity, respectively) are presented. For the solution a time step $\Delta t = 0.0001\ s$ and a space discretization $\Delta z = 0.2\ cm$ were used. In the start configuration (solution at $t = 0\ s$) $A = A_0$ and $G = \Omega_x = \Omega_y = 0$, while Q and H have an assigned profile (half sine function with $Q_{max} = 100\ cm^3/s$ and $H_{max} = 10\ cm^4/s$). As the tube is straight there is not propagation of the H profile which goes to zero slowly due to the presence of a source term depending on the fluid viscosity ν. The results for the same test case, but setting to zero the fluid viscosity, are reported in Figure

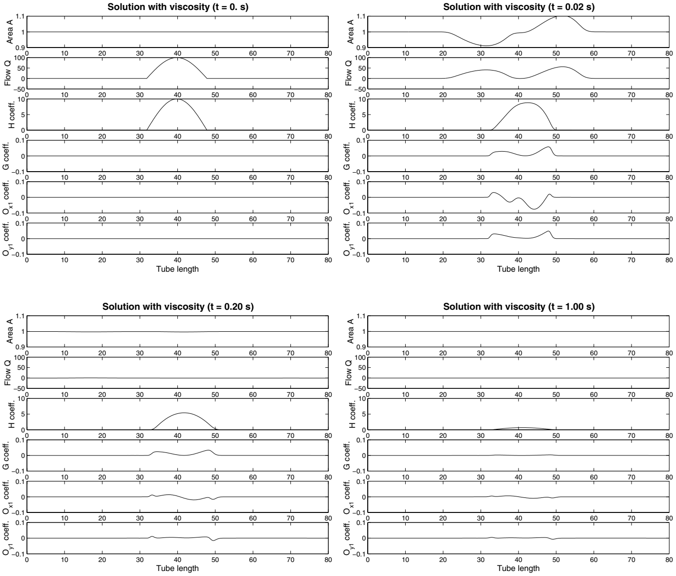
Solution with viscosity (t = 0. s)

Solution with viscosity (t = 0.02 s)

Solution with viscosity (t = 0.20 s)

Solution with viscosity (t = 1.00 s)

Figure 5.6: Solution at selected time steps for a straight artery of lenght 80 *cm*. H, G, Ω_x and Ω_y profiles don't propagate; they are different from zero because of the initialization of the H profile and they disappear because of fluid viscosity.

5.7. In this case the variables H, G, Ω_x and Ω_y are not equal to zero, when time increases the velocity field seems to be rich enough to represent a vortex which does not desappear. In fact because of the absence of fluid viscosity there is no energy dissipation. More precisely the coupling between the various velocity coefficients implies that they can be different from zero, when time increases, even if they are null in the initial configuration.

5.4 Curved geometry: first simplified model

The domain Ω_t is a curved cylinder of constant curvature radius C (with axis oriented along the curvilinear coordinate χ), as depicted in Figure 5.8. For this geometry the metric is $g^{\frac{1}{2}} = \frac{y+C}{C}$. Yet we assume the pressure constant over a section S, that is $p = \bar{p}(\chi)$, and an algebraic law for the vessel wall.
We consider that the velocity along the χ axis has the form

$$u_\chi = \left(1 - \frac{x^2 + y^2}{R^2}\right)\left(a(\chi, t) + b(\chi, t)x + c(\chi, t)y\right) \tag{5.4.1}$$

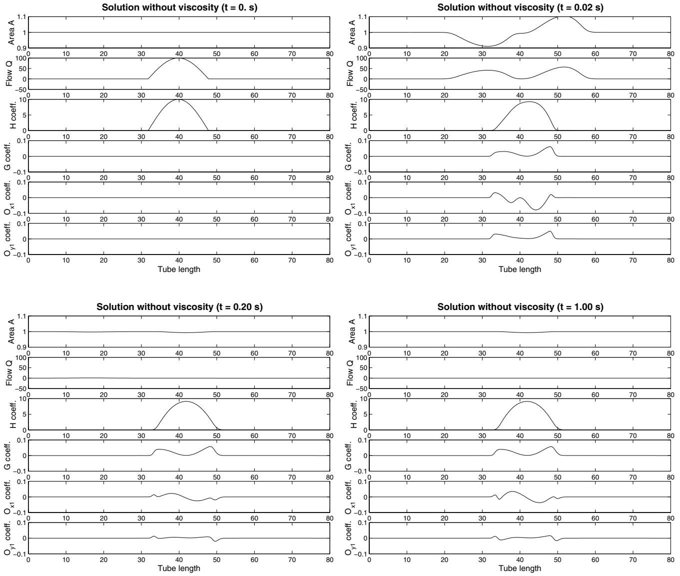
Solution without viscosity (t = 0. s)

Solution without viscosity (t = 0.02 s)

Solution without viscosity (t = 0.20 s)

Solution without viscosity (t = 1.00 s)

Figure 5.7: Solution at selected time steps for a straight artery of lenght 80 *cm*. H, G, Ω_x and Ω_y profiles don't propagate; they are different from zero because of the initialization of the H profile and they don't disappear because the fluid has no viscosity. This should be regarded as a vortex which doesn't dissipate his energy.

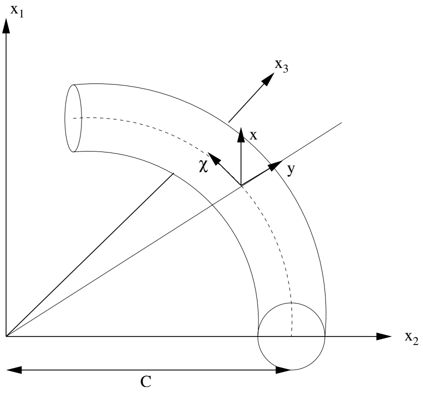

Figure 5.8: The cylindrical domain Ω_t. The cylinder axis has a constant curvature C. The axial sections χ =const. remain circular at all times. χ is belong to the plane $x_2 - x_3$

while the other two components of the velocity field are

$$u_x = \frac{\dot{\eta}}{R}x \qquad , \qquad u_y = \frac{\dot{\eta}}{R}y \tag{5.4.2}$$

These linear profiles are obtained by straightforward calculations by assuming a linear profile, as already done in Section 5.2. A simpler hypothesis could be to neglect completely the u_x and u_y velocity components in equation (5.1.2): this is reported in Section 5.4.2.

The unknowns of the problem are R, a, b, c. The four equations needed to close the system are obtained by applying $\mathbf{P_0}$ to equation (5.1.5), and $\mathbf{P_0}$,$\mathbf{P_1}$,$\mathbf{P_2}$ to equation (5.1.2).
Defining the following variables $A = \pi R^2$, $Q = \frac{\pi}{2}aR^2$, $H = \frac{\pi}{12}bR^4$, $G = \frac{\pi}{12}cR^4$ we get the system, for $z \in (0, L), t > 0$

$$\left\{ \begin{array}{l} \dfrac{\partial A}{\partial t} + \dfrac{\partial Q}{\partial \chi} = 0 \\ \dfrac{\partial Q}{\partial t} + \dfrac{1}{C}\dfrac{\partial G}{\partial t} + \dfrac{4}{3}\dfrac{\partial}{\partial \chi}\dfrac{Q^2}{A} + 6\pi\dfrac{\partial}{\partial \chi}\dfrac{H^2}{A^2} + 6\pi\dfrac{\partial}{\partial \chi}\dfrac{G^2}{A^2} + \\ \qquad \dfrac{\beta}{2\rho A_0}\sqrt{A}\dfrac{\partial A}{\partial \chi} = -8\pi\nu\dfrac{Q}{A} - \dfrac{1}{C}24\pi\nu\dfrac{G}{A} \\ \dfrac{\partial H}{\partial t} + 2\dfrac{\partial}{\partial \chi}\dfrac{HQ}{A} + \dfrac{1}{2}\dfrac{H}{A}\dfrac{\partial Q}{\partial \chi} = -24\pi\nu\dfrac{H}{A} \\ \dfrac{\partial G}{\partial t} + \dfrac{1}{C}\dfrac{1}{6\pi}\dfrac{\partial}{\partial t}(QA) + 2\dfrac{\partial}{\partial \chi}\dfrac{GQ}{A} + \dfrac{1}{2}\dfrac{G}{A}\dfrac{\partial Q}{\partial \chi} + \dfrac{1}{C}\dfrac{\beta}{8\pi\rho A_0}A^{\frac{3}{2}}\dfrac{\partial A}{\partial \chi} = -24\pi\nu\dfrac{G}{A} - \dfrac{1}{C}3\nu Q \end{array} \right. \tag{5.4.3}$$

In quasi-linear form it is rewritten as

$$\mathbf{A}\frac{\partial \mathbf{U}}{\partial t} + \mathbf{J}\frac{\partial \mathbf{U}}{\partial z} = \mathbf{B}(\mathbf{U}) \tag{5.4.4}$$

where $\mathbf{U} = [A, Q, H, G]^T$ and

$$\mathbf{A} = \begin{bmatrix} 1 & 0 & 0 & 0 \\ 0 & 1 & 0 & \dfrac{1}{C} \\ 0 & 0 & 1 & 0 \\ \dfrac{1}{6\pi C}Q & \dfrac{1}{6\pi C}A & 0 & 1 \end{bmatrix} \tag{5.4.5}$$

$$\mathbf{J} = \begin{bmatrix} 0 & 1 & 0 & 0 \\ -\frac{4}{3}\frac{Q^2}{A^2} - 12\pi\frac{H^2}{A^3} - 12\pi\frac{G^2}{A^3} + \frac{\beta}{2\rho A_0}\sqrt{A} & \frac{8}{3}\frac{Q}{A} & 12\pi\frac{H}{A^2} & 12\pi\frac{G}{A^2} \\ -2\frac{HQ}{A^2} & \frac{5}{2}\frac{H}{A} & 2\frac{Q}{A} & 0 \\ -2\frac{GQ}{A^2} + \frac{\beta}{8\pi C\rho A_0}A^{\frac{3}{2}} & \frac{5}{2}\frac{G}{A} & 0 & 2\frac{Q}{A} \end{bmatrix} \tag{5.4.6}$$

$$\mathbf{B} = \begin{bmatrix} 0 \\ -8\pi\nu\dfrac{Q}{A} - \dfrac{1}{C}24\pi\nu\dfrac{G}{A} \\ -24\pi\nu\dfrac{H}{A} \\ -24\pi\nu\dfrac{G}{A} - \dfrac{1}{C}3\nu Q \end{bmatrix} \tag{5.4.7}$$

If now we consider the limit $C \to \infty$ (this is the limit curved geometry versus straight geometry), we remark that system (5.4.3) becomes system (5.2.5), as it was expected.
Moreover it should be noticed that the equation for the H profile doesn't change with respect to the straight geometry, being the problem symmetric with respect to the x-axis in the chosen (χ, x, y) coordinate system.

We hypothize that system (5.4.3) is hyperbolic and we solve it by the following finite difference upwind scheme

$$\mathbf{U}_j^{n+1} = \mathbf{U}_j^n - \frac{\Delta t}{\Delta z}\mathbf{A}^{-1}|_{t=t^n}\mathbf{L}^+\left(\mathbf{U}_j^n - \mathbf{U}_{j-1}^n\right) - \frac{\Delta t}{\Delta z}\mathbf{A}^{-1}|_{t=t^n}\mathbf{L}^-\left(\mathbf{U}_{j+1}^n - \mathbf{U}_j^n\right) + \Delta t\mathbf{A}^{-1}|_{t=t^n}\mathbf{B}_\mathbf{j}^\mathbf{n}$$

$$j = 1, n_{nodes}\ ,\ t = t^n$$

where $\mathbf{L}^\pm = \mathbf{R}\mathbf{\Lambda}^\pm\mathbf{R}^{-1}$, $\mathbf{\Lambda}^+ = \mathrm{diag}(\lambda_i^+) = \mathrm{diag}(\max(\lambda_i, 0))$, $\mathbf{\Lambda}^- = \mathrm{diag}(\lambda_i^-) = \mathrm{diag}(\min(\lambda_i, 0))$, λ_i are the eingenvalues of the matrix $\mathbf{J}$ and $\mathbf{R}$ is the matrix of right eigenvectors, to be computed numerically.
Numerically it was verified that the eigenvalues of the matrix $\mathbf{J}$ are real and, hence, that system (5.4.8) is hyperbolic.
Non-reflecting boundary conditions are imposed by a pseudo-characteristics method, as done for system (5.2.6).

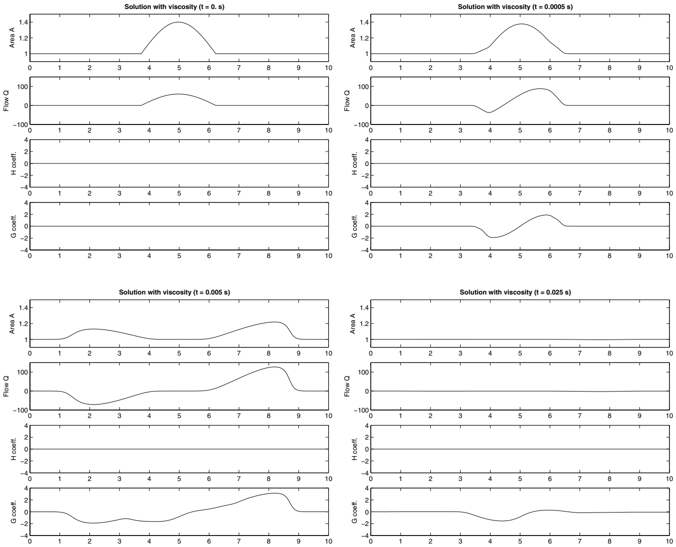

Figure 5.9: Solution at selected time steps for a curved artery ($C = 1$ cm) of length 10 cm. Because of problem simmetry the H profile, null in the initial configuration, remains null for all t, while the G profile is different from zero and propagates because of curvature.

5.4.1 Numerical results

We have considered curved arteries with different curvature radius (for instance $C = 1$ cm or $C = 5$ cm) and with the following physical properties: $\rho = 1$ gr/cm^3, $\nu = 0.035$ cm^2/s, $A_0 = 1$ cm^2, $\beta = 10^6$ gr/s^2.

In Figure 5.9 the solution at different time steps for an artery of curvature $C = 1$ cm is reported. At the starting configuration the variables A and Q are initialised at a value different from the constant one (they are half-sine functions with amplitude 1.4 cm^2 and 60 cm^3/s, respectively). This causes two waves propagating forward and backward, respectively. In particular we remark the propagation of the G profile, while the H profile is null; actually this is due to the particular symmetry of the problem at hand.

The problem of a wave propagating into curved arteries was addressed in two other numerical experiments, whom results are reported in Figures 5.10 and 5.13. In these cases inlet boundary conditions were imposed on pseudo-characteristic variables. Yet it should be noted that the H profile doesn't activate.

In Figures 5.11 and 5.12 we report some velocity profiles for the test case of Figure 5.13, in order to show which kind of result we get.

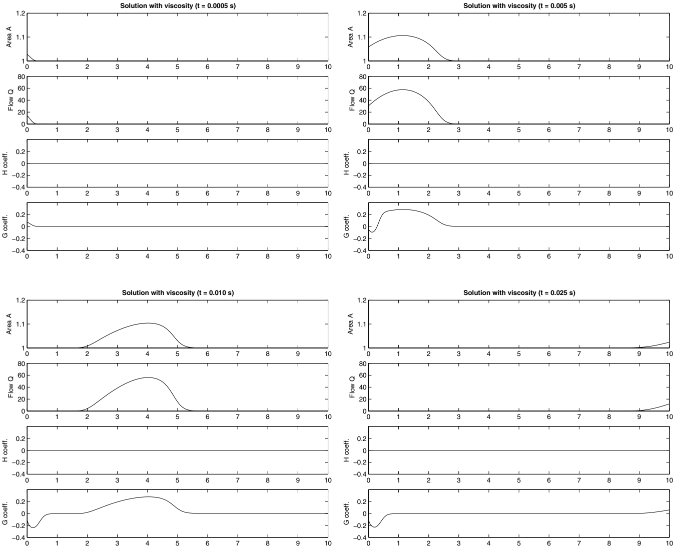

Figure 5.10: Solution at selected time steps for a curved artery ($C = 5\ cm$) of length 10 *cm*. This problem descibes the propagation of a wave imposed at inlet througth pseudo-characteristic. Because of problem simmetry the H profile, null in the initial configuration, remains null for all t, while the G profile is different from zero and propagates because of curvature.

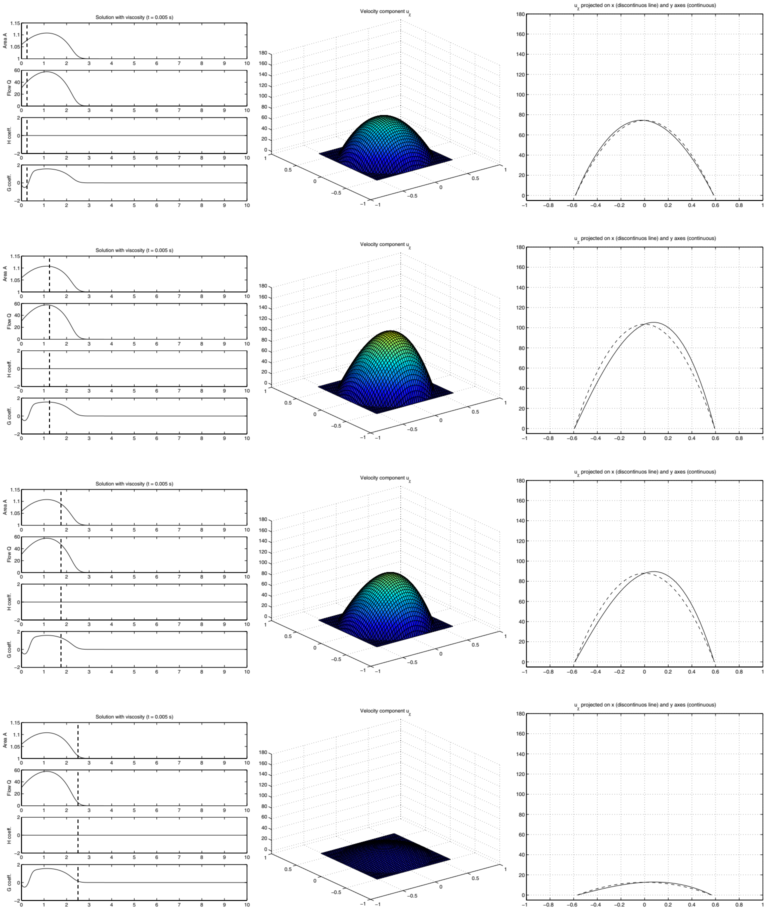

Figure 5.11: Solution at different places, fixed time ($t = 0.0025\ s$), with viscosity, for $C = 1$ cm. The first column in combination with the other two shows the relation between the expansion profile G and the velocity component along the longitudinal axis χ. The asymmetry of the velocity profile is clearly pointed out.

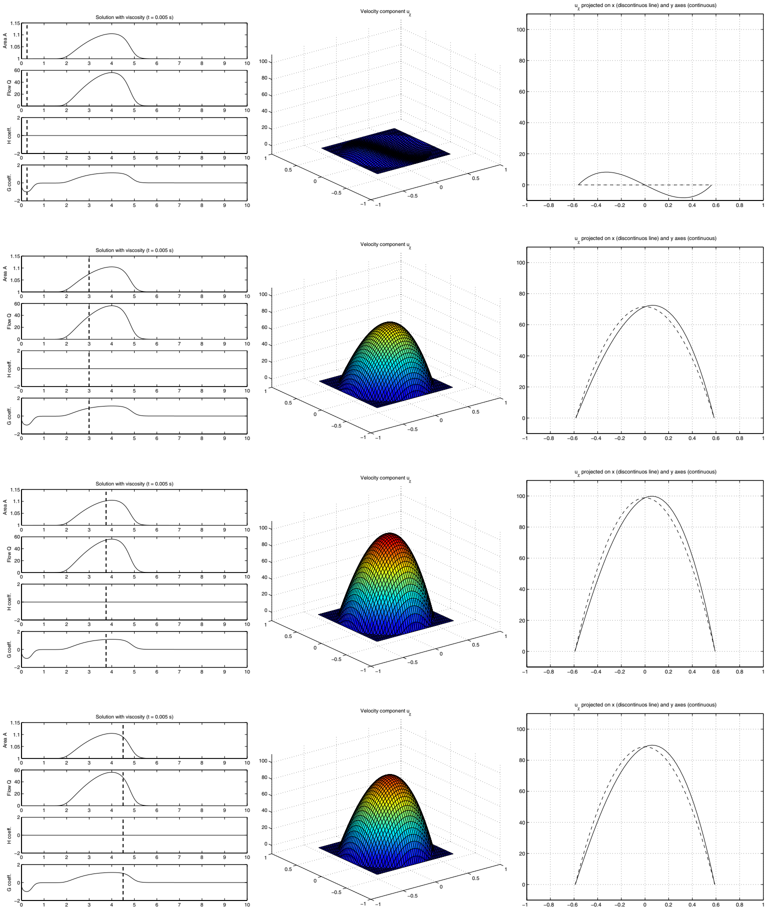

Figure 5.12: Solution at different places, fixed time ($t = 0.005\ s$), with viscosity, for $C = 1\ cm$. The first column in combination with the other two shows the relation between the expansion profile G and the velocity component along the longitudinal axis χ. The asymmetry of the velocity profile is clearly pointed out.

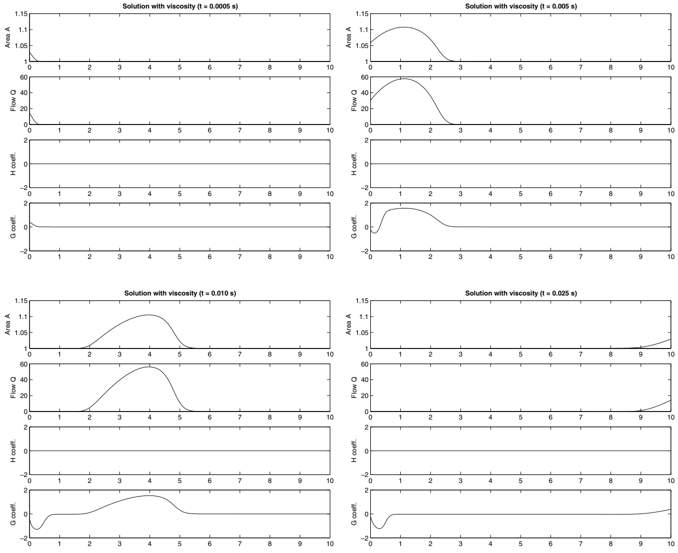

Solution with viscosity (t = 0.0005 s)

Solution with viscosity (t = 0.005 s)

Solution with viscosity (t = 0.010 s)

Solution with viscosity (t = 0.025 s)

Figure 5.13: Solution at selected time steps for a curved artery ($C = 1\ cm$) of length 10 cm. This problem descibes the propagation of a wave imposed at inlet througth pseudo-characteristic. Because of problem simmetry the H profile, null in the initial configuration, remains null for all t, while the G profile is different from zero and propagates because of curvature.

5.4.2 Remark

Neglecting completely the velocity along x and y we obtain a system close to the previous one; in quasi-linear form it reads:

$$\mathbf{A}\frac{\partial \mathbf{U}}{\partial t} + \mathbf{J}\frac{\partial \mathbf{U}}{\partial z} = \mathbf{B}(\mathbf{U}) \tag{5.4.8}$$

where $\mathbf{U} = [A, Q, H, G]'$ and

$$\mathbf{A} = \begin{bmatrix} 1 & 0 & 0 & 0 \\ 0 & 1 & 0 & \dfrac{1}{C} \\ 0 & 0 & 1 & 0 \\ \dfrac{1}{6\pi C}Q & \dfrac{1}{6\pi C}A & 0 & 1 \end{bmatrix} \tag{5.4.9}$$

$$\mathbf{J} = \begin{bmatrix} 0 & 1 & 0 & 0 \\ -\frac{4}{3}\frac{Q^2}{A^2} - 12\pi\frac{H^2}{A^3} - 12\pi\frac{G^2}{A^3} + \frac{\beta}{2\rho A_0}\sqrt{A} & \frac{8}{3}\frac{Q}{A} & 12\pi\frac{H}{A^2} & 12\pi\frac{G}{A^2} \\ -2\frac{HQ}{A^2} & 2\frac{H}{A} & 2\frac{Q}{A} & 0 \\ -2\frac{GQ}{A^2} + \frac{\beta}{8\pi C\rho A_0}A^{\frac{3}{2}} & 2\frac{G}{A} & 0 & 2\frac{Q}{A} \end{bmatrix} \tag{5.4.10}$$

$$\mathbf{B} = \begin{bmatrix} 0 \\ -8\pi\nu\dfrac{Q}{A} - \dfrac{1}{C}24\pi\nu\dfrac{G}{A} \\ -24\pi\nu\dfrac{H}{A} \\ -24\pi\nu\dfrac{G}{A} - \dfrac{1}{C}3\nu Q \end{bmatrix} \tag{5.4.11}$$

This system is very close to system (5.4.4); the source term is the same and the only difference in the matrix $\mathbf{J}$ is in $\mathbf{J}(3,2)$ and $\mathbf{J}(4,2)$ where the coefficient 2 substitute the coefficient $\frac{5}{2}$.

5.4.3 A numerical comparison between the curved model and the straight tube

As it was remarked so far (see Chapter 1) the one dimensional model was developed to describe flow rate and pressure in the human circulatory system.

Here we report some numerical comparisons between the straight artery solution and the curved ones (with different curvatures). We report the comparison for A, Q and G (H being null) having in mind that what we are looking for are the first two variables. What we would like to understand is the influence of the curvature on the solution, with respect to the averaged quantities.

An artery of length 10 cm was then considered with $\beta = 10^6$ gr/s^2 and area at rest of 1 cm^2. Four curvature's radii (C) were considered: $C = \infty$ (this case corresponds to the straight geometry), $C = 10$ cm, $C = 5$ cm and $C = 1$ cm. This last should be interpreted as a spiral where torsion effects are neglected. For the numerical simulation a time discretization Δt of 0.00001 s was used and a space discretization Δx of 0.025 cm. The total time T of the simulation was $T = 0.02$ s. At inlet we impose a flow rate $Q(t) = \tilde{Q}\sin(\pi t/0.006)$ if $t < 0.006$ s and $Q(t) = 0$ if $t > 0.006$ s.

In Figures 5.14 and 5.15 are reported the results for a straight artery and the difference between curved arteries, the flow velocity amplitude ($\tilde{Q}/A_0$) being 30 cm/s in the first and 80 cm/s in the second.

In both regimes we remark that instead of an important variation in the velocity profiles the averaged quantities (area A and flow rate Q) don't have a relevant variation. Only in the case of $C = 1$ cm the flow rate shows a variation of order 10%.

Yet this is a non-physiological wave, in particular with respect to the wavelength. A more physiological test ($Q(t) = \tilde{Q}\sin(\pi t/0.3)$ if $t < 0.3$ s and $Q(t) = 0$ if $t > 0.3$ s, $\tilde{Q} = 80$ cm^3/s) is reported in Figure 5.16, where no relevant differences can be remarked between the curved and the straight models.

5.5 Curved geometry: more complex models

We consider now the same profile for the velocity along the χ axis, namely

$$u_\chi = \left(1 - \frac{x^2+y^2}{R^2}\right)\left(a(\chi,t) + b(\chi,t)x + c(\chi,t)y\right) \tag{5.5.1}$$

while u_x and u_y are given by

$$u_x = o_{x1}(\chi,t) + o_{x2}(\chi,t)x + o_{x3}(\chi,t)y + o_{x4}(\chi,t)x^2 + o_{x5}(\chi,t)y^2 + o_{x6}(\chi,t)xy \tag{5.5.2}$$

$$u_y = o_{y1}(\chi,t) + o_{y2}(\chi,t)x + o_{y3}(\chi,t)y + o_{y4}(\chi,t)x^2 + o_{y5}(\chi,t)y^2 + o_{y6}(\chi,t)xy \tag{5.5.3}$$

Imposing that the displacement is radial:

$$u_x|_{(R\cos\theta, R\sin\theta)} = \dot{\eta}\cos\theta$$

$$u_y|_{(R\cos\theta, R\sin\theta)} = \dot{\eta}\sin\theta$$

we obtain simplified expressions for u_x and u_y:

$$u_x = o_{x1}(\chi,t) + \frac{\dot{\eta}}{R}x - \frac{o_{x1}(\chi,t)}{R^2}\left(x^2+y^2\right) \tag{5.5.4}$$

$$u_y = o_{y1}(\chi,t) + \frac{\dot{\eta}}{R}y - \frac{o_{y1}(\chi,t)}{R^2}\left(x^2+y^2\right) \tag{5.5.5}$$

The unknowns of our problem are $R, a, b, c, o_{x1}, o_{y1}$. The six equations needed to close the system are obtained by applying the operator $\mathbf{P_0}$ to equations (5.1.5), (5.1.3), (5.1.4), and the operators $\mathbf{P_0}$,$\mathbf{P_1}$,$\mathbf{P_2}$ to equation (5.1.2).

In order to recover more familiar expressions we perform the change of variables $A = \pi R^2$, $Q = \frac{\pi}{2}aR^2$, $H = \frac{\pi}{12}bR^4$, $G = \frac{\pi}{12}cR^4$, $\Omega_x = \frac{\pi}{2}o_{x1}R^2$ and $\Omega_y = \frac{\pi}{2}o_{y1}R^2$.

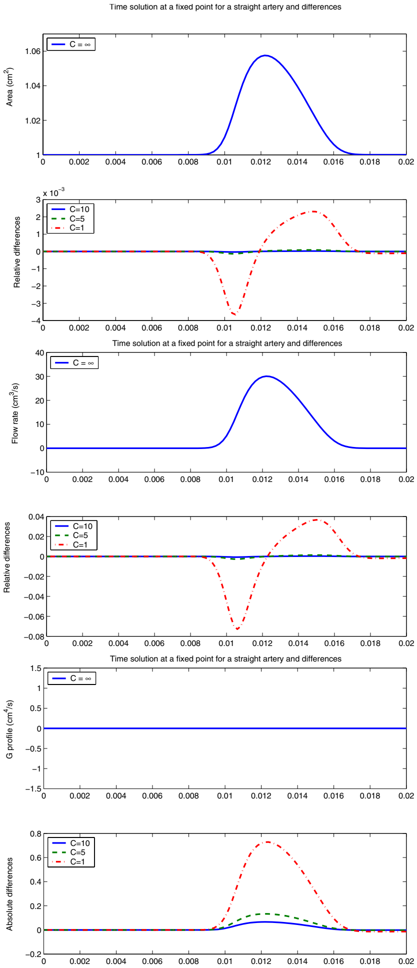

Figure 5.14: Time solution in the middle of the artery for area, flow rate and G profile for the straight geometry and its comparison with the solution for curved geometries, C being the curvature radius. For the variable area A and flow rate Q the relative difference is considered while for the G profile we have considered the absolute difference.

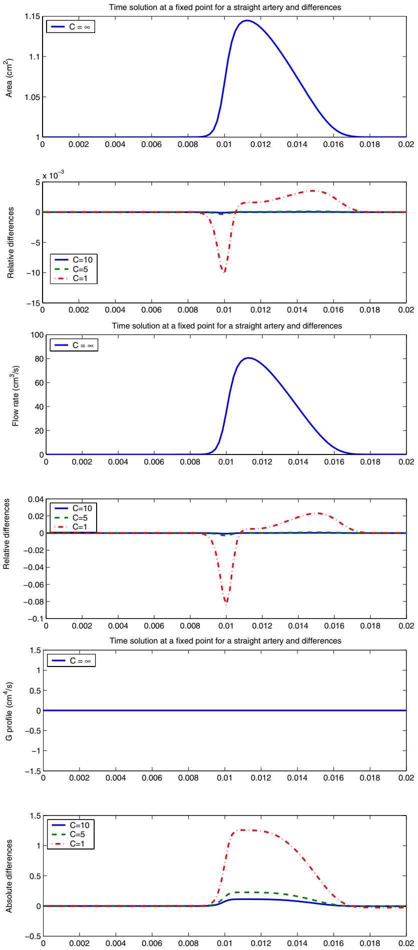

Figure 5.15: Time solution in the middle of the artery for area, flow rate and G profile for the straight geometry and its comparison with the solution for curved geometries, C being the curvature radius. For the variable area A and flow rate Q the relative difference is considered while for the G profile we have considered the absolute difference.

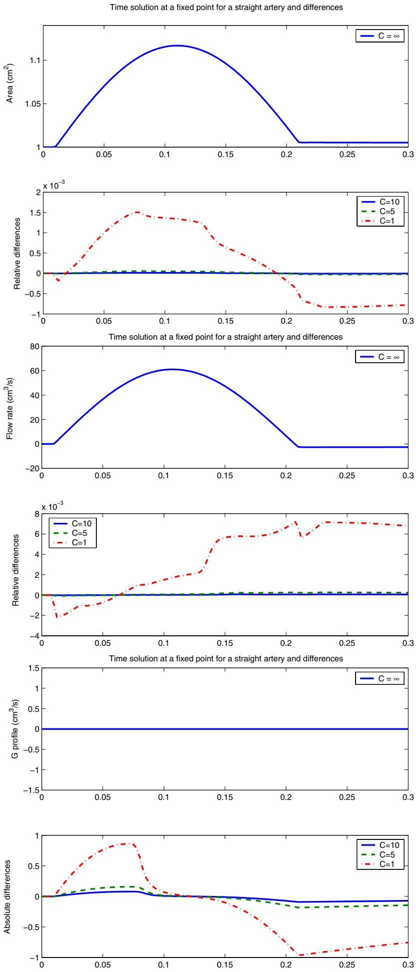

Figure 5.16: Time solution in the middle of the artery for area, flow rate and G profile for the straight geometry and its comparison with the solution for curved geometries, C being the curvature radius. For the variable area A and flow rate Q the relative difference is considered while for the G profile we have considered the absolute difference.

Therefore, we get the following 6 by 6 system:

$$
\left\{
\begin{array}{l}
\dfrac{\partial A}{\partial t} + \dfrac{\partial Q}{\partial \chi} = 0 \\[2ex]
\dfrac{\partial Q}{\partial t} + \dfrac{1}{C}\dfrac{\partial G}{\partial t} + \dfrac{4}{3}\dfrac{\partial}{\partial \chi}\dfrac{Q^2}{A} + 6\pi\dfrac{\partial}{\partial \chi}\dfrac{H^2}{A^2} + 6\pi\dfrac{\partial}{\partial \chi}\dfrac{G^2}{A^2} + \dfrac{\beta}{2\rho A_0}\sqrt{A}\dfrac{\partial A}{\partial \chi} = -8\pi\nu\dfrac{Q}{A} - \dfrac{1}{C}24\pi\nu\dfrac{G}{A} \\[2ex]
\dfrac{\partial H}{\partial t} + 2\dfrac{\partial}{\partial \chi}\dfrac{HQ}{A} + \dfrac{1}{2}\dfrac{H}{A}\dfrac{\partial Q}{\partial \chi} = +\dfrac{4}{3}\dfrac{Q\Omega_x}{A} + \dfrac{1}{C}\dfrac{G\Omega_x}{A} - 24\pi\nu\dfrac{H}{A} \\[2ex]
\dfrac{\partial G}{\partial t} + \dfrac{1}{C}\dfrac{1}{6\pi}\dfrac{\partial}{\partial t}(QA) + 2\dfrac{\partial}{\partial \chi}\dfrac{GQ}{A} + \dfrac{1}{2}\dfrac{G}{A}\dfrac{\partial Q}{\partial \chi} + \dfrac{1}{C}\dfrac{\beta}{8\pi\rho A_0}A^{\frac{3}{2}}\dfrac{\partial A}{\partial \chi} = \\[2ex]
\qquad\qquad\qquad\qquad\qquad + \dfrac{4}{3}\dfrac{Q\Omega_y}{A} + \dfrac{1}{C}\dfrac{G\Omega_y}{A} - 24\pi\nu\dfrac{G}{A} - \dfrac{1}{C}3\nu Q \\[2ex]
\dfrac{\partial \Omega_x}{\partial t} + \dfrac{4}{3}\dfrac{\partial}{\partial \chi}\dfrac{Q\Omega_x}{A} - \dfrac{1}{2}\dfrac{\partial}{\partial \chi}\left(\dfrac{H}{A}\dfrac{\partial Q}{\partial \chi}\right) = -8\pi\nu\dfrac{\Omega_x}{A} \\[2ex]
\dfrac{\partial \Omega_y}{\partial t} + \dfrac{1}{C}\dfrac{1}{8\pi}\dfrac{\partial}{\partial t}\left(A\dfrac{\partial A}{\partial t}\right) + \dfrac{1}{C}\dfrac{1}{4\pi}\left(\dfrac{\partial Q}{\partial \chi}\right)^2 - \dfrac{1}{C}\dfrac{\nu}{2}\dfrac{\partial Q}{\partial \chi} + \dfrac{4}{3}\dfrac{\partial}{\partial \chi}\dfrac{Q\Omega_y}{A} - \dfrac{1}{2}\dfrac{\partial}{\partial \chi}\left(\dfrac{G}{A}\dfrac{\partial Q}{\partial \chi}\right) = -8\pi\nu\dfrac{\Omega_y}{A}
\end{array}
\right.
\tag{5.5.6}
$$

As expected, increasing the expansions of the velocity profiles, we finally find a mixed hyperbolic-parabolic system (5.5.6).

System (5.5.6) has not yet been numerically solved and is here reported to show the limit of our "Naghdi-Green" approach: despite its absolute generality, the complexity of the resulting system increases rapidly when increasing the accuracy of the approximation.

Moreover a mixed type system (hyperbolic-parabolic) should be expected.

Part II

A multiscale simulation of the human arterial system

Chapter 6

Models and methods

Introduction

In this Chapter we consider the arterial network model proposed in [91], where the 55 largest arteries are represented by 1D models well-matched at the bifurcations for forward propagating waves. The parameters specifying the mechanical and physical features of each vessel are basically deduced from [105] and [97], later adjusted in [104]. Normally, the action of the heart is represented by a boundary conditon to be prescribed at the inlet of the first artery (ascending aorta) of the network. However, it is well known that "the left ventricle and arterial circulation represent two mechanical units that are joined together to form a coupled biological system" [59, Chapter 13]. The relevance of the heart-arterial interaction in mathematical modeling has been pointed out in [88, 87], in the framework of lumped parameter models. The reduction of the heart action to a boundary condition for the system does not account at all for this coupling. This approach is unsatisfactory in particular when we want to study the effect on the pressure and flow patterns caused by changes in the geometrical or mechanical characteristics of the arterial network (e.g. due to the presence of a prothesis in the iliac bifurcation). No feedback from the arterial tree to the heart is indeed being modelled in this way. Here, we propose to overcome this drawback by a coupled description based on the matching of the 1D network model with a lumped parameter model for the left ventricle. In particular, we refer to the model illustrated in [59] and in [45], together with a technique that accounts for the closure of the aortic valve.
In this Chapter we outline the mathematical model and the numerical methods used, leaving to the next Chapter the application to physiological test cases.

The results reported in this Chapter are taken from [30].

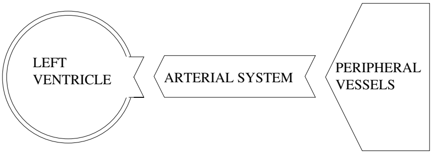

Figure 6.1: Diagramatic representation of the simulated system. The arterial network is described in terms of 1D models, while the heart and the peripheral circulation are given by lumped parameter models.

6.1 The Mathematical Model

We consider the system represented in Figure 6.1, composed by a left ventricle (LV), an arterial system and peripheral vessels. They are here described, respectively, by a lumped parameter model, a one dimensional network and a lumped parameter model.

In this Section, we introduce the basic features of the mathematical model we have adopted. The basic 1D model and the numerical methods adopted for its solution have been presented in Chapters 1 and 2. Since the human arterial system is formed by a network of vessels we need to find a proper way to account for branching. We addressed this issue in Chapter 4.

Finally, the model is completed by accounting for the peripheral circulation and the heart. The former is here modeled by a lumped parameter model which can be regarded as a boundary condition for the 1D network distal sections (Section 6.1.1); the formulation here reported generalises the one based on a pure resistive parameter [91]. The heart can be described either as a boundary condition for the proximal section of the 1D model or through a differential equation. The two approaches are presented in Section 6.1.1; we will see that the former is not suitable to investigate the effect at the level of aortic pressure for changes of the network characteristics. This explains why we introduced the alternative approach, which is of course more complex, consisting in modeling also the heart action through a differential equation.

6.1.1 Boundary conditions for the network

Boundary conditions for the whole model of the arterial network at hand are either distal or proximal. The former has to simulate in a simplified way the presence of the capillary bed. The latter, which is imposed at the proximal node in the ascending aorta, accounts for the action of the heart or, more precisely, of the left ventricle.

Distal conditions (peripheral circulation)

At the distal ends a common choice is to assume that the peripheral circulation corresponds to a purely resistive load (see e.g. [92]). This corresponds to assuming that:

$$p_d = R_p Q_d \tag{6.1.1}$$

where p_d and Q_d are the pressure and the flow rate at the distal end and R_p is the peripheral resistance.

When resorting to non reflecting boundary conditions reformulated in terms of Riemann invariants, we can linearize the characteristic variables given by (1.2.9) in the form:

$$W_1 = a_1 Q + a_2 p, \quad W_2 = a_1 Q - a_2 p$$

where a_1 and a_2 are constant.
Condition (6.1.1) can be therefore rewritten as

$$\frac{W_1 - W_2}{2a_2} = R_p \frac{W_1 + W_2}{2a_1},$$

thence

$$W_2 = -\frac{a_1 - \frac{a_2}{R_p}}{a_1 + \frac{a_2}{R_p}} W_1 = -R_t W_1 \tag{6.1.2}$$

having set $R_t = \left(a_1 - \frac{a_2}{R_p}\right) / \left(a_1 + \frac{a_2}{R_p}\right)$.
This condition states that the back propagating Riemann invariant is (up to the sign) a fraction of the incoming one (see e.g. [92]). For this reason we will refer to R_t as reflection coefficient. Observe, in particular, that if R_p tends to infinity (that means condition (6.1.1) corresponds to a completely blocked end ($Q_p = 0$)) R_t tends to 1, as expected.
The hypothesis that the peripheral circulation can be represented in terms of a resistive impedance is correct for very peripheral vessels [59]. Our model will be used for simulating different scenarios, considering different possible distal boundaries. We therefore generalize the previous condition when the lumped parameter representation of the peripheral circulation is given by a complex impedance Z_p. In particular, if we consider the *three-element Windkessel model* represented in Figure 6.2, the *input impedance* is:

$$Z_p = R_0 + \frac{R_1}{1 + i\omega R_1 C}.$$

Here R_0 and R_1 are resistive parameters while C is a capacitance.
In the time domain, by setting $R_0 + R_1 = R_p$, we have the generalization of the resistive condition (6.1.1):

$$p + R_1 C \frac{dp}{dt} = R_p Q + R_0 R_1 C \frac{dQ}{dt}. \tag{6.1.3}$$

When resorting to the (linearized) Riemann invariants, after some manipulations, condition (6.1.3) becomes:

$$R_1 C \frac{a_2 + \frac{a_1}{R_0}}{a_2 + \frac{a_1}{R_p}} \frac{dW_2}{dt} + W_2 = R_1 C \frac{a_2 - \frac{a_1}{R_0}}{a_2 + \frac{a_1}{R_p}} \frac{dW_1}{dt} - \frac{a_2 - \frac{a_1}{R_p}}{a_2 + \frac{a_1}{R_p}} W_1. \tag{6.1.4}$$

Time integration of (6.1.4) (pursued at the numerical level, as described in Section 6.2) provides the distal boundary conditions.
Observe that if we suppose that R_0 tends to infinity (corresponding to a complete occlusion of the peripheral boundary), if the initial data are compatible (i.e. $Q_P = 0$ at the initial time), it is possible to verify that we still obtain the expected solution $Q_P = 0$.

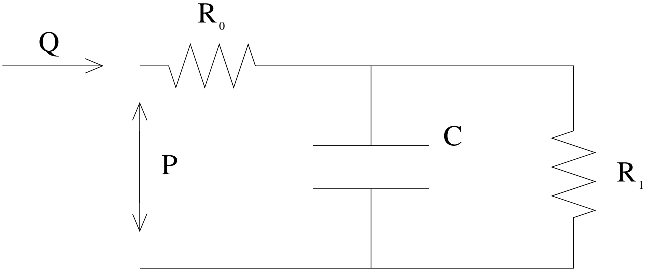

Figure 6.2: Three-elements Windkessel model used for modeling the peripheral circulation.

Proximal Conditions: standard model

At the inlet we need to simulate the presence of the heart and of the aortic valve. Proximal boundary conditions may be further subdivided into two types: *open valve conditions* (OV) and *closed valve conditions* (CV). The change in condition type must be driven by the solution itself. For the sake of simplicity, we detail here OV and CV separately. How to switch between the states in the numerical model is explained in Section 6.2.3.

CV Conditions: When the valve is closed the boundary condition imposed at a given instant at the proximal aortic node is $Q = 0$. In practice we resort to a condition similar to (6.1.2), where now the roles of W_1 and W_2 are exchanged and $R_t = 1$, yielding:

$$W_{1,CV} = -W_2. \tag{6.1.5}$$

OV Conditions: In this situation a classical methodology is to prescribe either the flux or the pressure at the proximal node using a well chosen profile (see Section 1.3). We should note however that prescribing pressure or fluxes is a reflective-type condition. This means that part of the wave going toward the heart will be reflected backward into the network. If this is what we expect when the aortic valve is closed, it may otherwise give unwanted spurious waves in the case of OV conditions, since we are not accounting for the absorbing properties of the ventricle. Smoother results are obtained using instead a non-reflecting boundary condition, by imposing the incoming Riemann invariant W_1, obtained from the profile of the ventricular pressure P_v. As seen in Chapter 1, the incoming Riemann invariant W_1 is written in terms of the pressure and W_2 as follows

$$W_1 = W_2 + 4\sqrt{\frac{2}{\rho}}\left(P_v + \frac{\beta}{\sqrt{A_0}}\right). \tag{6.1.6}$$

In practice P_v has been chosen as a half sine wave of amplitude $P_{v,0}$ and a half-period $t_v = 0.3$ s (see Figure 6.3); the profile will be restarted at every heart beat (we will indicate the heart beat period by T). If we assume that the ventricle acts as a perfectly absorbing chamber, the value of W_2 must remain unchanged and equal to its initial value $W_{2,0}$, readily computed from the initial state at the aortic proximal node. In the general case, the actual value of W_2 is computed by extrapolation (see Section 6.2).

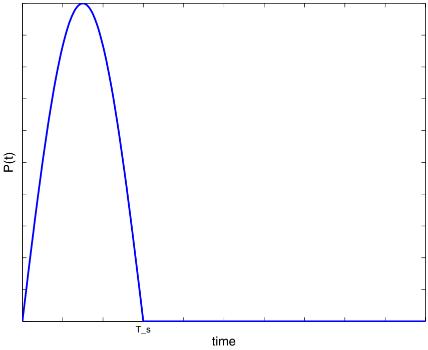

Figure 6.3: Function $P_{v,0}(t)$ for the left-ventricle pressure P_V in the case of standard bounday conditions. $T\_s = 0.3\ s$ is the end-of-systole time.

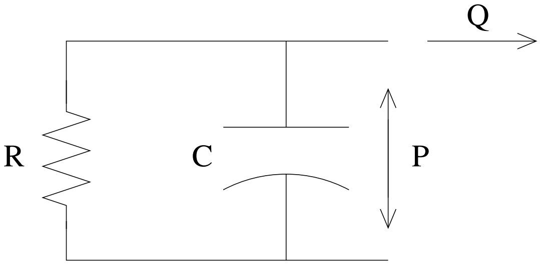

Figure 6.4: Lumped parameter representation of the heart during the systolic phase.

With this method we will not impose the pressure P_v exactly at the proximal node, since we are selecting just the part of information corresponding to the wave entering the network. However, we are now sure that the waves coming from the periphery will be perfectly absorbed. As previously pointed out, this approach does not account at all of the behavior of the heart and of the coupling between the left ventricle and the arterial system, since P_v is given: there is no interaction between the left ventricle and the arterial system.

6.1.2 Lumped parameter description of the heart

We describe here an alternative technique, based on a commonly accepted phenomenological model of the ventricle function. The basic idea of this model, originally proposed in [102, 101] (see also [59, 45, 46, 87, 88]) is that the pressure in the left ventricle and the ventricular volume are linked through a time-dependent coefficient called *elastance* (see Figure 6.5).
In particular, the cardiac stiffness, that is actually measured by the elastance, is low during the

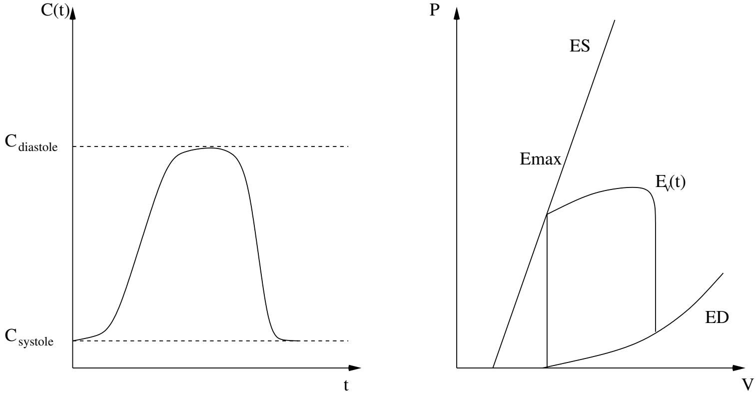

Figure 6.5: On the left: qualitative character of the time-dependent compliance, C(t), of the left ventricle during a cardiac cycle [45]. On the right: qualitative character of the elastance function, $E_v(t)$, in a pressure (P) - volume (V) diagram (E_{max} = ventricular contractility index, ES = end systole, ED = end diastole) [100].

diastole and increases in systole. In [102, 101] it is experimentally shown that the elastance funtion is in fact independent of the ventricular load. We will therefore assume that the ventricle pressure P_v and the ventricular volume V_v are linked by the relation:

$$\begin{aligned} P_v(t) &= E_v(t)(V_v(t) - V_0) + K E_v(t)(V_v - V_0)Q_v(t) \\ &= E_v(t)(V_v(t) - V_0)(1 + K Q_v(t)) \end{aligned} \tag{6.1.7}$$

Here $E_v = E_v(t)$ is a time varying elastance that simulates the action of the heart muscular fibers, V_0 is a reference volume and K is a resistance coefficient (see [59, Chapter 13, eq. (13.4)]). E_v, K and V_0 are intrinsic properties of the ventricle. K is usually rather small, so we will set it to zero. We also assume that V_0 is constant. Observe that the flow rate ejected by the ventricle is given by $Q_v = -dV_v/dt$. During the systole equation (6.1.7) is matched with the 1D network (*OV conditions*). During this phase (when the atrio-ventricular valve is closed), a lumped parameter model for the left ventricle in terms of electric networks is obtained by a time derivation of (6.1.7), yielding:

$$\frac{1}{E}\frac{dP_v}{dt} + \frac{d}{dt}\left(\frac{1}{E}\right)P_v = \frac{dV}{dt} = -Q_v.$$

The presence of the venous system, which is responsible of the pressure increment in the heart during the diastole (*CV conditions*), is not explicitely considered, being the pressure increment still driven by (6.1.7). Moreover the venous system is completely omitted. Thanks to this pressure increment, at the beginning of the systole the capacitance $C = \frac{1}{E}$ of Figure 6.4 is polarized. The systolic phase actually coincides with the depolarization of the capacitor, yielding the blood ejection into the arterial system.

6.2 Numerical methods

6.2.1 Peripheral circulation

At the numerical level, relation (6.1.4) provides an equation for the approximation at time t^{n+1} of W_1 and W_2 at a distal boundaries. More precisely, using the notation

$$s_1 = R_1 C \frac{a_2 + \frac{a_1}{R_0}}{a_2 + \frac{a_1}{R_p}}, \qquad s_2 = R_1 C \frac{a_2 - \frac{a_1}{R_0}}{a_2 + \frac{a_1}{R_p}}, \qquad s_3 = \frac{a_2 - \frac{a_1}{R_p}}{a_2 + \frac{a_1}{R_p}},$$

if we discretize (6.1.4) with a backward Euler scheme, we obtain the equation

$$W_2^{n+1} = \frac{(s_2 - \Delta t s_3) W_1^{n+1} + s_1 W_2^n - s_2 W_1^n}{\Delta t + s_1} \tag{6.2.1}$$

where Δt is the time step. As before, this relation needs to be completed by the extrapolation of the outgoing characteristic. This is also needed by the fact that the right hand side of (6.2.1) depends on W_1^{n+1}.

We therefore obtain the non linear system

$$\begin{cases} W_1(A^{n+1}, Q^{n+1}) = W_{1,\text{ext}}^{n+1} \\ W_2(A^{n+1}, Q^{n+1}) = \dfrac{(s_2 - \Delta t s_3) W_1^{n+1} + s_1 W_2^n - s_2 W_1^n}{\Delta t + s_1} \end{cases} \tag{6.2.2}$$

which is solved with a Newton iterative scheme.

6.2.2 Proximal boundary

Standard conditions

In this case, the boundary condition we prescribe is the incoming Riemann variable W_1 through equation (6.1.5) when the aortic valve is closed, or (6.1.6) when it is open. The other condition is obtained by extrapolating W_2.

In the case of CV conditions, we will therefore set:

$$W_2^{n+1} = W_{2,ext}^{n+1}, \quad W_1^{n+1} = -W_2^{n+1} = -W_{2,ext}^{n+1}. \tag{6.2.3}$$

In the case of OV conditions, having prescribed a ventricular pressure function $P_v(t)$, we will force:

$$\begin{aligned} W_1^{n+1} &= W_{2,\text{ext}}^{n+1} + 4\sqrt{\frac{2}{\rho}} \left(P_v(t^{n+1}) + \frac{\beta}{\sqrt{A_0}} \right) \\ W_2^{n+1} &= W_{2,\text{ext}}^{n+1}, \end{aligned} \tag{6.2.4}$$

Heart model

When accounting for a lumped parameter description of the heart, conditions (6.2.3) are still valid in the case of CV.

For what concerns OV conditions, given the quantities at time t^n, we approximate (6.1.7) to obtain the pressure at time t^{n+1} as follows

$$P_v^{n+1} = E(t^{n+1}) \left(V_v^n - \frac{Q_v^{n+1} + Q_v^n}{2} \Delta t - V_0 \right), \tag{6.2.5}$$

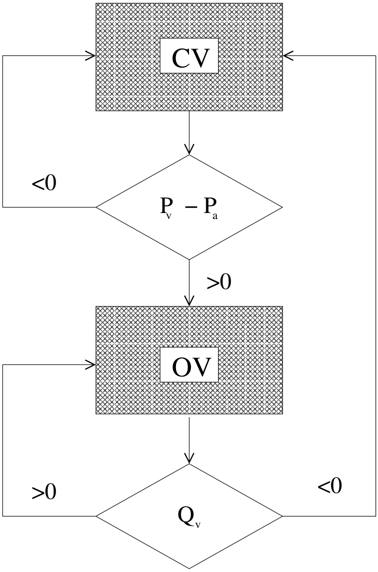

Figure 6.6: Flow chart representation of the aortic valve modeling. The simulation are started from close valve. The close valve condition is imposed till the ventricle pressure is bigger than the aortic pressure; then open valve condition is used until a flow reversal condition, which closes the valve.

where V_v^n is the ventricular volume at $t = t^n$. We assume that when the aortic valve is open the values of P_a and Q_a at the proximal aortic node coincide with P_v and Q_v, respectively.

Equation (6.2.5) and the extrapolation of W_2 are the boundary conditions for the open valve case. We can then update the ventricular volume as $V_v^{n+1} = V_v^n - \dfrac{Q^{n+1} + Q^n}{2}\Delta t$.

To simulate the cardiac cycle, we re-activate the model at each time $t^* = kT$, $k = 0, 1, \ldots$, being T the chosen beat period. At these times we assume that the ventricle is completely filled with $V_v(t^*) = V^*$ being the chosen stroke volume, while $E(t^*)$ corresponds to its lowest value (end diastole). Until the aortic valve opens (see next subsection for the modelling of the valve) we have $Q_v^n = Q_v^{n+1} = 0$ and $V_v^n = V^*$ (isochoric contraction) and (6.2.5) is sufficient to compute P_v^{n+1}. Until the aortic valve remains closed, the ventricular model is completely decoupled from the network model and the proximal boundary condition for the latter is determined by the zero flux condition.

When the aortic valve opens the ventricular and network model are coupled using the technique previously illustrated, until the valve closes again. From that time on, until the next period the models are again decoupled and, in fact, the ventricular model is not used at all.

6.2.3 Aortic valve action

We now describe the technique we have adopted to model the aortic valve action, for both the computations using the classical proximal condition and the heart modeling.

We have assumed that the valve opens under the action of a differential pressure, while it closes under the action of a flow reversal.

The diastolic cycle is started with the valve closed and at each time step P_v^{n+1} is compared to that P_a^{n+1}, the pressure computed by the 1D model at the aortic proximal node. When $P_v^{n+1} - P_a^{n+1} > 0$ the aortic valve is opened and from the successive time step onward we adopt the OV conditions, until the next closure.

Clearly, when the valve opens at the end of the isochoric contraction the ventricular pressure is still rapidly increasing and induces a positive flux into the aorta. To determine the instant of valve closure (end systole) we monitor the sign of the flux at the aortic proximal node. At the first time step when we have $Q_v^{n+1} < 0$ we "close" the valve by adopting again the CV boundary condition, until the next heart cycle. A flow chart representation of the aortic valve action is given in Figure 6.6.

6.3 Numerical tests on proximal boundary condition

In order to understand the role played by the coupling left ventricle - arterial system we did some numerical experiments. We consider the arterial network depicted in Figure 6.7. In each of the 55 straight arteries, we assume equations (1.1.2, 1.1.3) to hold, while bifurcations are described in terms of conservation of mass and total pressure (see Section 4.1.1). The values of the physical parameters (lengths, rest radii, Young's moduli, etc.) are taken from [104] and are reported in Table 6.3. At the outlet of the tree, in correspondence of the peripheral circulation, suitable values for the impedance are prescribed. This case will be denoted as the *physiological* test case.

The heart will be simulated both in the standard way and in the new one. In the former case, when the valve is open P_v is a half-sine curve, as pointed out in Section 6.1.1. In the case of the coupling with the lumped parameter model, it is worthwhile to assign a curve for Q_0, which is still a half-sine curve, as reported in Figure 6.3.

We also simulated two modifications of this model, in order to probe the correctness of the numerical model.

Age effects. We have considered different Young's moduli for different ages, by suitably changing the stiffness of the arteries. More precisely, Young's modulus has been reduced by 100 % in the case of a young patient and increased by 100 % for an elderly patient.

Pathological case. In order to outline the increase of wave reflections, we considered also a case of a complete obstruction of the right femoral artery. This means that in this case the 55 arteries network reduces to a set of 53 vessels, as indicated in Figure 6.8, and the distal conditions on the right femoral artery corresponds to a null distal velocity (complete blockage, $R_t = 1$). In the sequel, simulations referring to network of Figure 6.8 will be denoted by *pathological* case.

In Figure 6.9 we simulate the arterial tree of a middle aged individual and compare results obtained without left ventricle coupling (left column) and with the coupling (right column). In particular, we illustrate the pressure and the velocity of blood for different arteries of the system. The last two pictures in each column refer to the Riemann invariants (W_1 and W_2

#	Name of Artery	Length (cm)	Area (cm^2)	Beta (β)	Reflection coefficient (R_t)
		-	-	(kg/s^2)	-
1	Ascending Aorta	4.0	5.983	388	-
2	Aortic Arch I	2.0	5.147	348	-
3	Brachiocephalic	3.4	1.219	932	-
4	R. Subclavian I	3.4	0.562	1692	-
5	R. Carotid	17.7	0.432	2064	-
6	R. Vertebral	14.8	0.123	10360	0.302
7	R. Subclavian II	42.2	0.510	1864	-
8	R. radial	23.5	0.106	11464	0.273
9	R. Ulnar I	6.7	0.145	8984	-
10	R. Interosseous	7.9	0.031	51576	0.319
11	R. Ulnar II	17.1	0.133	9784	0.298
12	R. internal Carotid	17.6	0.121	10576	0.261
13	R. external Carotid	17.7	0.121	9868	0.26
14	Aortic Arch II	3.9	3.142	520	-
15	L. Carotid	20.8	0.430	2076	-
16	L. internal Carotid	17.6	0.121	10576	0.261
17	L. external Carotid	17.7	0.121	9868	0.264
18	Thoracic Aorta I	5.2	3.142	496	-
19	L. Subclavian I	3.4	0.562	1664	-
20	Vertebral	14.8	0.123	10360	0.302
21	L. Subclavian II	42.2	0.510	1864	-
22	L. Radial	23.5	0.106	11464	0.274
23	L. Ulnar I	6.7	0.145	8984	-
24	L. Interosseous	7.9	0.031	51576	0.319
25	L. Ulnar II	17.1	0.133	9784	0.298
26	Intercostals	8.0	0.196	3540	0.209
27	Thoracic Aorta II	10.4	3.017	468	-
28	Abdominal I	5.3	1.911	668	-
29	Celiac I	2.0	0.478	1900	-
30	Celiac II	1.0	0.126	7220	-
31	Hepatic	6.6	0.152	4568	0.308
32	Gastric	7.1	0.102	6268	0.307
33	Splenic	6.3	0.238	3224	0.31
34	Superior Mesenteric	5.9	0.430	2276	0.311
35	Abdominal II	1.0	1.247	908	-
36	L. Renal	3.2	0.332	2264	0.287
37	Abdominal III	1.0	1.021	1112	-
38	R. Renal	3.2	0.159	4724	0.287
39	Abdominal IV	10.6	0.697	1524	-
40	Inferior Mesenteric	5.0	0.080	7580	0.306
41	Abdominal V	1.0	0.578	1596	-
42	R. common Iliac	5.9	0.328	2596	-
43	L. common Iliac	5.8	0.328	2596	-
44	L. external iliac	14.4	0.252	5972	-
45	L. internal Iliac	5.0	0.181	12536	0.308
46	L. Femoral	44.3	0.139	10236	-
47	L. deep Femoral	12.6	0.126	10608	0.295
48	L. posterior Tibial	32.1	0.110	23232	0.241
49	L. anterior Tibial	34.3	0.060	36972	0.239
50	R. external Iliac	14.5	0.252	5972	-
51	R. internal Iliac	5.1	0.181	12536	0.308
52	R. Femoral	44.4	0.139	10236	-
53	R. deep Femoral	12.7	0.126	10608	0.296
54	L. posterior Tibial	32.3	0.110	23232	0.241
55	R. anterior Tibial	34.4	0.060	36972	0.239

Table 6.1: Data used in the computational model of the 55 arteries. The data is from the physiological data published by Westerhof [105] and Stergiopulos [97] with the changes made by Wang and Parker [104].

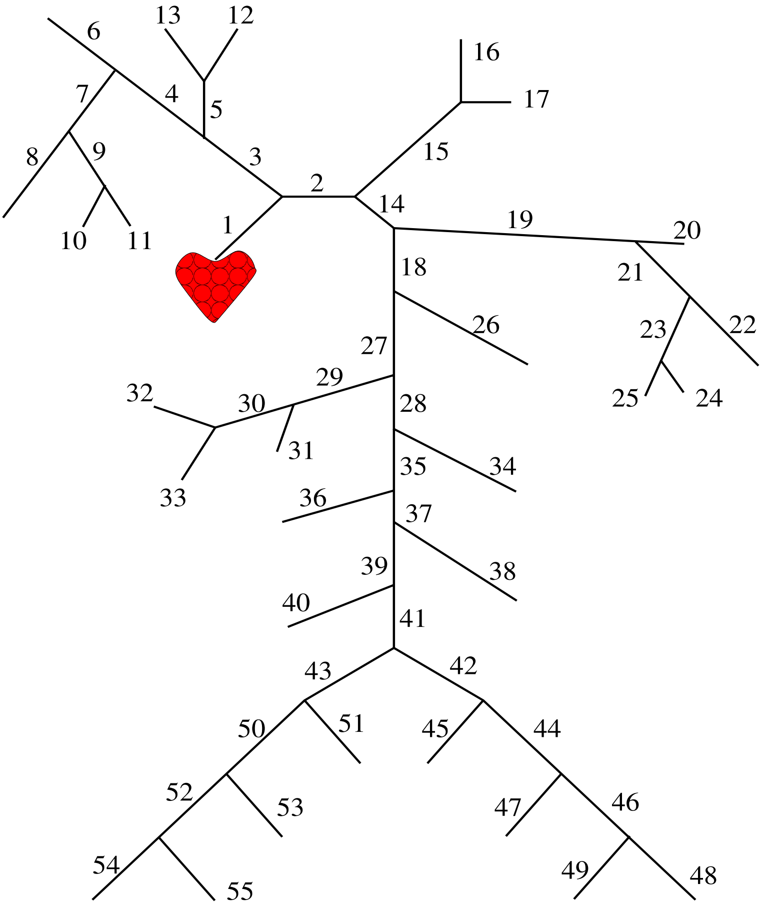

Figure 6.7: Arterial tree composed of a set of 55 straight vessels, described by 1D models. Physiological case (see Table 6.3).

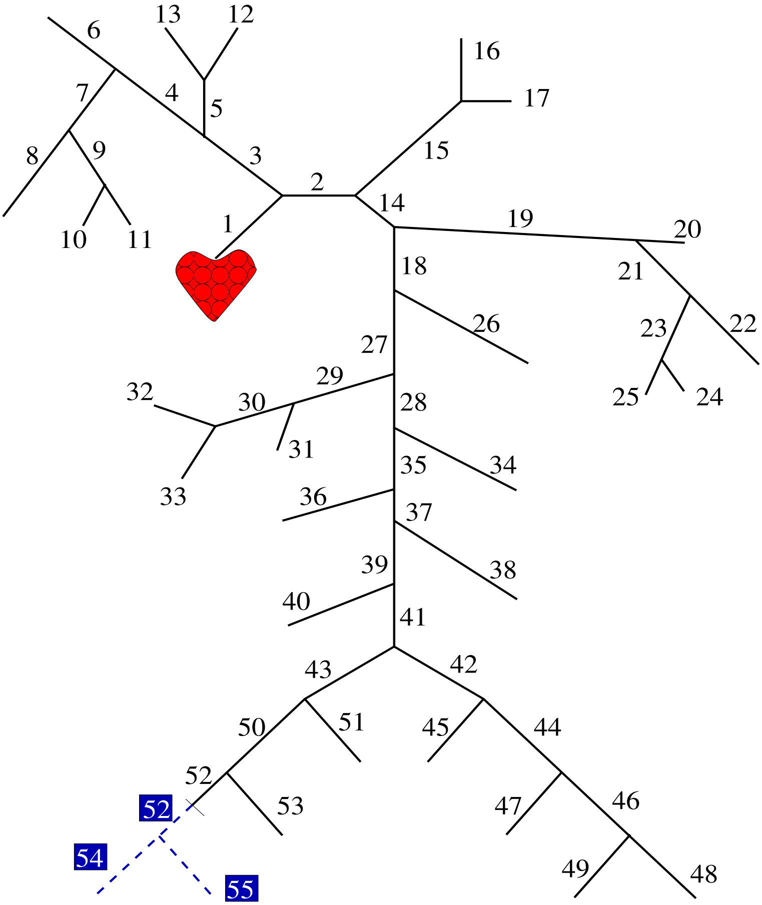

Figure 6.8: Arterial tree composed of a set of 55 straight vessels, described by 1D models. Pathological test case: vessels outlined in the boxes are cut away from the system.

respectively) computed for the same simulations. Both the case of 55 physiological and 53 pathological networks have been considered.
Figure 6.10 refers to the same simulation carried out in the case of an elderly patient.
The impact of the coupling of the heart in the numerical model is evident from Figure 6.9 and 6.10. In particular, it is worth to be mentioned the underestimation of the reflections in the pathological case when the heart coupling is not considered in the model. This was to be expected, since in the non-coupled case the action of the heart is actually independent of the real overload induced on the heart by increasing the peripheral resistances. This induces a sort of smoothing effect, that strongly dumps the wave reflections. In particular, looking at the Riemann invariants, in the non-coupled case the incoming variable W_1 is obviously independent of the outgoing waves, which is however unphysical. On the other hand, presence of wave reflections is felt by the heart in the coupled model.
Another remark refers to Figure 6.10, where an elderly patient is considered. The sensitivity of the uncoupled model to the Young's moduli of the arteries is significantly lower than in the coupled case, as can be noticed by comparing with the case of a middle aged individual. This was to be expected too, since the damping effect mentioned above reduces the impact of a change in the moduli over the system.
These results show the relevance of the heart coupling.

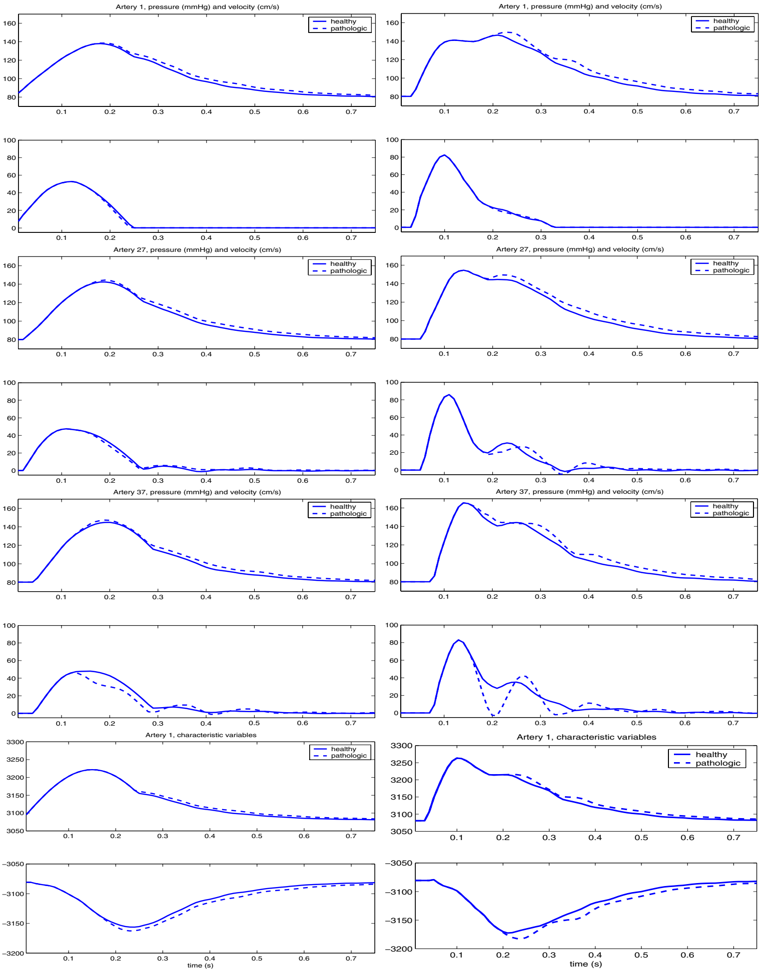

Figure 6.9: Comparison between the case with a simplified representation of the heart, based on boundary conditions, (left) and a lumped parameter representation of the heart, based on the varying elastance model of Figure 6.4, (right). Velocity and pressures at different arteries are presented in the first four pictures. The last pictures illustrate a comparison between the Riemann invariants W_1 (fifth row) and W_2 (sixth row). We are simulating adult circulation in a physiologic (solid) and pathologic (dotted) test case.

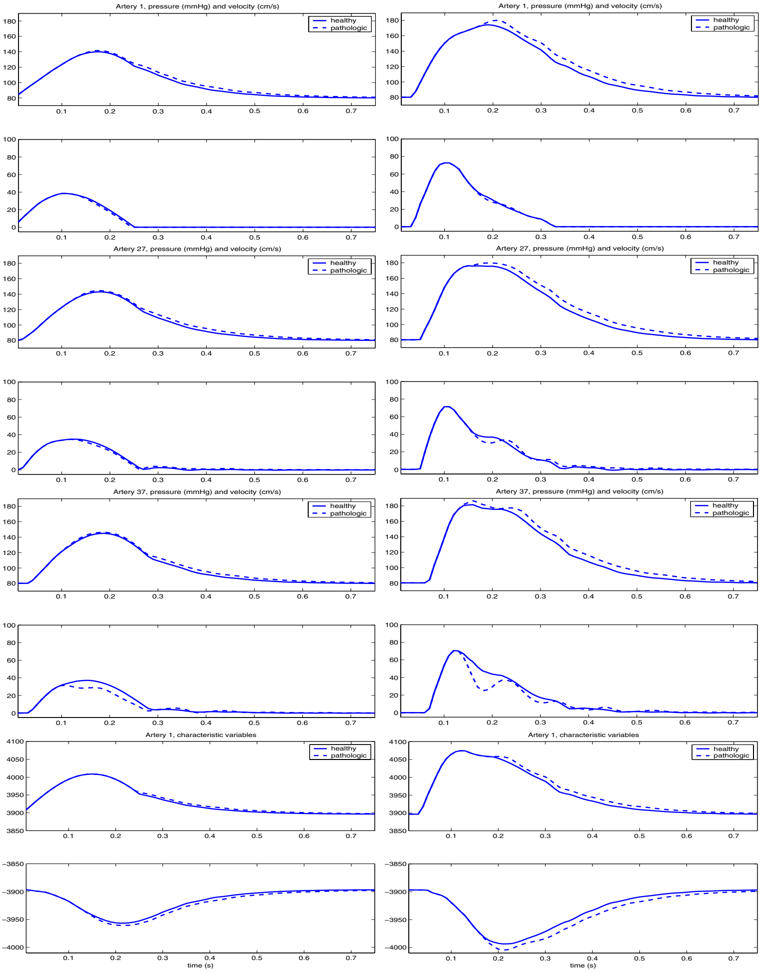

Figure 6.10: Same simulation of Figure 6.9 for an elderly patient.

Chapter 7

Numerical tests on cases of clinical interest

Introduction

Physiopathological evidence suggests that major differences in the shape of aortic flow and pressure waves among patients occur either in the presence or in the absence of cardiovascular diseases [56, 57]. In fact, the contour of pressure and flow waves in major systemic arteries can be explained on the basis of wave reflections and their interaction with the heart. The physical structure of the arterial system leads indeed to the reflection of waves at critical regions such as bifurcations, abrupt changes of the arterial stiffness or radius. These reflections are by far relevant in determining the working point of the coupled heart/arterial network system (see [59]).
The basic arterial network we consider in our simulations has already been illustrated in the previous Chapter (Figure 6.7 and Table 6.3 for data). Moreover, all the details about models and methods have been outlined therein.
In this Chapter this numerical model is used for the simulation of physiological situations for individuals of different age. In fact, arterial stiffness increases with age ([59],[12]) and this reflects in suitable modifications of the values of parameters of the numerical model. In particular, we investigate the overload on the heart induced by the backward waves, whose relevance is increased by the stiffening of the vessel walls.
In a similar way, some pathological situations can be considered where anomalous pressure wave reflections could have some consequences on the heart. Drastic modification in the arterial network such as the ones induced by an amputation (for instance as a consequence of diabetes), are described by a suitable modification of the computational domain. This case has already been presented in the previous Chapter (*pathological* test case, Figure 6.8). Abrupt changes in the stiffness of the wall of a particular district such as the ones induced by the presence of an endoprosthesis could be described at the mathematical level with a modification of the physical parameters of the 1D network (as seen in Section 4.1.2).
Preliminary numerical results referring to the *pathological* test case are presented here.

Part of the results reported in this Chapter are taken from [30].

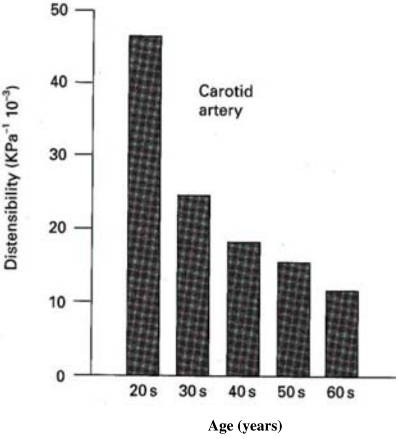

Figure 7.1: Relation between distensibility and age for a central elastic artery. Taken form [11].

7.1 Physiological test case and aging effects

We consider the basic arterial network illustrated in the previous Chapter (Figure 6.7). All the data for a middle aged patient are reported in Table 6.3. As already pointed out, *aging* consists in changing the stiffness of the arteries (see Figure 7.1). More precisely, Young's modulus has been reduced by 100 % in the case of a young patient and increased by 100 % for an elderly patient.

Figures 7.2, 7.4, 7.6, 7.5, 7.8 and 7.9 refer to simulations of the physiological case.

In particular, Figure 7.2 shows the time history of the left ventricle and the aortic pressures during a heart beat. When the valve is open the two curves clearly superimpose and the aortic pressure is due to the left ventricle - arterial system interaction. Otherwise the aortic pressure is determined by the wave reflections along the arterial network and at its end.

Figure 7.4 shows the behavior of the arterial pressure and flow waves in arteries at different locations of the system in the physiological case of a middle aged individual. We report results from the thoracic aorta up to the tibial artery. This Figure indicates that the numerical model is able to correctly simulate the behavior of arterial flow and pressure waves as they travel away from the heart (see for comparison Figure 7.3 taken from [59]). In fact, mean pressure falls slowly but the pulsatile pressure variation increases until in the tibial artery. It may double that at the root of the aorta. The flow oscillation, on the contrary, diminishes markedly from the proximal aorta to the tibial arteries. Such behavior can only be accounted for by the presence of a strong reflection in the small peripheral vessels, due to high peripheral

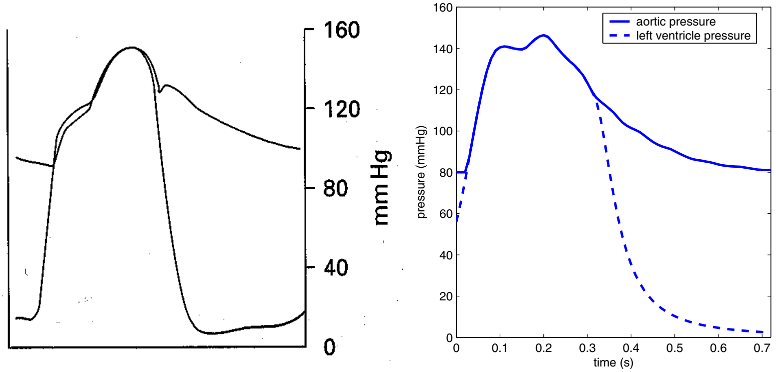

Figure 7.2: Left ventricle pressure and aortic pressure. The image on the left has been taken from [59]. The image on the right reproduces our results for a middle aged patient. The pressures in the aorta and in the left ventricle are superimposed when the heart valve is open (see Section 6.2.2).

resistances (i.e. high R_t). In fact, in the absence of reflections (low peripheral resistances), damping would cause a parallel fall in pressure and flow oscillations. The probable region of this fall appears to be the smallest arteries and proximal arterioles. This fall also occurs in the splanchnic branches of the abdominal aorta (renal, superior and inferior mesenteric) but there is no back flow and flow contour is similar to that of pressure. This can be attributed to low peripheral resistance and to a low reflection coefficient in vascular beds supplied by these arteries (see [51], [57]).

In Figure 7.6 we compare the behavior of the arterial pressure and flow waves in arteries of subjects of different ages, while in Figure 7.5 we report the pressure-volume curves for the heart at different ages. In Figure 7.6 it is evident that the system is able to simulate the major changes of the arterial pulse as seen with hypertension or aging. Usually these alterations are attributable to arterial stiffening and to a more rapid travel of the pulse along the major arteries and to consequent early return of wave reflection from the periphery of the body. Comparing flow and pressure waves, one notes that in the young adult the wave speed is low and reflections arrive late, i.e. they arrive in diastole back in the aorta. In the older human, wave speed has increased and the reflections return in systole. This is the reason for disappearance of the reflected wave from diastole and its movement into systole, with characteristic boost to pressure in late systole in elderly patients. Decreased distensibility also increases pressure wave amplitude. Increased wave velocity causes wave reflection to return earlier and often leads to fusion of incident and reflected waves with generation of a pressure wave with a later systolic peak in all major arteries. It is worth to be noticed that the increasing of the arterial stiffness induces a heart overload. This can be seen in the $P - V$ diagrams of Figure 7.5. The increment of the area spanned by the $P - V$ curve in the elderly case is evident and corresponds to the ventricular overload induced by the stiffening.

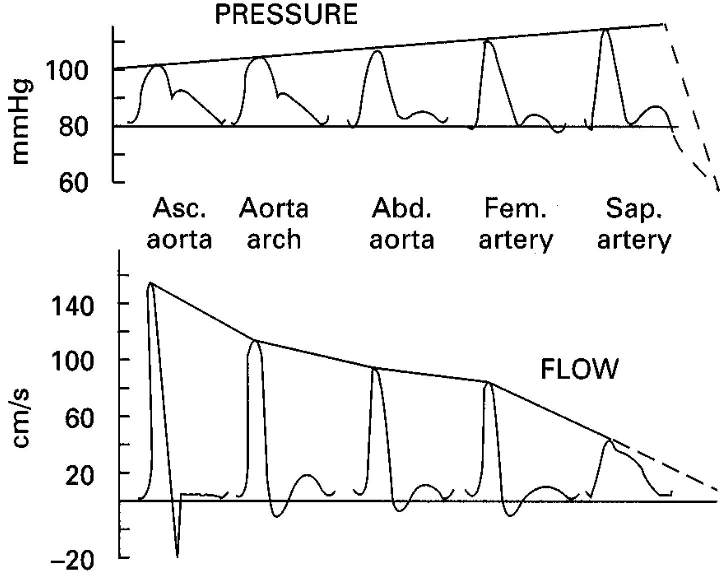

Figure 7.3: Diagrammatic comparison of the behavior of the arterial pressure and flow pulses in arteries as they travel away from heart (taken from [59]). Mean pressure falls slowly, but the pulsatile pressure variation increases; on the other side the flow oscillation diminishes markedly.

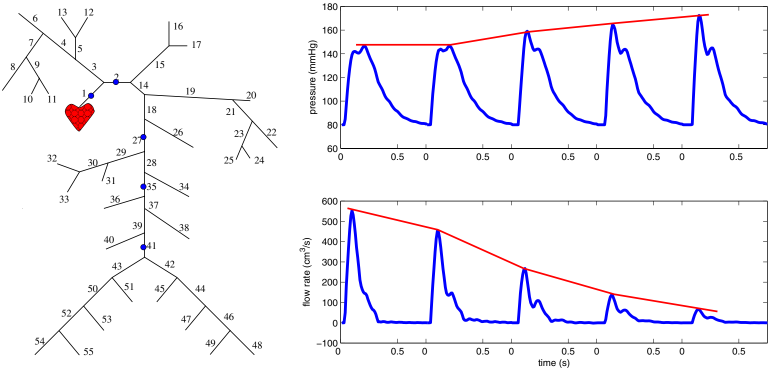

Figure 7.4: Diagrammatic comparison of the behavior of the arterial pressure and flow pulses in arteries as they travel away from heart. The Figure on the right shows flow and pressure waves (as obtained from our model in the case of an adult patient) at the selected points represented on the left.

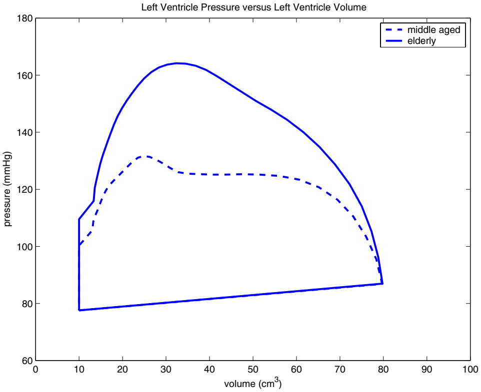

Figure 7.5: Pressure-volume curves for the left ventricle at different ages.

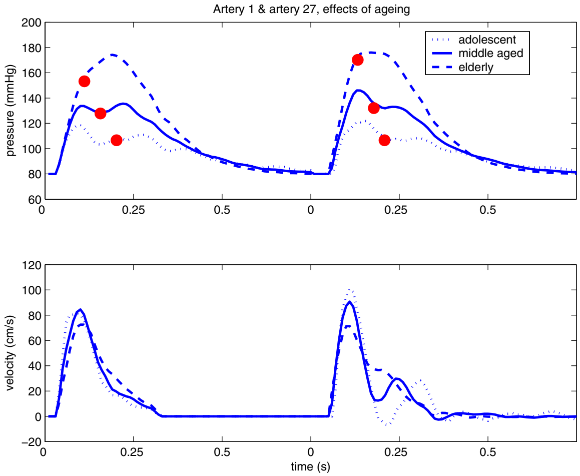

Figure 7.6: Pressure and flow waves in the ascending and thoracic aorta for different ages individuals. Physiological case (55 arteries network).

The Figure 7.8 shows the behavior of the pressure wave forms as a function of location from the ascending aorta to the iliac bifurcation compared with the flow wave pattern in each chosen artery.

Figure 7.9 shows the behavior of subclavian artery pressure wave compared to that of aortic arch for a middle aged individual.

The appearance of reflected waves is outlined also in Figure 7.8 where this occurs progressively earlier in systole as the wave approaches the iliac bifurcation. The amplitude of the reflection increases peripherally. As previously pointed out, the morphology of the network induces the presence of reflections. Possible reflecting sites include branching points, a change of arterial calibre (tapering), or of the elastic properties of the arterial wall [51]. At a given location in the ascending aorta the forward pulse wave interacts with the backward travelling (reflected) wave while systole is still in progress. This reflected wave “adds up” to the forward wave and yields the archetypal ascending aorta pressure wave-form [57]. The interaction with the reflected wave, as indicated by comparing flow and pressure waves, occurs progressively earlier in systole as we approach the iliac bifurcation. As the initial portion of the reflected wave occurs progressively early during the systole with increasing distance from the aortic valve, the diastolic portion of the reflected wave moves from diastole into systole too. In addition to the earlier appearance of the reflected wave, the amplitude of the reflection increases peripherally. These observations further support the evidence that the terminal abdominal aorta behaves as the major reflection site in man [57]. Perhaps this is evident in Figure 7.8.

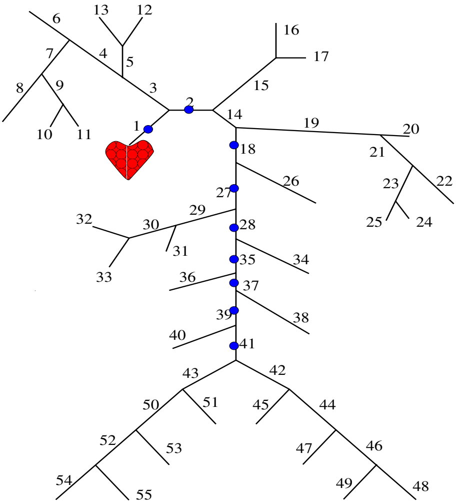

Figure 7.7: 55 arteries network and selected locations from ascending aorta to iliac bifurcation.

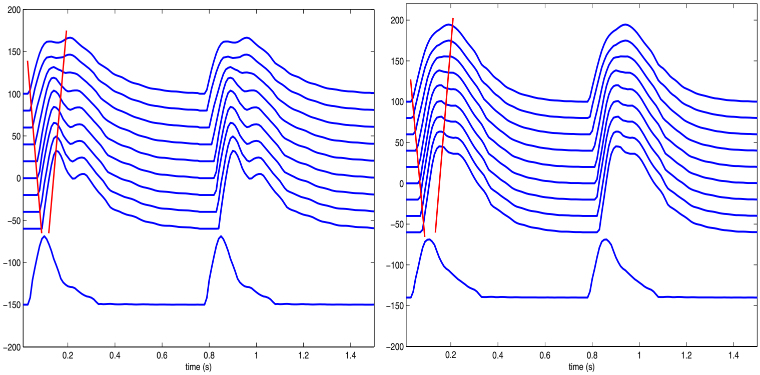

Figure 7.8: Pressure waves at the different locations of Figure 7.7 for a middle aged (left) and an elderly patient (right). On the bottom we report the flow rate in the ascending aorta.

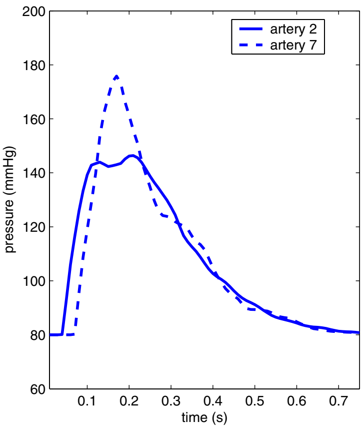

Figure 7.9: Results of the physiological test case in the aortic arch and in the subclavian artery.

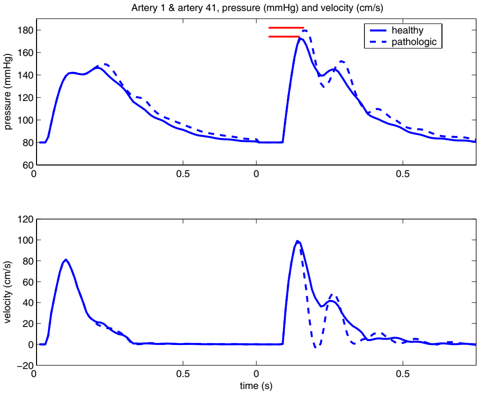

Figure 7.10: Ascending (top) and abdominal (bottom) pressure waves for the physiological and the pathological case.

Arterial terminations in the upper part of the body are another relevant reflecting site. As a matter of fact, in man peak and nadir of the brachial artery pressure waves are considered to represent systolic and diastolic pressure throughout the whole arterial system. Moreover, the contour of pressure pulse in the upper limb is quite different from that in the femoral artery and its peripheral branches. For instance, there are usually two systolic peaks in the brachial artery but only one in the femoral artery. This suggest a sort of amplification in the upper limb arteries due to the shortest time period between the initial systolic peak and diastolic wave. In normal circumstances the arterial pressure wave is markedly amplified in transit from the ascending aorta to the radial artery [21]. Moreover, when arterial pressure is taken on the upper arm by using a sphygmomanometer, we actually measure the pressure in the brachial artery, which is different from the pressure in the aorta (or other distributing arteries) [65]. Our system is able to simulate this amplification phenomenon in the brachial artery due to the shortest time period between the initial systolic peak and the diastolic wave (Figure 7.9). In normal situations this difference may be relatively small in absolute terms and may warrant the assumption that central aortic and brachial systolic pressures are identical.

7.2 A pathological test case

In order to outline the increase of wave reflections, we considered also a case of a complete obstruction of the right femoral artery. This means that in this case the 55 arteries network reduces to a set of 53 vessels, as indicated in Figure 6.8 (*pathological case*), and the distal conditions on the right femoral artery corresponds to a null distal velocity (complete blockage, $R_t = 1$).

Figure 7.10 compares the results of the physiological and the pathological cases. More precisely, we report the different behavior of the abdominal aorta pressure waves.

It can be noticed that flow and pressure wave contours are markedly altered close to the arterial obstruction, while only little perceptible changes in flow and pressure wave contours of the proximal aorta can be remarked. This can be explained by dissipation phenomena from abdominal to thoracic aorta. When the obstruction is at a distance, the net effect to the flow is similar to that seen during peripheral vasoconstriction, with a fall in the entire flow with the onset of a back flow. Arterial obstruction is associated to a decrease in amplification of the pressure wave as a result of a local higher reflection phenomenon. Local aortic systolic pressure in presence of iliac-femoral artery obstruction may exceed the normal aortic pressure by far 30-40 $mmHg$.

Conclusions

The aim of this work was to provide a tool for the numerical simulation of the human cardiovascular system. The studies conducted at *EPFL*, in the *Chaire de Modélisation et Calcul Scientifique*, show that this problem is global, in the sense that local changes can modify the solution far away. From the point of view of computing and modeling this suggests the use of multiscale methods. By far this seems the best way to perform a global calculation reaching a "good" level of local details. Since 1D models play a major role in the description of blood wave propagation, in the first part of this work we improved them by accounting for a more complex vessel wall law and more general geometries, such as bifurcated channels, curved vessels, stented arteries). However, our study of curved geometries is at a preliminary state and needs to be furtherly developed.
In the second part of the thesis we presented a multiscale model for the simulation of the whole arterial network at low computational cost. Specific attention has been devoted to the coupling between the left ventricle and the arterial system, whose physiopathological relevance is well known.

The mathematical model gives satisfactory results in numerical tests and is able to describe the most relevant features of the pressure wave propagation and reflections within the arterial system. Moreover, a 3D model could be inserted in our system without major difficulties (for example it could be used to represent an aneurysm before and after surgical treatment). This would allow undoubtely to better describe the local stresses and flow patterns.

Future developments could be devoted to an extensive application of the model to simulate realistic pathological cases. In order to achieve this task the parameters of the lumped models should be better fit. In particular, the solution strongly depends on the parameter setting of the elastance model used to describe the left ventricle; moreover, the resistive parameter, present therein, should not be neglected.

From the modeling viewpoint, the next steps to improve the model here presented could be the inclusion of the venous system (possibly represented through a lumped parameter model), and a more precise description of the heart, hence allowing the closure of the system.

Bibliography

[1] Analysis of coronary stents. EndoLab GmbH.

[2] Stent simulation applications. IDAC, Integrated Design & Analysis Consultants (Ireland) Ltd.

[3] *International Cardiovascular Disease Statistics.* American Heart Association, 2003.

[4] *Atlas of the body.* American Medical Association, 2004. http://www.ama-assn.org/ama/pub/category/7140.html.

[5] *Heart Disease and Stroke Statistics – 2004 Update.* American Heart Association, 2004.

[6] H. Gray (1825-1861). *Anatomy of the Human Body.* 1918.

[7] J. Abram. *Tensor calculus through differential geometry.* Butterworths, 1965.

[8] R. Alexander, V. Fuster, S. King, R. O'Rourke, R. Roberts, and H. Wellens. *Hurst's The Heart.* McGraw-Hill Professional, 10th edition edition, 2000.

[9] D. Ambrosi and L. Quartapelle. A Taylor-Galerkin method for simulating nonlinear dispersive water waves. *J. Comput. Phys.*, 146(2):546–569, 1998.

[10] R. Aris. *Vectors, Tensors and the Basic Equations of Fluid Mechanics.* Prentice Hall, 1962.

[11] A. Benetos, S. Laurent, A.P. Hoeks P.H. Boutouyrie, and M.E. Safar. Arterial alterations with ageing and high blood pressure: A noninvasive study of carotid and femoral arteries . *Arteriosclerosis and Thrombosis*, 13:90–97, 1993.

[12] L.M. Van Bortel and J.J. Spek. Influence of aging on arterial compliance. *Journal of human hypertension*, 12:583–586, 1998.

[13] K. Boukir, Y. Maday, and B. Métivet. A high order characteristics method for the incompressible Navier-Stokes equations. *Comput. Methods Appl. Mech. Engrg.*, 116(1-4):211–218, 1994. ICOSAHOM'92 (Montpellier, 1992).

[14] S. Čanić. Blood flow through compliant vessels after endovascular repair: wall deformations induced by the discontinuous wall properties. *Computing and Visualisation in Science*, 4:147–155, 2002.

[15] S. Čanić and E.H. Kim. Mathematical analysis of the quasilinear effects in a hyperbolic model of blood flow through compliant axi-symmetric vessels. *Mathematical Methods in Applied Sciences*, 26:1161–1186, 2003.

[16] S. Čanić, D. Lamponi, and A. Mikelić. Self-consistent effective equations modeling blood flow in medium-to-large compliant arteries. Submitted to SIAM J. Multiscale Analysis and Simulation, 2003.

[17] S. Čanić and D. Mirković. A hyperbolic system of conservation laws in modeling endovascular treatment of abdominal aortic aneurysm. *Hyperbolic Problems: Theory, Numerics, Applications*, 141:227–236, 2000.

[18] M. Do Carmo. *Differential geometry of curves and surfaces.* Prentice Hall, 1976.

[19] R. Carola, J.P. Harley, and C.R. Noback. *Human anatomy & physiology.* McGraw-Hill, 1990.

[20] D.P. Chock. A comparison of numerical methods for solving the advection equation. *Atmos. Environ.*, pages 853–871, 1991.

[21] G.R. Cokelet. The rheology and tube flow of blood. In R. Skalak and S. Chen, editors, *Handbook of Bioengineering.* McGraw-Hill, 1987.

[22] S. Deparis. *Numerical analysis of axisymmetric flows and methods for fluid-structure interaction arising in blood flow simulation.* PhD thesis, École Polytechnique Fédérale de Lausanne (EPFL), 2004. Thesis N. 2965.

[23] J. Donea, S. Giuliani, H. Laval, and L. Quartapelle. Time-accurate solutions of advection-diffusion problems by finite elements. *Comp. Meth. Appl. Mech. Engng.*, 45:123–145, 1984.

[24] J. Donea, L. Quartapelle, and V. Selmin. An analysis of time discretization in the finite element solution of hyperbolic problems. *J. Comput. Phys.*, 146(2):463–499, 1987.

[25] F. Dubois and P. Le Floch. Boundary conditions for nonlinear hyperbolic systems of conservation laws. *Journal of Differential Equations*, 71:93–122, 1988.

[26] L. Euler. *Principia pro motu sanguinis per arterias determinando*, volume 2, chapter Opera posthuma mathematica et physica anno 1844 detecta, pages 814–823. ediderunt Ph Fuss et N Fuss Petropoli, Appund Eggers et Socios, 1844.

[27] C. Fauchier-Magnan. Une étude de l'écoulement d'un fluide dans un tube courbé. Project de diplôme. Département de mathématiques, EPFL, hiver 2000-2001.

[28] L. Formaggia, J.-F. Gerbeau, F. Nobile, and A. Quarteroni. On the coupling of 3D and 1D Navier-Stokes equations for flow problems in compliant vessels. *Comp. Methods in Appl. Mech. Engng.*, 191:561–582, 2001.

[29] L. Formaggia, D. Lamponi, and A. Quarteroni. One dimensional models for blood flow in arteries. *J. Eng. Math.*, 47:251–276, 2003.

[30] L. Formaggia, D. Lamponi, M. Tuveri, and A. Veneziani. Numerical modeling of 1D arterial networks coupled with a lumped parameters description of the heart. 2004. Submitted.

[31] L. Formaggia, F. Nobile, J.-F. Gerbeau, and A. Quarteroni. Numerical treatment of defective boundary conditions for the Navier-Stokes equations. *SIAM J. Numer. Anal.*, 40:376–401, 2002.

[32] L. Formaggia, F. Nobile, and A. Quarteroni. A one dimensional model for blood flow: application to vascular prosthesis. In I. Babuška, T. Miyoshi, and P.G. Ciarlet, editors, *Mathematical Modeling and Numerical Simulation in Continuum Mechanics*, volume 19 of *Lecture Notes in Computational Science and Engineering*, pages 137–153, Berlin, 2002. Springer-Verlag.

[33] L. Formaggia, F. Nobile, A. Quarteroni, and A. Veneziani. Multiscale modelling of the circulatory system: a preliminary analysis. *Computing and Visualisation in Science*, 2:75–83, 1999.

[34] L. Formaggia and A. Veneziani. *Reduced and Multiscale Models for the Human Cardiovascular System.* Von Karman Institute, 2003. Lecture Notes of the 7^{th} VKI Lecture Series, "Biological Fluid Dynamics".

[35] Y.C. Fung. *Biomechanics: Mechanical Properties of Living Tissues.* Springer-Verlag, New York, 1993.

[36] E. Godlewski and P.-A. Raviart. *Numerical Approximation of Hyperbolic Systems of Conservation Laws*, volume 118 of *Applied Mathematical Sciences.* Springer, New York, 1996.

[37] C.L. Goh. One dimensional models for blood flow circulation. Diploma Report. Imperial College of Science, 2001.

[38] A.E. Green and P.M. Naghdi. A direct theory of viscous fluid flow in pipes i. basic general developments. *Philosophical Transactions of the Royal Society of London*, 1993.

[39] A.E. Green, P.M. Naghdi, and M.J. Stallard. A direct theory of viscous fluid flow in pipes ii. flow of incompressible viscous fluid in curved pipes. *Philosophical Transactions of the Royal Society of London*, 1993.

[40] B. Haridas and C. Haynes. Predictive analysis at the forefront of medical product development. *Medical Device & Diagnostic Industry*, pages 112–119, Oct 1999.

[41] H. Holden and N.H. Risebro. Riemann problems with a kink. *SIAM J. Math. Anal.*, 30,3:497–515, 1999.

[42] G.A. Holzapfel. Biomechanics of soft tissue. *Biomech preprint series*, 2000.

[43] G.A. Holzapfel, T.C. Gasser, and R.W. Ogden. A new constitutive framework for arterial wall mechanics and a comparative study of material models. *Journal of Elasticity*, 61:1–48, 2000.

[44] G.A. Holzapfel, T.C. Gasser, and M. Stadler. A structural model for the viscoelastic behavior of arterial walls: Continuum formulation and finite element simulation. *Biomech preprint series*, 2001.

[45] F. Hoppensteadt and C. Peskin. *Mathematics in Life Sciences and Medicine.* Springer-Verlag, New York, 1992.

[46] J. Keener and J. Sneyd. *Mathematical Physiology.* Interdisciplinary Applied Mathematics - Springer NY, 1998.

[47] B.V. Rathish Kumar, A. Quarteroni, L. Formaggia, and D. Lamponi. On parallel computation of blood flow in human arterial network based on 1D modelling. *Computing*, 71:321–351, 2003.

[48] K. Laganà, G. Dubini, F. Migliavacca, R. Pietrabissa, G. Pennati, A. Veneziani, and A. Quarteroni. Multiscale modelling as a tool to prescribe realistic boundary conditions for the study of surgical procedures. *Biorheology*, 39(3-4):359–364, 2002.

[49] L.D. Landau and E.M. Lifschitz. *Elasticity theory.* Pergamon Press, Oxford, 1975.

[50] G.J. Langewouters, K.H. Wesseling, and W.J.A. Goedhard. The static elastic properties of 45 human thoracic and 20 abdominal aortas in vitro and the parameters of a new model. *J. of Biomech.*, 17:425–435, 1984.

[51] R.D. Latham, N. Westerhof, P. Sipkema, B. Rubal, and P. Reuderink. Regional wave travel and reflections along the human aorta: a study with six simultaneous micromanometric pressures. *Circulation*, 72:1257–1269, 1985.

[52] R.J. LeVeque. *Numerical Methods for Conservation Laws.* Birkhauser, Basel, 1990.

[53] P. Luchini, M.Lupo, and A. Pozzi. Unsteady stokes flow in a distensible pipe. *ZAMM - Z. angew. Math. Mech.*, 71:367–378, 1991.

[54] F. Migliavacca, L. Petrini, M. Colombo, F. Auricchio, and R. Pietrabissa. Mechanical behavior of coronary stents investigated through the finite element method. *J. of Biomech.*, 35:803–811, 2002.

[55] R. Mongrain, E. Aboumansour, S. Plante, O.F. Bertrand, and J.C. Tardif. Development of a 3d cad model for the structural analysis of a coronary stent. In D. Mantovani, editor, *Advanced Materials for Biomedical Applications*, pages 257–268. Canadian Institute of Mining, Metallurgy and Petroleum, 2000.

[56] J.P. Murgo, S.A. Altobelli, J.F. Dorethy, J.R. Logsdon, and G.M. McGranathan. Normal ventricular ejections dynamics in man during rest and exercis. In D.F. Leon and J.A. Shaver, editors, *Physiologic Principles of Heart Sounds and Murmurs*, pages 92–. American Heart Association, Dallas, 1975.

[57] J.P. Murgo, N. Westerhof, J.P. Giolma, and S.A. Altobelli. Aortic impedance in normal man: relationship to pressure waveforms. *Circulation*, 62:105–116, 1980.

[58] P.M. Naghdi. Finite deformation of elastic rods and shells. In *Proceedings of the IUTAM Symposium on finite elasticity, Lehigh University*, 1980.

[59] W.W. Nichols and M.F. O'Rourke. *McDonald's Blood Flow in Arteries.* Edward Arnold, London, fourth edition, 1998.

[60] F. Nobile. *Numerical approximation of fluid-structure interaction problems with application to hemodynamics.* PhD thesis, École Polytechnique Fédérale de Lausanne (EPFL), 2001. Thesis N. 2458.

[61] A. Noordergraaf, H.B.K. Boom, and P.D. Verdouw. A human systemic analog computer. In A. Noordergraaf, editor, *1st Congr. Soc. for Ballistocardiographic Res.*, 1960.

[62] M. Olufsen. A one-dimensional fluid dynamic model of the systemic arteries. In J. Ottesen and M. Danielsen, editors, *Proceedings from Mathematical Modelling in Medicine, September 1997, Roskilde University.* Roskilde University Press, 1997.

[63] M. Olufsen. *Modeling the arterial system with reference to an anestesia simulator.* PhD thesis, Rotskilde Univ., 1998. Tekst 345.

[64] M. Olufsen and J. Ottesen. A fluid dynamical model of the aorta with bifurcations. Tekst 297, Rotskilde Univ., 1995.

[65] M.F. O'Rourke, A.P. Avolio, and W.W. Nichols. Left ventricular systemic arterial coupling in humans and strategies to improve coupling in disease states. In F.C.P. Yin, editor, *Vascular/Ventricular coupling*, pages 1–19. Spring Publishing Co, Inc., New York, 1987.

[66] T.J. Pedley. *The Fluid Mechanics of Large Blood Vessels.* Cambridge University Press, Cambridge, G.B., 1980.

[67] J. Peiró, S.J. Sherwin, K.H. Parker, V. Franke, L. Formaggia, D. Lamponi, and A. Quarteroni. Numerical simulation of the arterial pulse propagation using one-dimensional models. In M. Atherton et al., editor, *Wall-Fluid Interactions in Physiological Flows.* 2004.

[68] C.S. Peskin. *Partial Differential Equations in Biology.* Courant Institute of Mathematical Sciences, New York University, USA, 1976.

[69] F. Phythoud, N. Stergiopulos, and J.-J. Meister. Forward and backward waves in the arterial system: nonlinear separation using riemann invariants. *Technology and Health Care*, 3:201–207, 1995.

[70] F. Phythoud, N. Stergiopulos, and J.-J. Meister. Separation of arterial pressure waves into their forward and backward running components. *J. Biomech. Eng.*, 118:295–301, 1996.

[71] R. Pietrabissa, A. Quarteroni, G. Dubini, A. Veneziani, F. Migliavacca, and S. Ragni. From the global cardiovascular hemodynamics down to the local blood motion: preliminary applications of a multiscale approach. In E. Onate et al., editor, *ECCOMAS 2000*, Barcelona, 2000.

[72] G. Pontrelli. A mathematical model of flow through a liquid-filled viscoelastic tube. *Med. Biol. Eng. Comput.*, 40:550–556, 2002.

[73] G. Pontrelli and E. Rossoni. Numerical modelling of the pressure wave propagation in the arterial flow. *Int. J. Num. Meth. Fluids*, 43:651–671, 2003.

[74] L. Quartapelle. *Numerical solution of the incompressible Navier-Stokes equations.* Birkhäuser Verlag, Basel, 1993.

[75] A. Quarteroni. Mathematical modelling of the cardiovascular system. In L. Tatsien, editor, *Proceedings of the International Congress of Mathematicians*, volume III, Beijing, 2002. Higher Education Press.

[76] A. Quarteroni. *Modellistica numerica per problemi differenziali.* Springer-Verlag, Berlin, 2003.

[77] A. Quarteroni and L. Formaggia. *Modelling of Living Systems*, chapter in Mathematical Modelling and Numerical Simulation of the Cardiovascular System. Handbook of Numerical Analysis. Elsevier Science, Amsterdam, 2002. to appear.

[78] A. Quarteroni, S. Ragni, and A. Veneziani. Coupling between lumped and distributed models for blood problems. *Computing and Visualisation in Science*, 4:111–124, 2001.

[79] A. Quarteroni, M. Tuveri, and A. Veneziani. Computational vascular fluid dynamics: Problems, models and methods. *Computing and Visualisation in Science*, 2:163–197, 2000.

[80] A. Quarteroni and A. Valli. *Numerical Approximation of Partial Differential Equations.* Springer-Verlag, Berlin, 1994.

[81] A. Quarteroni and A. Valli. *Domain Decomposition Methods for Partial Differential Equations.* The Clarendon Press Oxford University Press, New York, 1999. Oxford Science Publications.

[82] A. Quarteroni and A. Veneziani. Analysis of a geometrical multiscale model based on the coupling of ODE's and PDE's for blood flow simulations. *SIAM J. Num. Anal.*, 2002 (submitted). Also MOX Report N.4/2002, MOX, Mathematics Department, Politecnico di Milano, Milan, Italy.

[83] S. Ragni. *Multiscale modelling of the circulatory system.* PhD thesis, Politecnico di Milano (Italy), 2000.

[84] V. Rideout and D. Dick. Difference-differential equations for fluid flow in distensible tubes. *IEEE Trans. Biomed. Eng.*, BME-14(3):171–177, 1967.

[85] A.M. Robertson and A. Sequeira. A director theory approach for modeling blood flow in the arterial system. *Annals of Biomedical Engineering*, 2003. submitted.

[86] T.A. Salerno, P. Hermandez, and R.B. Lynn. Abdominal aortic aneurysm in the elderly. *Can. J. Surg.*, 24:71–72, 1981.

[87] P. Segers, P. Morimont, P. Kohl, N. Stergiopulos, N. Westerhof, and P. Verdonck. Arterial elastance and heart-arterial coupling in aortic regurgitation are determined by aortic leak severity. *Am. Heart J.*, 568-576, 2002.

[88] P. Segers, N. Stergiopulos, N. Westerhof, P. Wouters, P. Kolh, and P. Verdonck. Systemic and pulmonary hemodynamics assessed with a lumped-parameter heart-arterial interaction model. *J. Eng. Math.*, 47:185–199, 2003.

[89] S.J. Sherwin. Dispersion analysis of the continuous and discontinuous Galerkin formulations. In B. Cockburn, G.E. Karniadakis, and C.W. Shu, editors, *Discontinuous Galerkin methods: Theory, computational and applications*, pages 425–431. Spring Publishing Co, Inc., 2000.

[90] S.J. Sherwin, L. Formaggia, and J. Peiró. Computational modelling of 1D blood flow with variable mechanical properties. In *Proceedings of ECCOMAS CFD 2001*, ECCOMAS, September 2001. CD-ROM Edition.

[91] S.J. Sherwin, L. Formaggia, J. Peiró, and V. Franke. Computational modelling of 1D blood flow with variable mechanical properties and its application to the simulation of wave propagation in the human arterial system. *Int. J. Num. Meth. Fluids*, 43:673–700, 2003.

[92] S.J. Sherwin, V. Franke, J. Peiró, and K.H. Parker. One-dimensional modelling of a vascular network in space-time variables. *J. Eng. Math*, 47:217–250, 2003.

[93] F.T. Smith, N.C. Ovenden, P.T. Franke, and D.J. Doorly. What happens to pressure when a flow enters a side branch? *Journal of Fluid Mechanics*, 479:231–258, 2003.

[94] F.T. Smith, R. Purvis, S.C.R. Dennis, M.A. Jones, N.C. Ovenden, and M. Tadjfar. Fluid flow through various branching tubes. *J. Eng. Math.*, 47:277–298, 2003.

[95] N. P. Smith, A. J. Pullan, and P. J. Hunter. An anatomically based model of transient coronary blood flow in the heart. *SIAM J. Appl. Math.*, 62(3):990–1018, 2002.

[96] N. Stergiopulos, Y. Tardy, and J.-J. Meister. Nonlinear separation of forward and backward running waves in elastic conduits. *J. of Biomech.*, 26:201–209, 1993.

[97] N. Stergiopulos, D. Young, and T. Rogge. Computer simulation of arterial flow with application to arterial and aortic stenoses. *J. of Biomech.*, 25:1477–1488, 1992.

[98] J.C. Stettler, P. Niederer, and M. Anliker. Theoretical analysis of arterial hemodynamics including the influence of bifurcations, part I: Mathematical model and prediction of normal pulse patterns. *Annals of Biomedical Engineering*, 9:145–164, 1981.

[99] V.L. Streeter, W.F. Keitzer, and D.F. Bohr. Pulsatile pressure and flow through distensible vessels. *Circulation Research*, 13:3, 1963.

[100] H. Suga. Global cardiac function: mechano-energetico-informatics. *J. of Biomech.*, 36:713–720, 2003.

[101] H. Suga and K. Sagawa. Instantaneous pressure-volume relationships and their ratio in the excised supported canine left ventricle. *Circ. Res.*, 35:117–126, 1974.

[102] H. Suga, K. Sagawa, and A.A. Shoukas. Load independence of the instantaneous pressure-volume ratio of the canine left ventricle and effects of epinephrine and heart rate on the ratio. *Circ. Res.*, 32:314–322, 1973.

[103] A. Veneziani. *Mathematical and Numerical Modelling of Blood Flow Problems.* PhD thesis, Politecnico di Milano (Italy), 1998.

[104] J. Wang and K.H. Parker. Wave propagation in a model of the arterial circulation. *J. of Biomech.*, 2004. to appear.

[105] N. Westerhof, F. Bosman, C. Vries, and A. Noordergraaf. Analog studies of the human systemic arterial tree. *J. of Biomech.*, 2:121–143, 1969.

[106] N. Westerhof and N. Stergiopulos. Models of the arterial tree. *Stud. Health Technol. Inform.*, 71:65–77, 2000.

Daniele Lamponi est né à Porto S. Giorgio, Italie, le 20 avril 1975. Il a effectué son école secondaire au Liceo Ginnasio F. Stabili à Ascoli Piceno où il a obtenu en 1994 sa Maturitá Classica. Ensuite, il a poursuivi ses études à l'Universitá di Bologna pour obtenir en 2000 un diplôme de physicien avec mention. Depuis mars 2001 il a été engagé comme assistant dans la chaire de modélisation et calcul scientifique du Professeur Alfio Quarteroni.
Il est co-auteur des publications suivantes :

- D. Lamponi, I. Zmijarević, R. Sanchez, *Diffusion synthetic acceleration of SN linear nodal schemes in weighted difference form*, Transactions of the American Nuclear Society, 80,246-248 (2000)
- D.R. Flower, I.A. Doytchinova, K. Paine, P. Taylor, M. J. Blythe, D. Lamponi, C. Zygouri, P.P. Guan, H. McSparron, H. Kirkbride *Computational vaccine design*, in D.R. Flower editor, Drug Design, pages 136-180, The Royal Society of Chemistry, Cambridge, 2002 (Special publication No. 279)
- L. Formaggia, D. Lamponi, A. Quarteroni, *One-dimensional Models for blood flow in arteries*, Journal of Engineering Mathematics, 47, 251-276, 2003.
- B.V.R. Kumar, A. Quarteroni, L. Formaggia, D. Lamponi. *On Parallel Computation of Blood Flow in Human Arterial Network Based on 1-D Modelling*, Computing, 71, 321-351, 2003.
- J. Peiró, S.J. Sherwin, K.H. Parker, V. Franke, L. Formaggia, D. Lamponi, A. Quarteroni, *Numerical Simulation of the Arterial Pulse Propagation Using One-Dimensional Models*, in Wall-Fluid Interactions in Physiological Flows, M.Atherton et Al. Eds. ,2003
- S. Čanić, D. Lamponi, A. Mikelić, *Self-consistent effective equations modeling blood flow in medium-to large compliant arteries*, submitted to SIAM Journal on Multiscale Problems and Simulations (2004).
- L. Formaggia, D. Lamponi, M. Tuveri, A. Veneziani, *Numerical modeling of a 1D arterial network coupled with a lumped parameter description of the heart*, preprint (2004).
- L. Formaggia, D. Lamponi, *One dimensional models for flow in curved vessels: application to haemodynamics. Preliminary results*, in preparation.